CO_2 capture using liquid crystals

Selectivity analysis for CO_2 capture from syngas

Confidential

Mechanical Engineering - Engineering Thermodynamics

B.C. Ramaker - June 2013

M.Sc. Thesis   Report 2556

TUDelft
Technische Universiteit Delft

STW   Nieuwe technologie
mogelijk maken

Delft University of Technology

Faculty of Mechanical, Maritime and Materials Engineering (3mE)

Mechanical Engineering: Sustainable Processes & Energy Technologies

Process & Energy department: Engineering Thermodynamics

CO_2-capture using liquid crystals: selectivity analysis for CO_2 capture from syngas

October 2012 – June 2013

Report: 2556

Author: ing. Ramaker, B.C.

Exam committee: Prof. dr. ir. Vlugt, T.J.H.
                           dr. ir. De Loos, Th. W.
                           dr. ir. Ter Horst, J.H.
                           dr. ir. Van den Broeke, P.
                           ir. De Groen, M.

Abstract

The current need to reduce CO_2 emission from power plant flue gas demands development of new and more energy efficient separation processes. Liquid crystals are a new class of solvents for CO_2 absorption; making use of a solubility switch between two phases. Solubility of CO_2 is higher in the isotropic liquid phase than in the structured liquid phase. Phase transition enthalpy between both phases is low and therefore CO_2 capture with liquid crystals has the potential to consume less energy in an absorption/desorption cycle than conventional CO_2 capture processes. Liquid crystals enable precombustion CO_2 capture at high pressures, hence the capture process can be used for CO_2 capture from syngas; gas mainly consisting of CO_2 and H_2. At this stage research is focused on ideal selectivity and especially on the solubility of CO_2 in liquid crystals. Literature study is conducted on experimental phase behaviour of liquid crystal like structures to validate the Predictive Soave-Redlich Kwong equation of state. The Predictive Soave-Redlich Kwong equation of state is used to predict phase behaviour of different liquid crystals with H_2 and CO_2 to identify the most promising molecular structures, resulting in a selectivity analysis. In the Thermodynamics Laboratory (Process & Energy department, TU Delft) the binary mixtures of pentyl cyanobipenyl, heptyloxy cyanobiphenyl, ethyl propyl bicyclohexyl, propyl butyl bicyclohexyl, hexyloxybenzylidene aminobenzonitrile and phenyl cyclohexyl with CO_2, and the binary mixtures of ethyl propyl bicyclohexyl, phenyl cyclohexyl and heptyloxy cyanobiphenyl with H_2 are measured using a Cailletet setup. Henry coefficients obtained from the experimental data indicate the solubility of the different structures. Accuracy of the bubblepoint curve prediction by the Predictive Soave-Redlich Kwong equation of state is higher for small molecular structures at relatively low temperatures. The vapour liquid equilibrium prediction has larger deviations for binary mixtures with acetate structures in combination with CO_2 and for all binary mixtures with H_2; however the bubblepoint curve order is maintained in the vapour liquid equilibrium prediction. The Predictive Soave-Redlich Kwong equation of state simulation predicts that highest solubility for both CO_2 and H_2 with bicyclohexyl based structures and the lowest with biphenyl based structures. From the Predictive Soave-Redlich Kwong equation of state simulation it is found that more polar structures increase the solubility of both CO_2 and H_2. The experimental results measured in the Cailletet setup underline the predictions made with the PSRK simulation and demonstrate that weakly polar structures (PCH-type) have a higher solubility of CO_2. Highly polar structures (7OCB) are also demonstrating high solubility of CO_2 in the Predictive Soave-Redlich Kwong equation of state simulation and experiments. Simulation of the experimental liquid crystals with the Predictive Soave-Redlich Kwong equation of state shows prediction of bicyclohexyl structures phase behaviour is more accurate than predicting phase behaviour of biphenyl and cyclohexylbenzene based structures.

Acknowledgement

First of all I would like to thank Mariette de Groen for her daily support and overall supervision, your devotion to the project was really motivational for me. Also the support and guidance from the weekly supervision of Theo de Loos was helpful for me. I would also like to thank Eugene Straver for his assistance in the Thermodynamics Laboratory and the whole ETh group for their support throughout my graduation. Finally I would like to thank my parents, girlfriend and friends for their support and patience.

Table of content

Nomenclature

Abbreviation	Description
CC	Carbon Capture
CCS	Carbon Capture and Storage
DDB	Dortmund Data Bank
DSC	Differential Scanning Calorimetry
EOS	Equation of State
GHG	Green House Gas
IGCC	Integrated Gasification Combined Cycle
IPCC	Intergovernmental Panel on Climate Change
LC	Liquid Crystal
MEA	Mono-Ethanol-Amine
ppm	parts per million (volume)
PSRK	Predictive Soave-Redlich-Kwong
SRK	Soave-Redlich-Kwong
SynVis	Synthetic Visual
UNIFAC	UNIQUAC Functional-group Activity Coefficients
UNIQUAC	Universal QuasiChemical
VLE	Vapor-Liquid Equilibrium
WGS	Water-Gas Shift

Symbol	Description	Unit
A_1	Constant used in EOS mixing rules	-
a	Attractive parameter in cubic EOS	$[dm^6 \cdot bar \cdot mol^{-2}]$
a_i	Attractive parameter in cubic EOS for component i	$[dm^6 \cdot bar \cdot mol^{-2}]$
b	Repulsive parameter in cubic EOS	$[dm^6 \cdot mol^{-1}]$
b_i	Repulsive parameter in cubic EOS for component i	$[dm^6 \cdot mol^{-1}]$
f_i	Fugacity of component i	$[Pa]$
f_i^{id}	Ideal (Lewis/Randall rule) fugacity component i	$[Pa]$
$\hat{f}_i$	Actual fugacity component i	$[Pa]$
F	Degree of Freedom	$[-]$
g^C	Combinatorial term UNIQUAC	$[-]$
g_o^E	Excess molar Gibbs energy at reference pressure	$[J \cdot mol^{-1}]$
g^R	Residual term UNIQUAC	$[-]$
G^E	Excess Gibbs energy	$[J \cdot mol^{-1}]$
H	Enthalpy	$[J \cdot mol^{-1}]$
H_i	Henry coefficient component i	$[Pa]$
N	Number of chemical species	$[-]$
N_{atoms}	Number of atoms in substance	$[-]$
N_k	Number of groups of type k in a molecule (first order groups)	$[-]$
pck	Group contributions for Joback method	$[-]$
P	Total pressure	$[Pa]$
P_i^{sat}	Saturation pressure of component i	$[Pa]$
$P_{C,i}$	Critical pressure component i	$[bar]$
q_i	Relative molecular surface area	$[-]$
r_i	Relative molecular volume	$[-]$
R	Gas constant	$[J \cdot mol^{-1} \cdot K^{-1}]$
tck	Group contributions for Joback method	$[-]$
T	Temperature	$[K]$

T_b	Atmospheric boiling point	$[K]$
$T_{C,i}$	Critical temperature component i	$[K]$
v	Molar volume	$[dm^3 \cdot mol^{-1}]$
x	Mole fraction	$[\text{-}]$
x_i	Liquid mole fraction of component i	$[\text{-}]$
y_i	Vapour mole fraction of component i	$[\text{-}]$
wt%	Mass percentage	$[\%]$

Greek symbol	**Description**	**Unit**
π	Number of phases	$[\text{-}]$
$\hat{\phi}_i$	Fugacity coefficient component i	$[\text{-}]$
γ_i	Activity coefficient of component i	$[\text{-}]$
τ_{ji}	Interaction parameter	$[\text{-}]$

Introduction

Warming of the climate system is evident, as is now clear from observations of increasing global average air and ocean temperatures, widespread melting of snow and ice and rising of the global average sea level [1]. Changes in atmospheric concentrations of greenhouse gases (GHGs) and aerosols, land cover and solar radiation alter the energy balance of the climate system. Global GHG emissions have grown since pre-industrial times, with an increase of 70% between 1970 and 2004 due to human activities [1]. Carbon dioxide (CO_2) is the most important anthropogenic GHG. Its annual emissions grew by about 80% between 1970 and 2004. Global increase in CO_2 concentration are primarily caused by fossil fuel use, with deforestation providing another significant but smaller contribution [1].

The atmospheric concentration of CO_2 has exceeded the natural range over the last 650,000 years by far [1]. To reduce the CO_2 emitted in the atmosphere, Carbon dioxide Capture and Storage (CCS) is essential [2]. The Intergovernmental Panel on Climate Change (IPCC) estimates a reduction of CO_2 emissions of 80-90% to the atmosphere for a modern conventional (postcombustion) power plant equipped with CCS technology [2]. CCS is a process consisting of the separation of CO_2 from industrial and energy-related sources, transport to a storage location and long-term isolation from the atmosphere. The concentration of CO_2 in the gas stream, the pressure of the gas stream and the fuel type are important factors in selecting the capture system [2]. This report focusses on the first part of CCS, carbon capture (CC).

Typical CC systems use postcombustion CC which uses an amine based solvent to capture CO_2 from flue gas by chemical absorption. This postcombustion CCS will increase the energy requirements of the power plant by 25-40% [2] due to regeneration of the solvent. Furthermore, cost analysis shows an increased cost of electricity of 0.01-0.07$/kWh relative to a plant without a CCS system [3]. For postcombustion CCS from flue gas major obstacles are: the low pressure of the flue gas (ca. 1 atmosphere), the low CO_2 concentration (15%) in the flue gas and CO_2 separation from a high volume stream of flue gas component gases, predominantly N_2 [2]. Therefore the energy producing industry is searching for a more energy efficient solvent for CC.

Another process for CC which is, at first glance, more energy efficient is precombustion capture; this avoids dealing with large quantities for flue gas at atmospheric pressure. Furthermore, because of the elevated pressure physical solvents can be used instead of chemical solvents. The use of liquid crystals (LCs) as physical absorbents for precombustion CC is considered as novel process for CC [4]. The LC consists of two distinct liquid phases, namely an isotropic liquid and structured (e.g. anisotropic) liquid phase. The solubility of CO_2 is higher in the isotropic liquid phase than in the structured liquid phase and phase transition enthalpy between both liquid phases is low, therefore has the potential to

consume less energy than conventional capture process. This capture process enables precombustion CC and therefore can be used in CO_2 capture from synthetic gas (syngas).

Focus of this report is on predicting the most promising LC structure for CC from syngas. Used methods to select the most promising LC structure are experiments, to research actual solubility of CO_2 and H_2, and simulation, to predict solubility of CO_2 and H_2 in different LC structures. For the simulation of phase behaviour the Predictive Soave-Redlich Kwong (PSRK) equation of state (EOS) is used.

1.0 Phase behaviour theory

1.1 Phase behaviour: phase theory

The phase rule of Gibbs for nonreacting systems [eq. 1.1] shows the number of variables that may be independently fixed in a system at equilibrium. The difference between the number of variables that characterizes the intensive state of the system and the number of independent equations is the number of variables that may be independently fixed [5]. To evaluate the degrees of freedom (F) of the system for a system containing N chemical species and π phases:

$$F = 2 - \pi + N \qquad\qquad 1.1$$

For a unary system ($N = 1$), with minimum of one phase ($\pi = 1$), the maximum degree of freedom is two [7], therefore phase behaviour of pure substances can be described by a single *P,T*-diagram. In figure 1.1 a typical *P,T*-diagram of a pure substance is shown. At the triple point the unary system ($N = 1$), with three-phases ($\pi = 3$), has zero dimensions and is in fact a point [5].
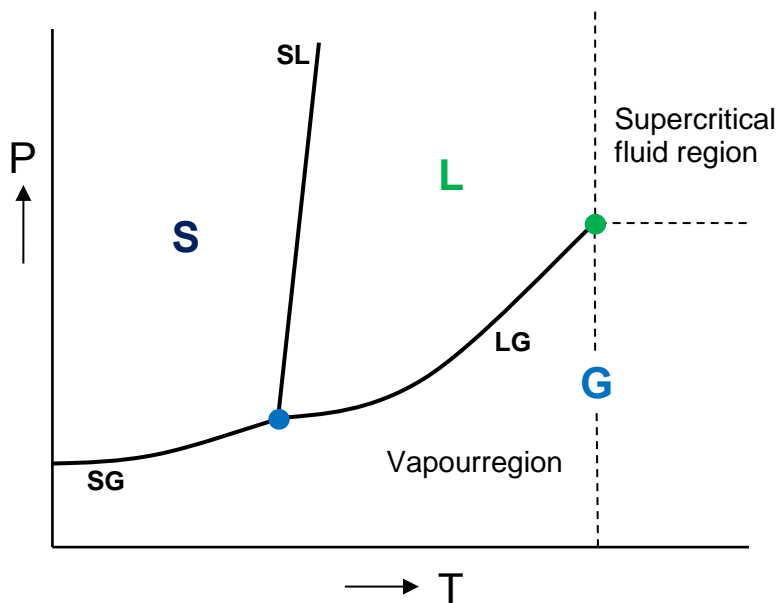
Figure 1.1: Typical *P,T*-diagram of a pure substance. Description of symbols used: (S) Solid phase, (L) Liquid phase, (G) Gas phase, (blue ●) triple point SLG, (green ●) critical point (P_c, T_c). SG-line is the sublimation curve, LG-line the vaporization curve and SL-line the fusion curve.

For a mixture of two components the degrees of freedom increase. For a binary mixture ($N = 2$), with minimum of one phase ($\pi = 1$), the maximum degree of freedom (F) is three, namely: pressure, temperature and mole fraction. These three dimensions can be projected in a three dimensional space; *P,T,x* projection.

1.2 Vapor-liquid equilibria

Vapor-liquid equilibria (VLE), in which the vapour phase is an ideal gas and the liquid phase is an ideal solution can be described by Raoult's law. The expression for Raoult's law [eq. 1.2] for component $i = 1,2,..,N$, is

$$y_i P = x_i P_i^{sat}$$

1.2

In which the x_i and y_i are respectively the liquid and vapour phase mole fraction are, P_i^{sat} the saturation pressure of the pure component i and P the total pressure on the system. The VLE line of a dilute binary mixture which is in the supercritical region is described by Henry's law [eq. 1.3]. Henry's law defines the solubility of the supercritical gas in the solvent by the Henry's constant. For ideal behaviour of binary systems Henry's law for component i is described with the following equation.

$$y_i P = x_i H_i$$

1.3

In which the Henry's coefficients (H_i) are found experimentally. Non ideal behaviour can be described with the residual Gibbs energy can be written as [eq. 1.4]

$$\bar{G}_i^R = \bar{G}_i - \bar{G}_i^{ig}$$

1.4

The residual Gibbs energy can be written as function of the fugacity coefficient [eq. 1.5]

$$\bar{G}_i^R = RT \ln \frac{\hat{f}_i}{y_i P}$$

1.5

The fugacity coefficient ($\hat{\phi}_i$) [eq. 1.6] of component i in a solution is described by

$$\hat{\phi}_i = \frac{\hat{f}_i}{y_i P}$$

1.6

The residual Gibbs energy can be rewritten as [eq. 1.7]

$$\bar{G}_i^R = RT \ln \hat{\phi}_i$$

1.7

The characteristic ideal solution behaviour is described by the Lewis/Randall rule [eq. 1.8]

$$\hat{f}_i^{id} = x_i f_i$$

1.8

From the expressions for the real Gibbs energy and the ideal Gibbs energy the excess Gibbs energy [eq. 1.8 & 1.9] can be calculated

$$\bar{G}_i^E = \bar{G}_i - \bar{G}_i^{id}$$

1.9

$$\bar{G}_i^E = RT \ln \frac{\hat{f}_i}{f_i^{id}} = RT \ln \frac{\hat{f}_i}{x_i f_i} \qquad 1.10$$

The activity coefficient (γ_i) [eq. 1.11] of component i in a solution is described by

$$\gamma_i = \frac{\hat{f}_i}{f_i^{id}} = \frac{\hat{f}_i}{x_i f_i} \qquad 1.11$$

The excess Gibbs energy can be described with the following equation [eq. 1.12]

$$\bar{G}_i^E = RT \ln \gamma_i \qquad 1.12$$

This shows that the activity coefficient is described by the ratio of the components actual fugacity and the ideal solution fugacity (given by the Lewis/Randall rule) [eq. 1.13]. If the activity coefficient is written as a function of measurable quantities and the fugacity and fugacity coefficient it becomes

$$\gamma_i = \frac{y_i \hat{\phi}_i P}{x_i f_i} \qquad 1.13$$

If fugacity coefficient $\hat{\phi}_i = 1$, then the activity coefficient can be written as [eq. 1.14]

$$\gamma_i = \frac{y_i P}{x_i f_i} \qquad 1.14$$
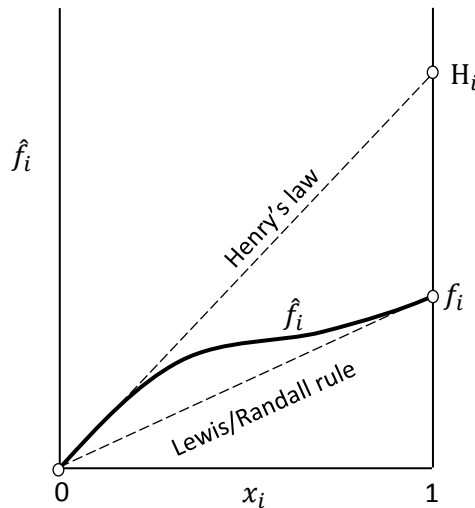
Figure 1.2: Composition dependence of liquid phase fugacity for component i in a binary solution at constant temperature and pressure. [5]

As can be seen in figure 1.2 the limit of $x_i \to 0$, $\hat{f}_i$ becomes zero. The ratio $\hat{f}_i/x_i$ is indeterminate in this limit, and with use of l'Hôpital's rule the equation becomes [eq. 1.15]

$$\lim_{x_i \to 0} \frac{\hat{f}_i}{x_i} = \left(\frac{d\hat{f}_i}{dx_i}\right)_{x_i=0} = H_i \qquad \text{1.15}$$

This defines the Henry constant as the limiting slope of the $\hat{f}_i, x_i$ curve at vicinity of $x_i = 0$. The equation of the tangent line expressed with Henry's law becomes [eq. 1.16]

$$\hat{f}_i = x_i H_i \qquad \text{1.16}$$

The Henry coefficients for a non-ideal mixture can then be calculated with

$$H_i = \frac{\hat{f}_i}{x_i} \qquad \text{1.17}$$

1.3 Phase behaviour of Liquid Crystals

The physical properties of a typical liquid phase are equal in all directions (isotropic) due to the free and random molecular motion in the fluid, in contrast: typical liquid crystals (LCs) consist two distinct liquid phases. The LC liquid phase consists of an isotropic liquid phase and a structured (anisotropic) liquid phase. For an anisotropic phase, physical properties like mechanical, electrical, magnetic and optical properties can vary according to the direction measured. In figure 1.3 a typical *P,T*-diagram of a pure LC shows the four phases, the two triple points (blue and red) and the critical point (green). The LC's structured phase is a condensed phase, either nematic (N) and/or smectic (Sm), and is located between the solid phase (S) and the isotropic liquid phase (I) in a phase diagram. [7]
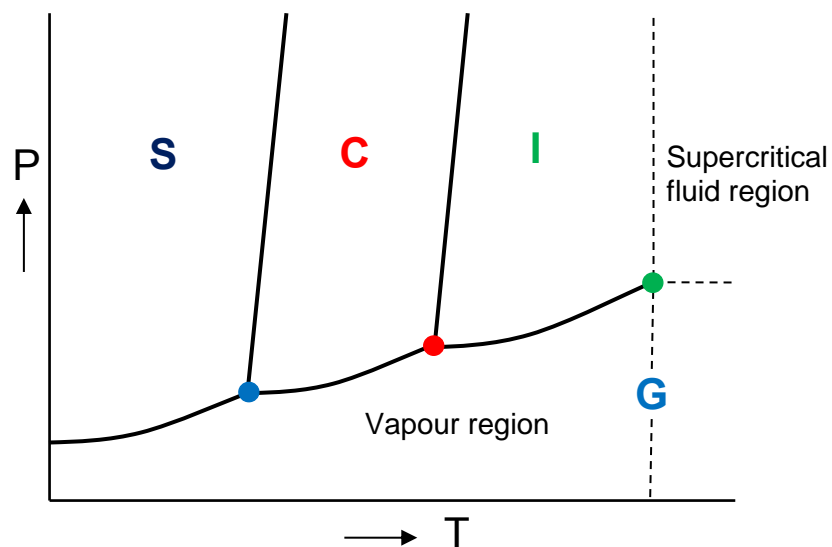
Figure 1.3: Typical *P,T*-diagram of a pure liquid crystal. Description of symbols used: (S) Solid phase, (C) Condensed liquid phase, (I) Isotropic liquid phase, (G) Gas phase, (blue ●) triple point SCG, (red ●) triple point CIG, (green ●) critical point (P_c, T_c).

Focus of the Cailletet experimental measurements is on the condensed liquid phase (C) and the isotropic liquid phase (I) behaviour due to importance of these in CC process. The phase diagram of a binary liquid crystal can be described with a three-dimensional space with pressure, temperature and composition as variables. To measure a two phase equilibria curve two of the three degrees of freedom needed to be controlled, while one is variable. In the Thermodynamics Laboratory (Process & Energy department, TU Delft) a visual observation of phase transitions can be made using an isopleth in the Cailletet experiment while controlling the pressure and temperature of the binary mixture. When keeping the temperature or pressure constant, the other is the controlled variable.

Figure 1.4 shows a typical P,T and T,x projection of a binary mixture of CO_2 and a typical LC. In the figure the pure LC (P,T projection) phase transitions are indicated with C↔I (CI), C↔G (CG) and I↔G (IG) [4]. The three phase point of the pure LC is indicated with (▲). For the binary mixture the three phase curve (CIG) is constructed as well as the phase transition curves. The indicated points can be used to construct an isopleth (P,T-diagram) or an isobar (T,x-diagram). The condensed phase of the LC, denoted with C, is either nematic and/or smectic. [7]
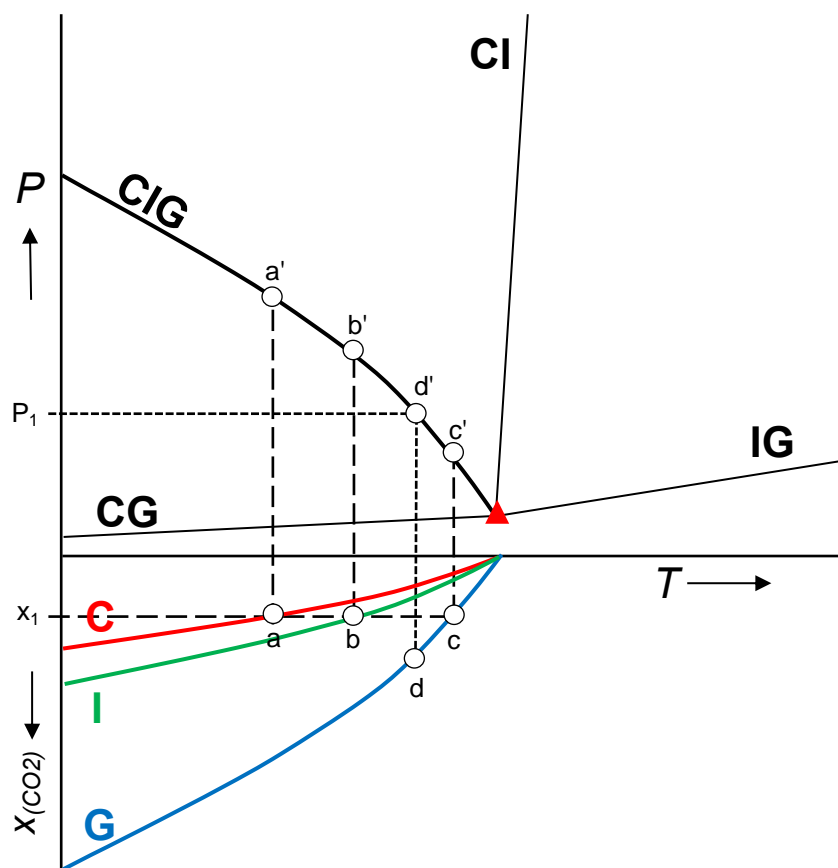
Figure 1.4: Schematic P,T,x projection of a binary mixture of LC with CO_2. Description of symbols used: (C) Condensed liquid phase, (I) Isotropic liquid phase, (G) Gas phase, (▲) triple point. The labels a, b, c, a', b' and c' are used to indicate phase behaviour of an isopleth or isobar.

LCs have a structured liquid phase (e.g. anisotropic) in which the solubility of CO_2 is lower than in the isotropic phase. From figure 1.4 a *P,T*-diagram can be generated (isopleth) at composition x_1 at which the corresponding point a', b' and c' are used to describe the three phase curve (figure 1.5). In figure 1.5 the *P,T*-diagram a typical binary mixture of LC and CO_2 is shown.
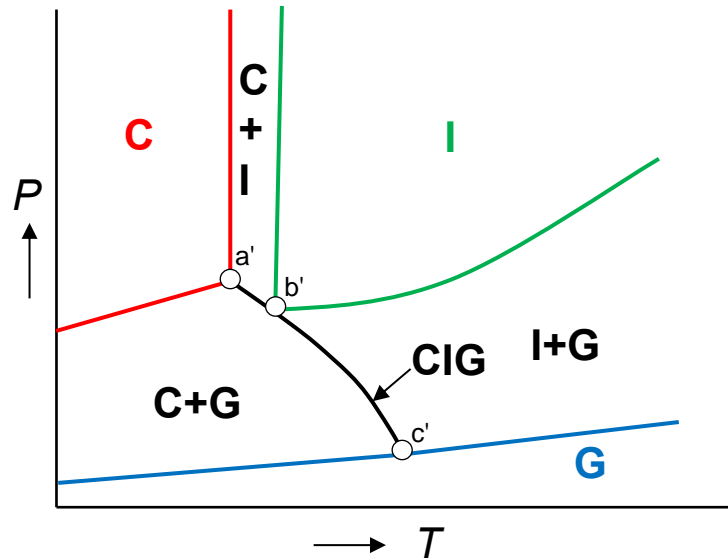
Figure 1.5: Typical *P,T*-diagram of a binary mixture of liquid crystal with CO_2. Description of symbols used: (C) Condensed phase, (I) Isotropic phase, (G) Gas phase, (CIG) three-phase line.

In figure 1.5 the solubility difference between the isotropic liquid phase (I) and the structured liquid phase (C) can be observed. Between the isotropic liquid phase (I) and the structured liquid phase (C) a two phase area is present (C+I). The isotropic liquid phase (I) and the gas phase (G) are separated with a two phase area (I+G). The curve represented with I+G↔I is the bubblepoint curve and the curve represented with I+G↔G the dew point curve. The structured liquid phase (C) and the gas phase (G) are also separated with a two-phase area (C+G). The curve represented with C+G↔C is the bubblepoint curve and the curve represented with C+G↔G the dew point curve. In between the two phase areas the three-phase curve (CIG) is present.

In figure 1.6 an isobaric projection (*T,x*-diagram) of figure 1.4 is constructed at pressure P_1. The dotted at P_1 line intercepts with the three-phase equilibrium curve (CIG) at point d', from the three-phase curve the pure LC phase transitions points can be constructed. The corresponding point (d) found in the *T,x* projection is shown in figure 1.6. The pure LC phase transitions; isotropic liquid phase transition (I) and the structured liquid phase transition (C), can be obtained from the corresponding composition (x_{CO_2}) in figure 1.4.
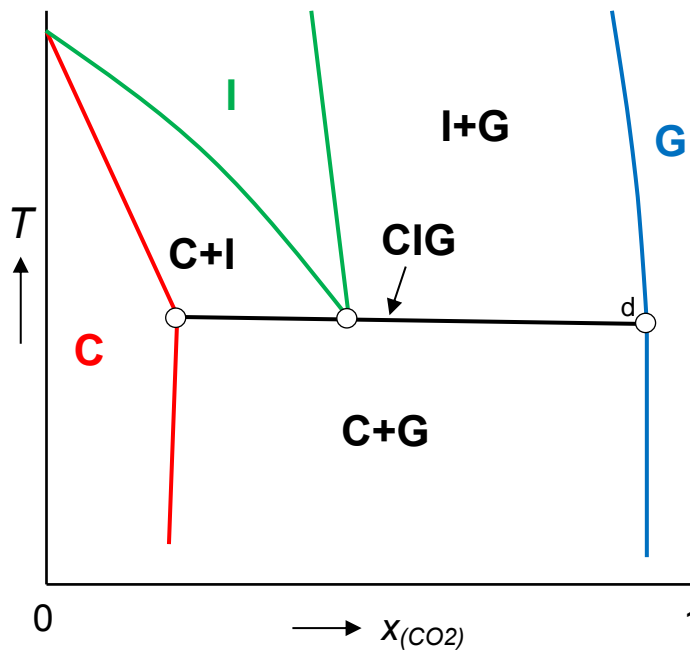
Figure 1.6: Typical *T,x*-diagram of a liquid crystal (C) with CO_2 including the intended CO_2 capture process (purple box process). Description of symbols used: (C) Condensed phase, (I) Isotropic phase, (G) Gas phase, (CIG) three-phase line.

In figure 1.6 the phase behaviour of a typical binary mixture of LC with CO_2 is shown. Above the three-phase equilibrium line (CIG) the structured liquid phase (C), the isotropic liquid phase (I) and the gas phase (G) are separated with two two-phase areas: (C+I) and (I+G). Below the three-phase equilibrium line (CIG) and on the right of the structured liquid phase (C) a two-phase area is present (C+G). This two-phase area (C+G) separates the structured liquid phase (C) and the gas phase (G) underneath the three-phase equilibrium line (CIG).

In the nematic phase the molecules maintain a preferred orientational direction as they diffuse, while in the smectic phase the LCs have layered structures; stacks of two-dimensional liquids are formed. Both nematic and smectic condensed phases are shown in respectively figures 1.7 and 1.8, besides the visual appearance the nematic phase behaves more like a low viscous liquid while the smectic phase behaves more like a high viscous liquid. [8] [9] [12]

Figure 1.7: Experimental setup: Cailletet tube (including magnetic ball stirrer). Phase transition from nematic phase (left) to isotropic liquid phase (right)
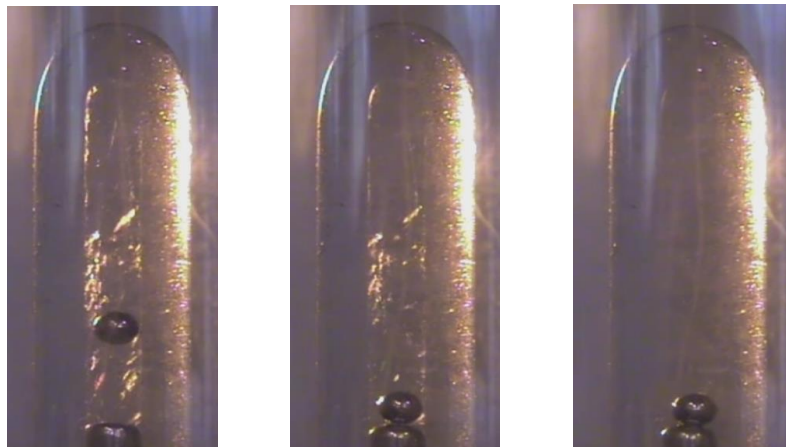
Figure 1.8: Experimental setup: Cailletet tube (including magnetic ball stirrer). Phase transition from smectic phase (left) to isotropic liquid phase (right)

1.4 Carbon capture process theory

The four types of CO_2 capture processes are; postcombustion (capture from flue gas), precombustion (capture after steam reforming), oxyfuel (capture from single stream) and carbon capture from industrial processes (i.e. natural gas sweetening, ammonia production and steel production). To neither drastically increase global demand in the chemical nor saturating the market with reactant the chemical used for CO_2 capture must be regenerable making the key challenge in a CO_2 capture process the energy needed for regeneration. [2] [3]

The CCS process includes the capture, transport and long term isolation of CO_2 (figure 1.9). Typical postcombustion and precombustion CC processes are equipped with a chemical absorbent material or a physical absorbent material [3]. The chemical absorbent used in conventional postcombustion CCS processes is monoethanolamine (MEA). The MEA is dissolved in water (typically 25-30 wt %) [2] and fed on the top of the absorption column while the CO_2 is fed at the bottom. At a temperature of approximately 40°C [2] the CO_2 reacts with the chemical forming organic compounds (carbamates). Heat of formation associated with carbamates production is high, leading to considerable energy consumption for regeneration of the solvent. The CO_2-rich liquid passes from the absorber column to a stripping tower where by heating the mixture (temperature 100-140°C, pressure just above atmospheric) [2] the CO_2 is released, and the MEA solution is regenerated. The energy increase retrofitting existing coal-fired power plants with aqueous MEA has been estimated as 25 up to 40% [2]. To overcome this large energy increase in fossil fuel fired power plants employed with CO_2 capture a less energy consuming process is needed.

Figure 1.9: Power plant equipped with Carbon Capture and Storage (CCS). Power plant equipped with pre- or postcombustion carbon capture process, transportation pipeline and underground CO_2 storage facility.

A typical schematic representation of precombustion CO_2 capture is shown in figure 1.10, this process is referred to as an Integrated Gasification Combined Cycle (IGCC). Syngas, a synthetic gas consisting mainly of CO, CO_2 and H_2, is the result of gasification of a fuel source. With use of a water-gas shift (WGS) reaction (part of steam reforming) the oxygen from the additionally fed H_2O shifts CO into

CO_2 increasing the amount of H_2 and CO_2 in the syngas. After a WGS reaction precombustion capture of CO_2 can be employed. If the gasified fuel requires sulphur removal, this can be performed after the WGS. From this gas mixture, the CO_2 can be captured with a physical absorbent to obtain a H_2 rich gas and to avoid direct CO_2 emissions after combustion. The single direct emission is H_2O (vapor) which is expected to condense at atmospheric pressure and temperature taking no part on the overall increase of GHG in the atmosphere [2]. The typical composition and conditions of both processes are shown in table 1.1, showing that precombustion capture will have to deal with an increased mass flow of CO_2 at elevated pressure in contrast to postcombustion capture. Typical compositions and conditions of postcombustion and precombustion gas streams are shown in table 1.1.
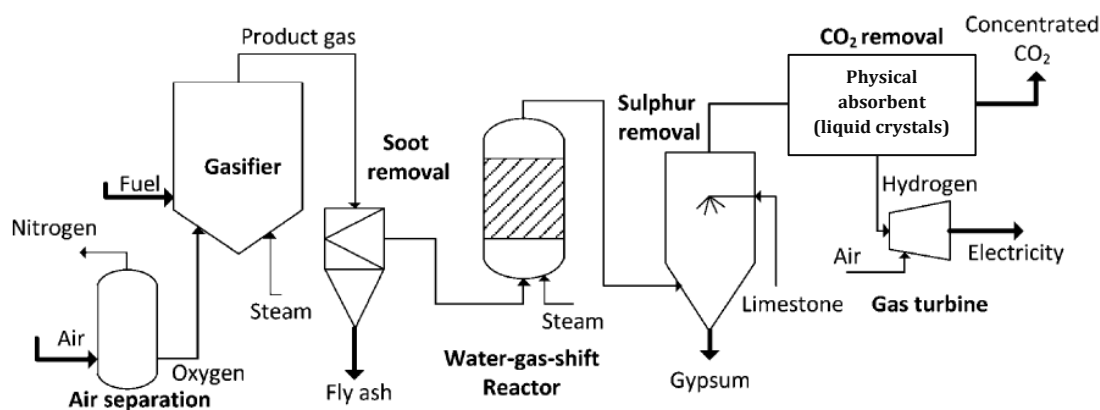
Figure 1.10: Schematic representation of a precombustion CO_2 capture system [43].

Table 1.1: Typical composition and conditions of gases in postcombustion and precombustion processes. [3]

| Composition	Postcombustion	Precombustion[1]
CO_2	15-16 [wt %]	35.5 [wt %]
H_2O	5-7 [wt %]	0.2 [wt %]
H_2	-	61.5 [wt %]
O_2	3-4 [wt %]	-
CO	20 [ppm]	1.1 [wt %]
N_2	70-75 [wt %]	0.25 [wt %]
SO_x	<800 [ppm]	-
NO_x	500 [ppm]	-
H_2S	-	1.1 [wt %]
Conditions		
Temperature	323-348 [K]	313 [K]
Pressure	0.1 [MPa]	3 [MPa]

[1]After water-gas shift reaction.

Main advantages of precombustion over postcombustion CO_2 capture are that the process is at higher pressure and has to deal with a smaller volume gas stream. The advantage of using precombustion

with a physical absorbent, like LCs, is that energy demand for phase transition is much lower than for regeneration reaction [40], therefore has the potential to be more energy efficient than conventional amine-based (MEA) capture process [4]. Drawback of precombustion CC is that it is only applicable to new power plants because of the integration with the combustion process. Another major challenge is the combustion of H_2 as fuel in gas turbines.

In the proposed absorption process of precombustion CC the CO_2 is captured at constant high pressure before combustion. In figure 1.11 the T,x-diagram of the proposed CC process with LC is shown, in the process CO_2 is absorbed and desorbed (as indicated in the purple process box).
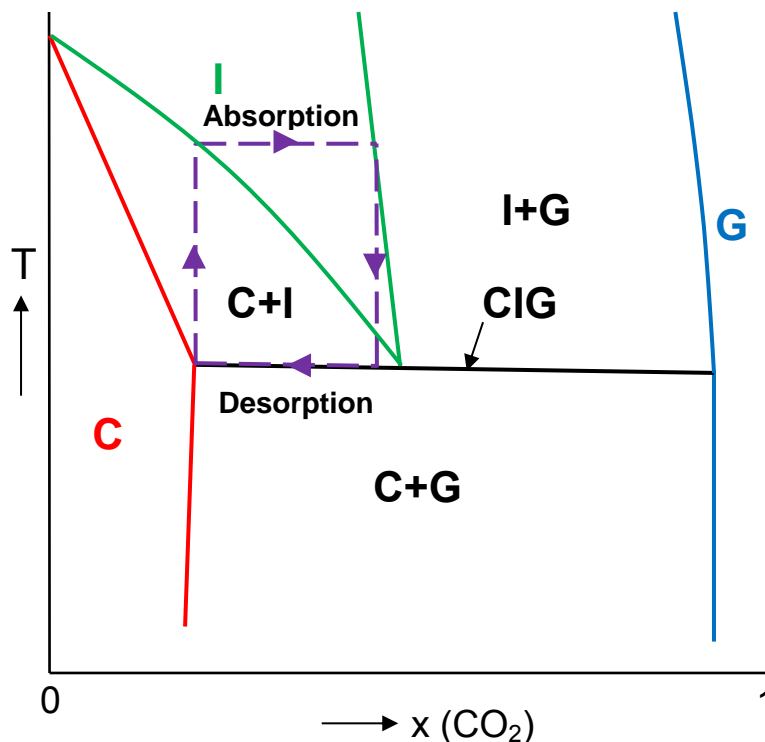
Figure 1.11: Schematic T,x-diagram of a liquid crystal (C) with CO_2 including the intended CO_2 capture process (purple box process). Description of symbols used: (C) Condensed phase, (I) Isotropic phase, (G) Gas phase, (CIG) three-phase line.

CO_2 is absorbed in the isotropic (I) phase and desorbed at the three-phase equilibrium (CIG). From the T,x-diagram it is clear that the absorption process depends on the width of the two-phase area (C+I) and the slopes of the CI curves.

The difference between the C→C+I and C+I→I curves depends on the phase transition enthalpy and can be calculated with a modified van 't Hoff law [eq. 1.18]:

$$\frac{dx_{CO_2}^C}{dT} - \frac{dx_{CO_2}^I}{dT} = \frac{\Delta_{tr}H}{R \cdot T_{tr}^2}$$

1.18

In which $\Delta_{tr}H$ is the condensed to isotropic liquid phase transition enthalpy, $x_{CO_2}^C$ and $x_{CO_2}^I$ the mole fractions of CO_2, respectively in the condensed and isotropic phase, T the temperature, T_{tr} the transition temperature and R the gas constant. When the phase transition enthalpy is high and the phase transition temperature low the proposed capture process has low energy requirement and high capture capacity.

1.5 Thermodynamic model: Predictive Soave-Redlich-Kwong Equation of State

The PSRK EOS is used because it is a predictive EOS for systems with supercritical components, such as CO_2 and H_2 in a capture process. The Predictive Soave-Redlich-Kwong (PSRK) [eq. 1.19] equation of state is used to model the bubblepoint line the binary mixtures of LC and CO_2 or H_2. The PSRK EOS uses the UNIFAC group contribution to predict phase behaviour while the cubic SRK EOS and gives accurate results for VLE of apolar or slightly polar mixtures [13].

$$P = \frac{RT}{v-b} - \frac{a}{v(v+b)} \qquad 1.19$$

Two modifications are necessary to predict the VLE for both polar and apolar systems [13]. The first modification incorporates the temperature dependence of the pure component parameter a. This makes the EOS sufficiently accurate for polar as well as apolar substances. The expression by Mathias and Copeman [13] is used to modify the EOS to fit polar components.

$$a_i = 0.42748 \frac{R^2 T_{C,i}^2}{P_{C,i}} f(T) \qquad 1.20$$

The second modification is linking the mixture rule of parameter a, which links the parameter to the excess Gibbs energy (g_o^E) at zero pressure [13]. The UNIFAC method is used to calculate the excess Gibbs energy.

$$a = b \left[\frac{g_o^E}{A_1} + \sum x_i \frac{a_i}{b_i} + \frac{RT}{A_1} \sum x_i \ln \frac{b}{b_i} \right] \qquad 1.21$$

$$b = \sum x_i b_i \qquad 1.22$$

$$b_i = 0.08664 \frac{RT_{C,i}}{P_{C,i}} \qquad 1.23$$

To estimate the critical points of structures the method of Joback is used [41], which uses group contribution schemes. The relations for the critical properties are:

$$T_c(K) = T_b \left[0.584 + 0.965 \left(\sum_k N_k(tck) \right) - \left(\sum_k N_k(tck) \right)^2 \right]^{-1} \qquad 1.24$$

$$P_c(bar) = \left[0.113 + 0.0032 N_{atoms} - \sum_k N_k(pck) \right]^{-2} \qquad 1.25$$

The UNIFAC method is a predictive method based on the UNIQUAC equation of state. The UNIQUAC equation [eq. 1.27] divides the Gibbs excess energy in two additive parts of g. This equation is the combination of g^C, which is the combinatorial term and g^R, which is the residual term. The term g^C contains pure-specie parameters only while g^R incorporates for the binary mixture parameters.

$$g \equiv \frac{G^E}{RT} \qquad\qquad 1.26$$

$$g = g^C + g^R \qquad\qquad 1.27$$

$$g^C = \sum_i x_i \ln\frac{\Phi_i}{x_i} + 5\sum_i q_i x_i \ln\frac{\theta_i}{\Phi_i} \qquad\qquad 1.28$$

$$g^R = -\sum_i q_i x_i \ln\left(\sum_j \theta_j \tau_{ji}\right) \qquad\qquad 1.29$$

In these equations the following parameters are defined.

$$\Phi_i \equiv \frac{x_i r_i}{\sum_j x_j r_j} \qquad\qquad 1.30$$

$$\theta_i \equiv \frac{x_i q_i}{\sum_j x_j q_j} \qquad\qquad 1.31$$

In this equation [eq. 1.30 & 1.31] the pure specie parameter r_i is the relative molecular volume and q_i the relative molecular surface area. The temperature dependence of the equation [1.29] is found in the UNIQUAC interaction parameter [eq. 1.32].

$$\tau_{ji} = exp\frac{-(u_{ji} - u_{ii})}{RT} \qquad\qquad 1.32$$

In the UNIQUAC method these interaction parameters u_{ii} and u_{ji} are obtained by fitting this equation to experimental data of molecule i and j. The UNIFAC group interaction parameters are used in the UNIFAC method, these interaction parameters are published in the Dortmund Data Bank (DDB) [27-39] literature.

When using the equation for the Gibbs excess energy [eq. 1.34] the equation for the pure component activity coefficient in a binary mixture can be rewritten [eq. 1.35].

$$\ln \gamma_i = \left[\frac{\partial (nG^E/RT)}{\partial n_i} \right]_{P,T,n_j}$$

1.33

$$\frac{G^E}{RT} = \sum_i x_i \cdot \ln \gamma_i$$

1.34

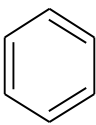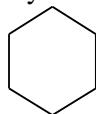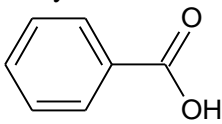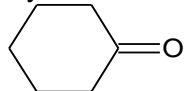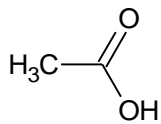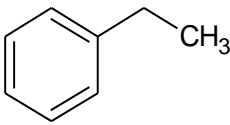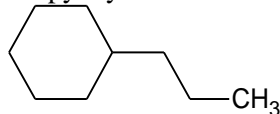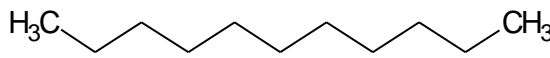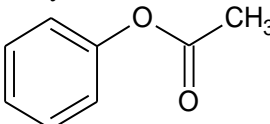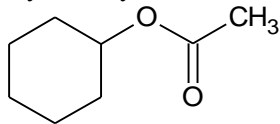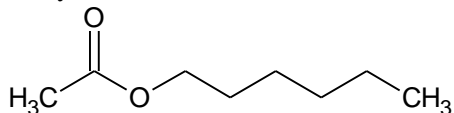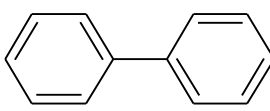$$\ln \gamma_i = \ln \gamma_i^C + \ln \gamma_i^R$$

1.35

From this equation the activity coefficient of the components can be determined.

2.0 Predictive Soave-Redlich Kwong Equation of State validation with literature data

The VLE predictions by the PSRK EOS in Aspen are validated with experimental literature data. The VLE data also allows indication for CO_2 and H_2 solubility of aromatic, cyclic and hydrocarbon chain structures. Literature is researched for (high pressure) Fluid Phase Equilibria published in the years: 1988-2008. From this published data binary mixtures of the structures in combination with CO_2 and H_2 are filtered. The literature used is found in references 14-25.

Table 2.1: Chemicals used in literature experiments. Left column contains benzene ring(s), middle column contains a cyclohexane ring and the right column contains a hydrocarbon chain.

Name, structure	Name, structure	Name, structure
Benzene	Cyclohexane	Acetonitrile
Methyl benzoate	Cyclohexanone	Acetic acid
Ethylbenzene	Propyl cyclohexane	Decane
Phenyl acetate	Cyclohexyl acetate	Hexyl acetate
Biphenyl		Ethanol

To compute the bubblepoint curve Aspen Plus was used incorporating the PSRK EOS. The LC structures are inserted by their molecular structure and the included UNIFAC groups. This enables Aspen to calculate the critical points, using the Joback method [41], and the bubblepoint curve using the PSRK EOS. The compatibility of the interacting groups and gas is checked in the PSRK data from Dortmund Data Bank (DDB) [27-39]. From *P,x*-diagram generated in Aspen a bubblepoint line can be obtained.

2.1 PSRK EOS modeling experimental data

The bubblepoint curves found in the literature are modelled in Aspen using the PSRK to validate the accuracy of the EOS. Composition and temperature are obtained from literature, bubblepoint pressure is generated by Aspen.
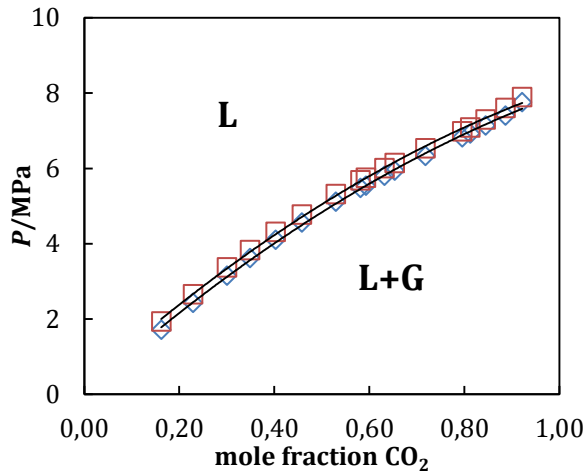
Figure 2.1: P,x-diagram benzene + CO_2 at T=315.45 K (Appendix G.1). Description of symbols used: (blue ◇) experimental data [15], (red □) PSRK simulation.
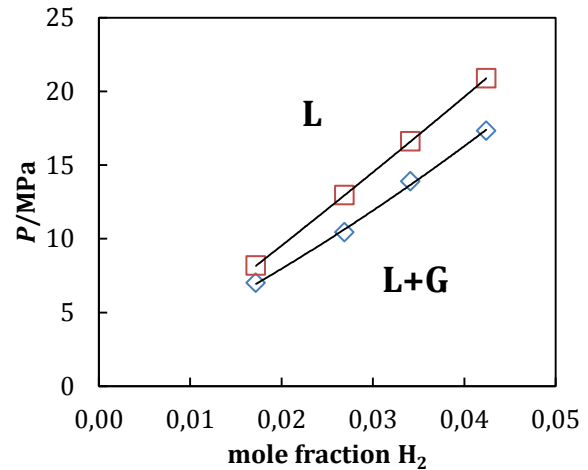
Figure 2.2: P,x-diagram benzene + H_2 at T=295 K (Appendix G.2). Description of symbols used: (blue ◇) experimental data [22], (red □) PSRK simulation.

In figure 2.1 and 2.2 experimental and simulation data of binary mixtures of benzene respectively with CO_2 and H_2 from literature [15] [22] is shown. In the binary mixture of benzene with CO_2 the experimental data trend is overpredicted with the PSRK simulation, it does follow the experimental values with an almost constant deviation. The binary mixture of benzene with H_2 is also overpredicted from the experimental data with the PSRK, when mole fraction of H_2 increases the deviation increases. When comparing the experimental bubblepoint curves of CO_2 and H_2 in benzene it can be observed that H_2 in combination with benzene has a higher bubblepoint pressure.
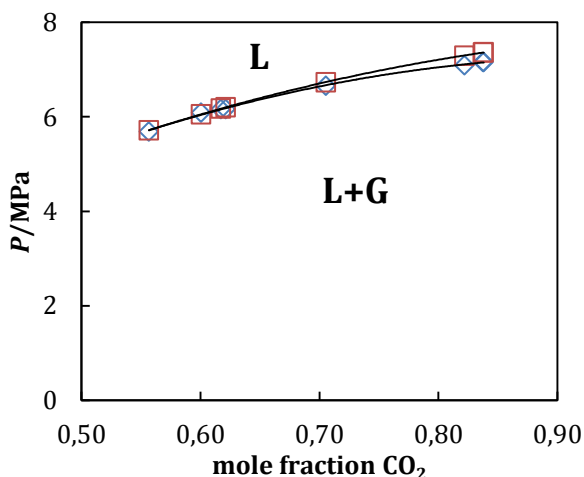
Figure 2.3: *P,x*-diagram ethylbenzene + CO_2 at T=313.2 K (Appendix G.4). Description of symbols used: (blue ◇) experimental data [14], (red ☐) PSRK simulation.

Figure 2.4: *P,x*-diagram ethylbenzene + H_2 at T=295 K (Appendix G.3). Description of symbols used: (blue ◇) experimental data [22], (red ☐) PSRK simulation.

In figure 2.3 and 2.4 experimental and simulation data of binary mixtures of ethylbenzene with CO_2 and H_2 from literature [14] [22] are shown, both are overpredicted by the PSRK EOS. In the binary mixture of ethylbenzene with CO_2 the experimental data trend is followed with the PSRK simulation, with only a small deviation. The deviation in the binary mixture of ethylbenzene with H_2 from the experimental data with the PSRK increases when the mole fraction H_2 increases. When comparing the bubblepoint line of CO_2 and H_2 in ethylbenzene it can be observed that H_2 in combination with ethylbenzene is much higher. The pressure of the bubblepoint curve of ethylbenzene with H_2 is lower compared to that of benzene with H_2.
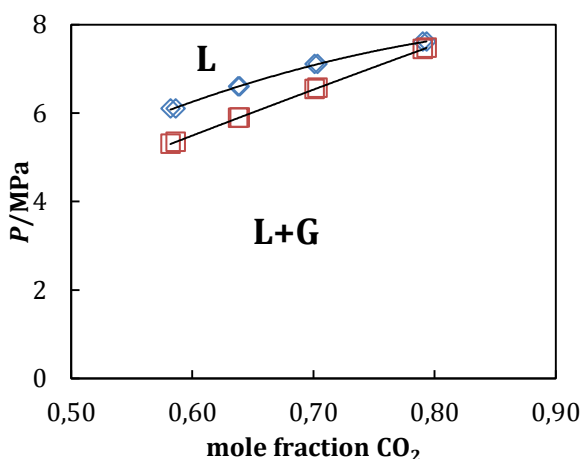
Figure 2.5: *P,x*-diagram methyl benzoate + CO_2 at T=313.1 K (Appendix G.5). Description of symbols used: (blue ◇) experimental data [20], (red ☐) PSRK simulation.

Figure 2.6: *P,x*-diagram phenyl acetate + CO_2 at T=333.15 K (Appendix G.6). Description of symbols used: (blue ◇) experimental data [17], (red ☐) PSRK simulation.

In figure 2.5 experimental and simulation data of binary mixtures of methyl benzoate with CO_2 from literature [20] is shown. In the binary mixture of methyl benzoate with CO_2 the experimental data

trend is not followed and underpredicted with the PSRK simulation, generating a linear bubblepoint line. In figure 2.6 experimental and simulation data of binary mixtures of phenyl acetate with CO_2 from literature [17] is shown. In the binary mixture of phenyl acetate with CO_2 the experimental data trend is followed but underpredicted with the PSRK simulation, the deviation increases at higher mole fraction.
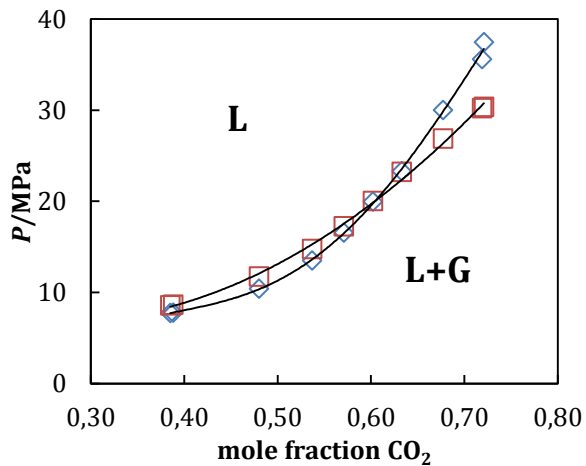
Figure 2.7: *P,x*-diagram biphenyl + CO_2 at T=333.2 K (Appendix G.7). Description of symbols used: (blue ◇) experimental data [25], (red □) PSRK simulation.

In figure 2.7 experimental and simulation data of binary mixture of biphenyl with CO_2 from literature [25] is shown. In the binary mixture of biphenyl with CO_2 the experimental data trend of a parabola is generated with the PSRK simulation, however the curve deviates from the experimental values. The bubblepoint curve is overpredicted for CO_2 mole fractions up to 0.60; afterwards the bubblepoint curve is underpredicted.
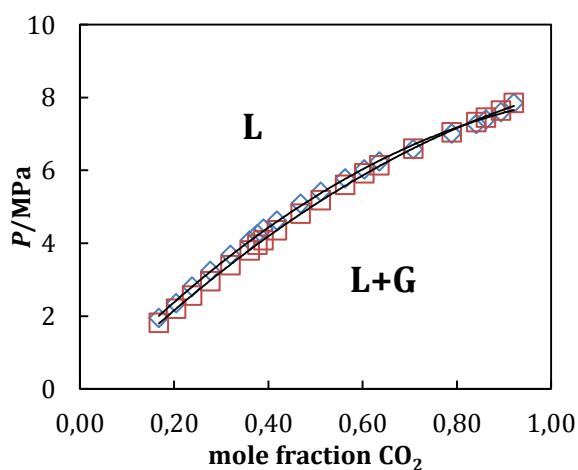
Figure 2.8: *P,x*-diagram cyclohexane + CO_2 at T=315.45 K (Appendix G.8). Description of symbols used: (blue ◇) experimental data [15], (red □) PSRK simulation.
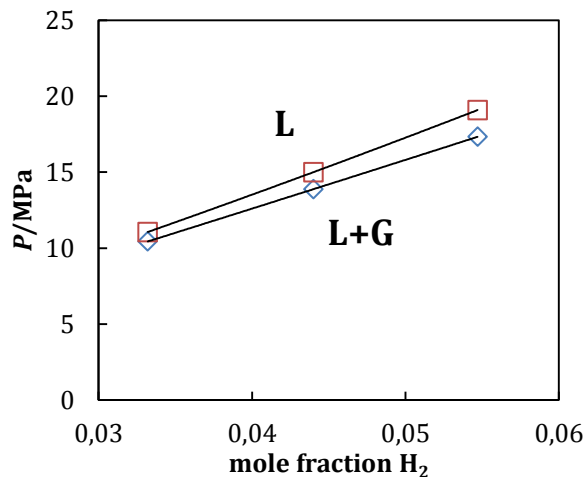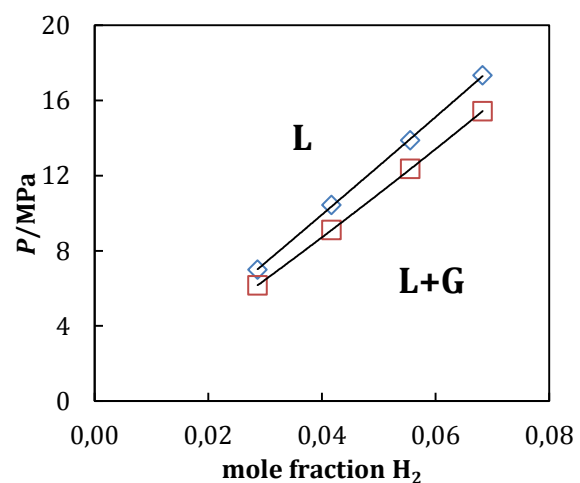
Figure 2.9: *P,x*-diagram cyclohexane + H_2 at T=295 K (Appendix G.9). Description of symbols used: (blue ◇) experimental data [22], (red □) PSRK simulation.

In figure 2.8 and 2.9 experimental and simulation data of binary mixtures of cyclohexane respectively with CO_2 and H_2 from literature [15] [22] is shown. In the binary mixture of cyclohexane with CO_2 the experimental data trend is predicted correctly with the PSRK prediction, with only a small deviation. The deviation in the binary mixture of cyclohexane with H_2 from the experimental data with the PSRK increases when the mole fraction H_2 increases. Both bubblepoint lines are underpredicted with the PSRK. When comparing the bubblepoint line from CO_2 and H_2 in cyclohexane it can be observed that the bubblepoint pressure of H_2 in combination with cyclohexane is much higher.
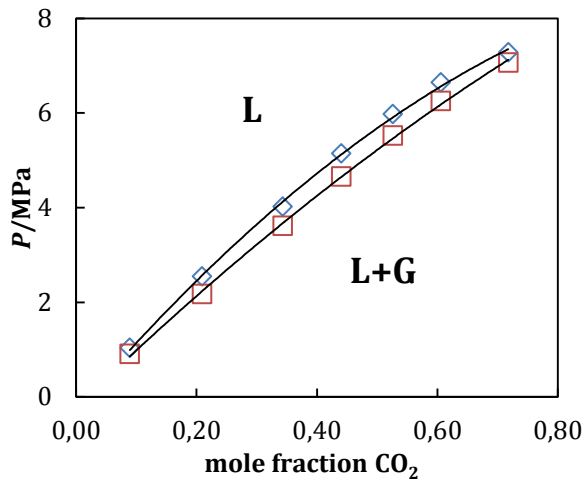
Figure 2.10: *P,x*-diagram propyl cyclohexane + CO_2 at T=313.1 K (Appendix G.11). Description of symbols used: (blue ◇) experimental data [18], (red □) PSRK simulation.
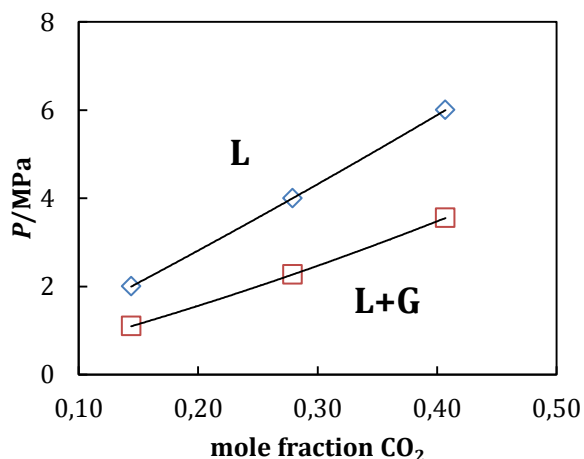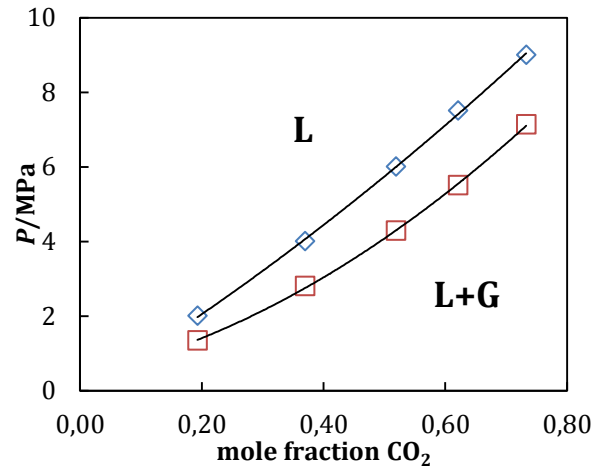
Figure 2.11: *P,x*-diagram cyclohexyl acetate + CO_2 at T=333.15 K (Appendix G.12). Description of symbols used: (blue ◇) experimental data [17], (red □) PSRK simulation.

In figure 2.10 experimental and simulation data of binary mixtures of propyl cyclohexane with CO_2 from literature [18] is shown. In the binary mixture of propyl cyclohexane with CO_2 the experimental data trend is followed and underpredicted with the PSRK simulation (parabola), with largest deviation in the middle of the parabola. In figure 2.11 experimental and simulation data of binary mixtures of cyclohexyl acetate with CO_2 from literature [17] is shown. In the binary mixture of cyclohexyl acetate with CO_2 the experimental data trend is followed and underpredicted with the PSRK simulation, however the curvature at low mole fraction deviates from the experimentally found values.
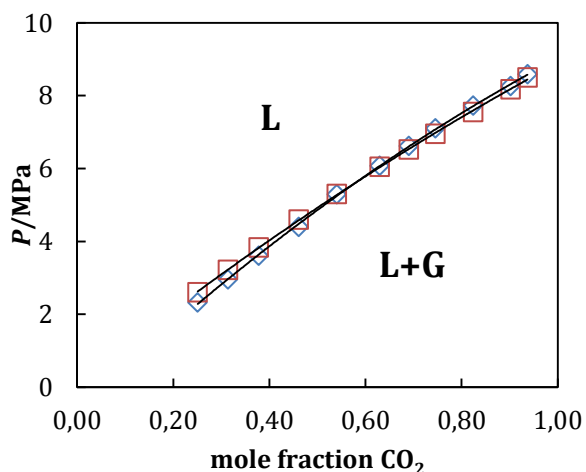
Figure 2.12: *P,x*-diagram acetonitrile + CO_2 at T=318.45 K (Appendix G.13). Description of symbols used: (blue ◇) experimental data [15], (red □) PSRK simulation.
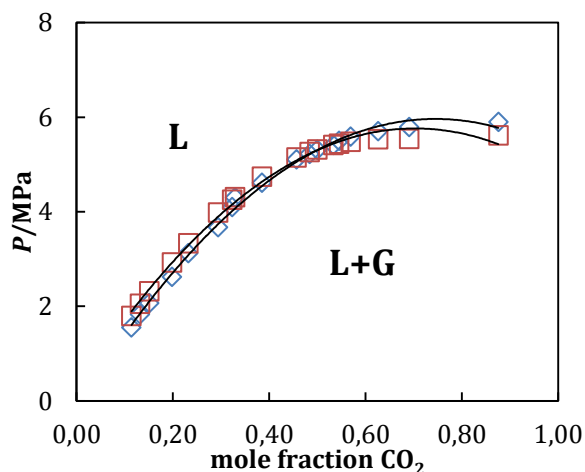
Figure 2.13: *P,x*-diagram ethanol + CO_2 at T=298.15 K (Appendix G.15). Description of symbols used: (blue ◇) experimental data [16], (red □) PSRK simulation.

In figure 2.12 experimental and simulation data of binary mixtures of acetonitrile with CO_2 from literature [15] is shown. In the binary mixture of acetonitrile with CO_2 the experimental data trend is followed with the PSRK simulation, with only a small deviation. The PSRK overpredicts the bubblepoint line until 0.55 mole fraction CO_2, at higher mole fractions of CO_2 the PSRK under predicts the bubblepoint line. In figure 2.13 experimental and simulation data of binary mixtures of ethanol with CO_2 from literature [16] is shown. In the binary mixture of ethanol with CO_2 the experimental data trend is followed with the PSRK simulation with only a small deviation. The PSRK over predicts the bubblepoint line for CO_2 mole fractions under 0.53 and under predicts for mole fractions larger than 0.53.
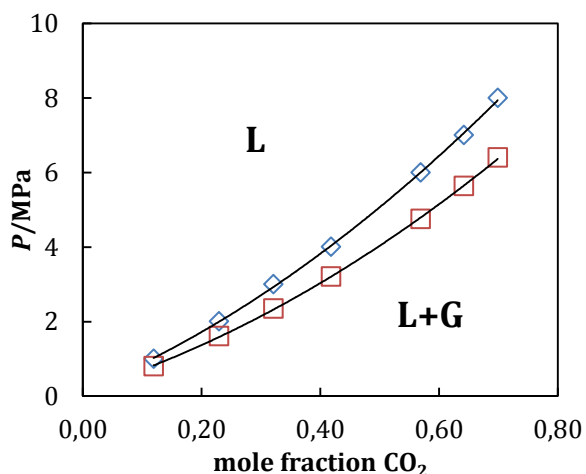
Figure 2.14: *P,x*-diagram hexyl acetate + CO_2 at T=333.15 K (Appendix 14). Description of symbols used: (blue ◇) experimental data [17], (red □) PSRK simulation.
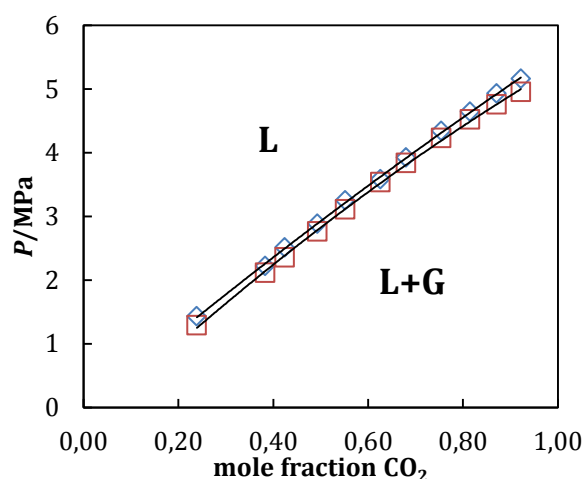
Figure 2.15: *P,x*-diagram cyclohexanone + CO_2 at T=290.8 K (Appendix G.10). Description of symbols used: (blue ◇) experimental data [19], (red □) PSRK simulation.

In figure 2.14 experimental and simulation data of binary mixtures of hexyl acetate with CO_2 from literature [17] is shown. In the binary mixture of hexyl acetate with CO_2 the experimental data trend is followed and underpredicted with the PSRK simulation, with only a small deviation. In figure 2.15 experimental data of binary mixtures of cyclohexanone with CO_2 from literature [19] is shown. In the binary mixture of cyclohexanone with CO_2 the experimental data trend is followed and underpredicted with the PSRK simulation with only a small and almost constant deviation.
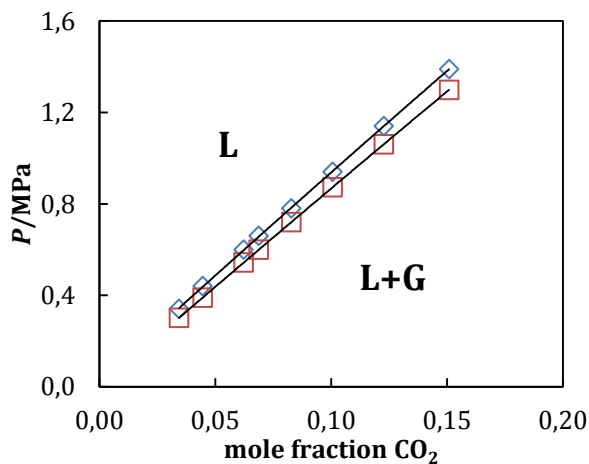
Figure 2.16: *P,x*-diagram acetic acid + CO_2 at T=298.15 K (Appendix G.16). Description of symbols used: (blue ◇) experimental data [21], (red □) PSRK simulation.
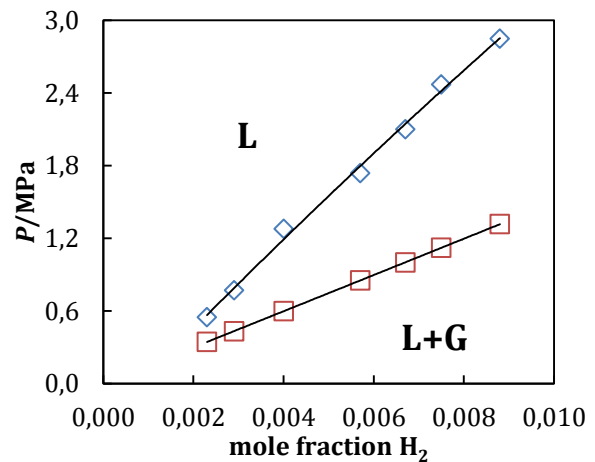
Figure 2.17: *P,x*-diagram acetic acid + H_2 at T=298.15 K (Appendix G.17). Description of symbols used: (blue ◇) experimental data [21], (red □) PSRK simulation.

In figure 2.16 and 2.17 experimental and simulation data of binary mixtures of acetic acid with CO_2 and H_2 from literature [21] is shown. In the binary mixture of acetic acid with CO_2 the experimental data trend is followed with constant deviation and underpredicted with the PSRK simulation. The deviation in the binary mixture of acetic acid with H_2 from the experimental data with the PSRK is underpredicted and increases very rapidly when the mole fraction H_2 increases. Binary mixtures of acetic acid with H_2 are inaccurately predicted with the PSRK EOS.
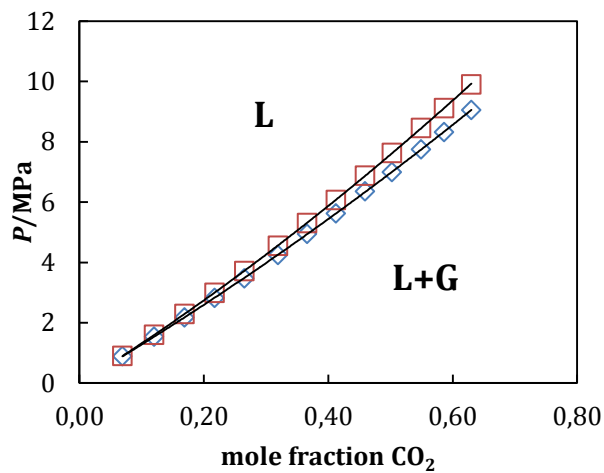
Figure 2.18: *P,x*-diagram decane + CO_2 at T=344.3 K (Appendix G.18). Description of symbols used: (blue ◇) experimental data [23], (red □) PSRK simulation.
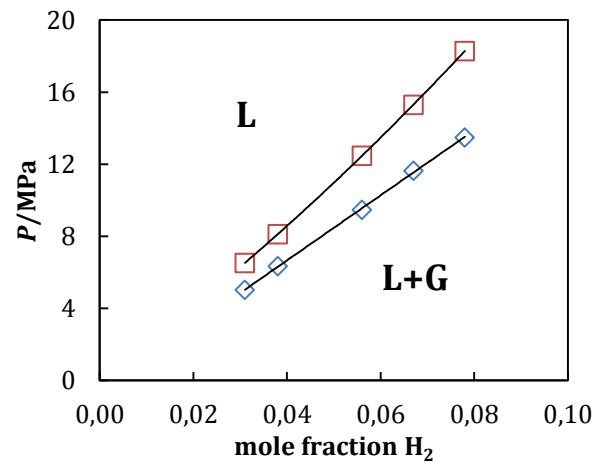
Figure 2.19: *P,x*-diagram decane + H_2 at T=283.22 K (Appendix G.19). Description of symbols used: (blue ◇) experimental data [24], (red □) PSRK simulation.

In figure 2.18 and 2.19 experimental data of binary mixtures of decane respectively with CO_2 and H_2 from literature [23] [24] is shown. In the binary mixture of decane with CO_2 the experimental data trend is followed but with increasing deviation (at higher mole fraction CO_2) and overpredicted with the PSRK simulation. The deviation in the binary mixture of decane with H_2 from the experimental data with the PSRK increases when the mole fraction H_2 increases. When comparing the bubblepoint line from CO_2 and H_2 in decane it can be observed that H_2 in combination with decane is much higher.

2.2 PSRK EOS modeling trends

Some of the bubblepoint lines are measured at identical temperature, which enables to compare the bubblepoint lines of different structures and thus indicate the order prediction of the PSRK EOS.

(a)   *(b)*
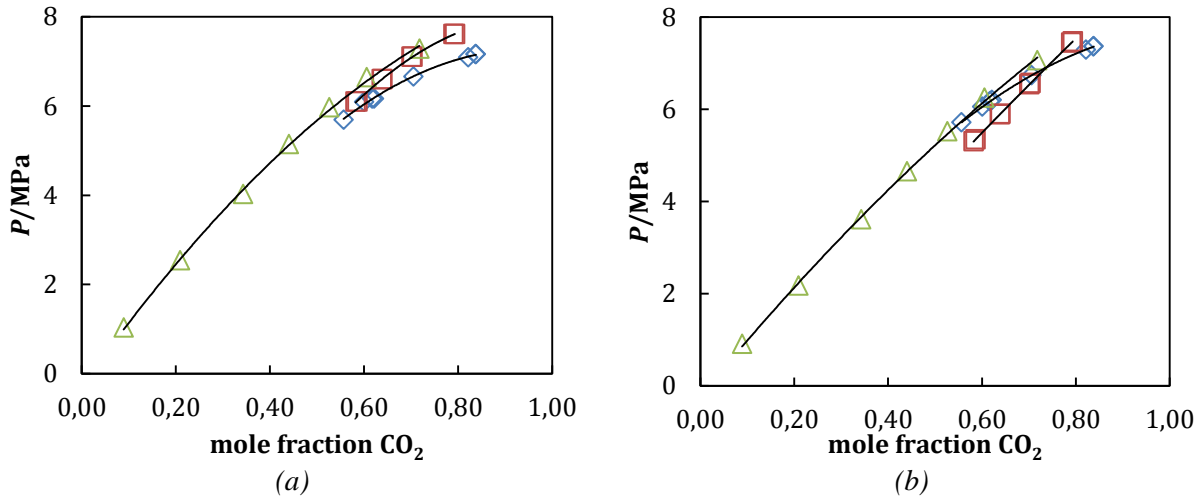
Figure 2.20: *P,x*-diagram of binary mixtures with CO_2 at T=313 K; (a) experimental data, (b) PSRK simulation. Description of symbols used: (blue ◇) ethylbenzene [14], (red ☐) methyl benzoate [20], (green △) propyl cyclohexane[18].

In figure 2.20 two benzene ring based structures and one cyclohexane based structures is plotted. The experimental results show that ethylbenzene has a lower bubblepoint then methyl benzoate when the mole fraction of CO_2 is high (0.6-0.8) and propyl cyclohexane has a higher bubblepoint than ethylbenzene at high mole fraction of CO_2. The PSRK EOS correctly predicts the presence of a point where the bubble point line of methyl and ethyl benzene seem to coincide, but at the wrong concentration. Furthermore, the order of methyl benzoate and propyl cyclohexane is predicted correctly. However, the bubble point pressure of the mixture of methyl benzoate and CO_2 is inaccurate and underpredicted, leading to a deviation in the order of the bubblepoint line. The bubblepoint line for ethylbenzene is accurate predicted for low CO_2 concentration (<0.70 mole fraction CO_2), the bubblepoint line for methyl benzoate is predicted more accurate for higher CO_2 concentrations (>0.7 mole fraction CO_2). Ethylbenzene with CO_2 is overpredicted while methyl benzoate and propyl cyclohexane is underpredicted. Trends and bubblepoint order of the PSRK EOS is not identical to the experimental values.
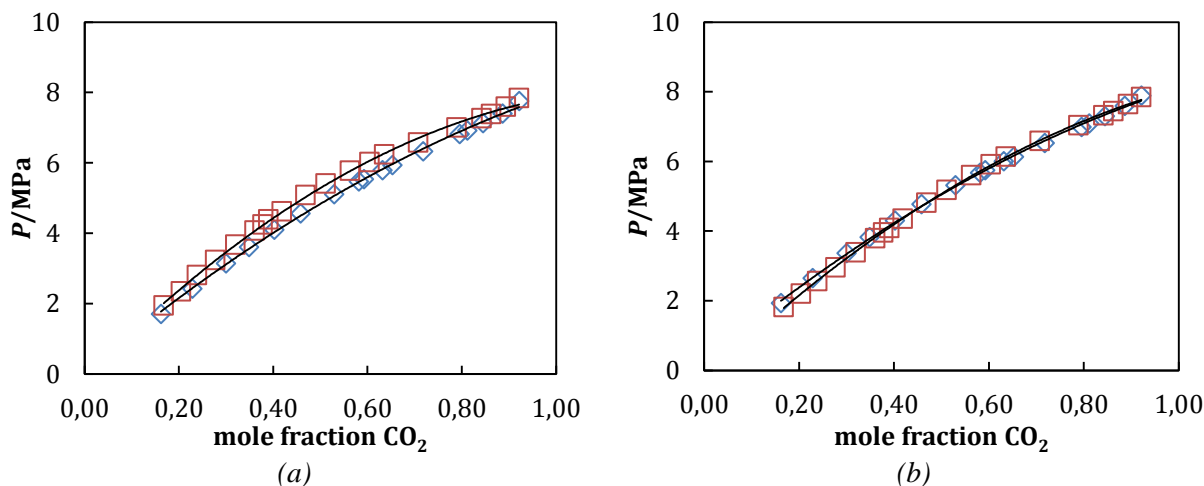
Figure 2.21: *P,x*-diagram of binary mixtures with CO_2 at T=315 K; (a) experimental data, (b) PSRK simulation. Description of symbols used: (blue ◇) benzene [15], (red □) cyclohexane [15].

Benzene has a lower bubblepoint compared to cyclohexane in combination with CO_2 (figure 2.21), this trend can be also observed in figure 2.20. Both benzene and cyclohexane are well predicted with the PSRK EOS, however benzene with CO_2 is overpredicted with the PSRK EOS and cyclohexane with CO_2 is underpredicted with the PSRK EOS.
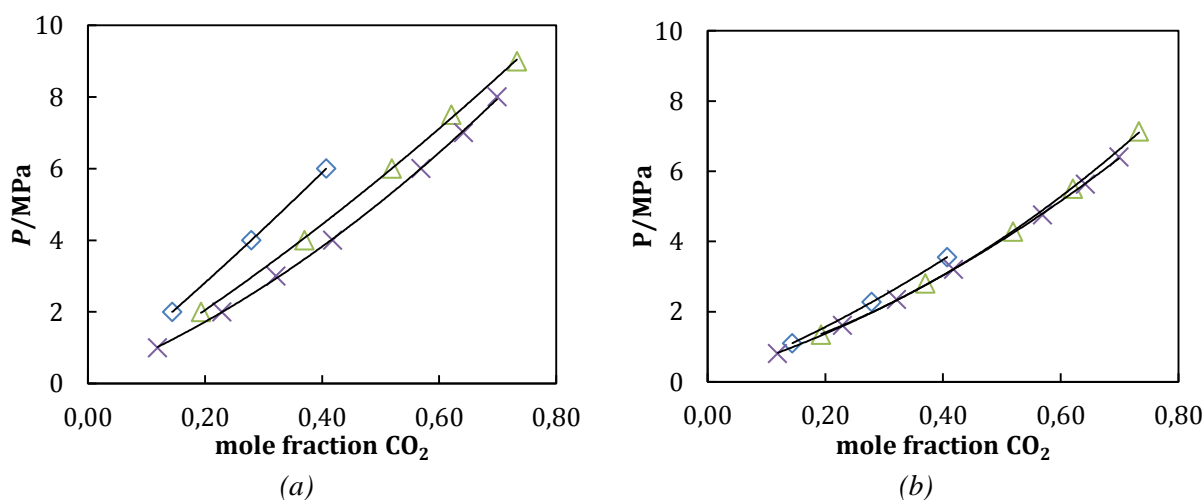
Figure 2.22: *P,x*-diagram of binary mixtures with CO_2 at T=333 K; (a) experimental data, (b) PSRK simulation. Description of symbols used: (blue ◇) phenyl acetate[17], (green △) cyclohexyl acetate [17], (purple ✕) hexyl acetate [17].

In figure 2.22 phenyl acetate, cyclohexyl acetate and hexyl acetate is plotted. Hexyl acetate has the lowest bubblepoint while the highest bubblepoint is given by the phenyl acetate. In this case the cyclohexyl acetate has a lower bubblepoint than the phenyl acetate, which is in contrast with figure 2.20 and 2.21. Phenyl acetate, cyclohexyl acetate and hexyl acetate are all three underpredicted with the PSRK EOS. The experimental trends and bubblepoint order are followed with PSRK EOS.
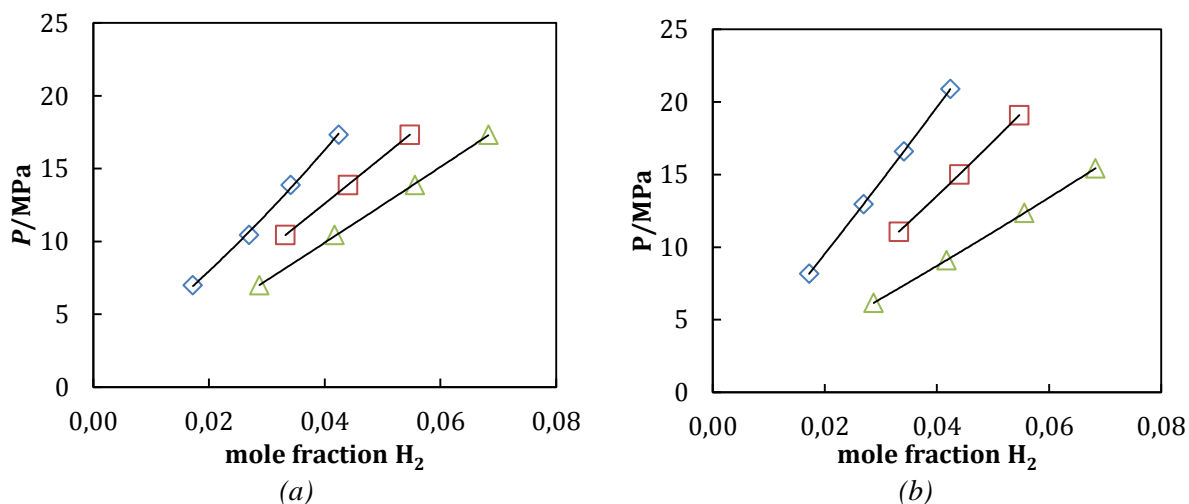
Figure 2.23: *P,x*-diagram of binary mixtures with H_2 at T=295 K; (a) experimental data, (b) PSRK simulation. Description of symbols used: (blue ◇) benzene [22], (red □) ethylbenzene [22], (green △) cyclohexane [22].

In figure 2.23 the highest bubblepoint is given with benzene, the lowest with cyclohexane. This is in contrast with figure 2.20 and 2.21 but similar as the results found in figure 2.22. Benzene and ethylbenzene are, in contrast to cyclohexane with CO_2, overpredicted with the PSRK EOS. The experimental trends and bubblepoint order are followed with PSRK EOS. The overview of accuracies achieved with PSRK EOS to simulate the bubblepoint curve of the literature data is shown in table 2.2.

Table 2.2: Validation PSRK EOS with literature experimental data range

Chemical	Absolute pressure difference		Absolute deviation from exp.	
	CO_2 [MPa]	H_2 [MPa]	CO_2 [%]	H_2 [%]
Benzene[1]	0.14-0.22	1.18-3.55	1.8-13.0	16.9-20.5
Ethylbenzene[1]	0.04-0.21	0.62-1.76	0.6-2.9	6.0-10.2
Methyl benzoate[1]	0.14-0.75	-	1.8-13.1	-
Phenyl acetate[1]	0.90-2.45	-	40.8-45.1	-
Biphenyl[1]	1.36-7.10	-	13.1-19.0	-
Cyclohexane[2]	0.05-0.28	0.83-1.90	0.7-8.9	11.0-12.8
Cyclohexanone[2]	0.11-0.21	-	1.3-9.9	-
Propyl cyclohexane[2]	0.12-0.49	-	3.0-11.9	-
Cyclohexyl acetate[2]	0.65-2.00	-	20.8-32.7	-
Acetonitrile[3]	0.01-0.27	-	0.5-11.8	-
Acetic acid[3]	0.06-0.09	0.21-1.53	6.6-11.5	37.4-54.6
Decane[3]	0.01-0.85	1.50-4.80	1.5-9.6	29.8-35.6
Hexyl acetate[3]	0.20-1.60	-	19.5-21.7	-
Ethanol[3]	0.002-0.29	-	0.04-15.9	-

[1]benzene based structure.

[2]cyclohexane based structure.

[3]hydrocarbon chain based structure.

The structures in table 2.2 show that there is a large difference in the prediction of the bubblepoint curve with the PSRK EOS.

2.3 Conclusion PSRK EOS literature data and modeling

Literature VLE data is used to validate the use of the PSRK EOS for identifying promising molecular structures for pre-combustion CO_2 capture. Most important for this capture process are structures having high CO_2 and low H_2 solubility.

Based on the results of the predicted *P,x*-diagrams at constant temperature, it can be concluded that VLE of small molecular structures with CO_2 are most accurately predicted. An explanation is that small molecules consist of a lower number of UNIFAC groups, leading to a higher accuracy. Structures like benzene, ethylbenzene cyclohexane and cyclohexanone are simulated within 10% deviation over the whole mole fraction range of CO_2. Especially cyclohexane and benzene are accurately predicted. However, biphenyl is overpredicted at low mole fractions of CO_2 and underpredicted at high mole fractions (above 0.60 mole fraction) of CO_2. Hydrocarbon chain structures acetonitrile, acetic acid and decane are simulated within 10% deviation over the whole mole fraction range of CO_2. Largest deviations were found for mixtures containing H_2 or an acetate structure with CO_2. However, when looking at the order prediction of the mixtures containing H_2, the order seems to be correct. In this case, we should use the PSRK EOS for hydrogen as a qualitative prediction tool. Furthermore, in general one can conclude that benzene based structures are more likely to be overpredicted while cyclohexane or hydrocarbon chain based structures are more likely to be underpredicted.

The experimental VLE from literature is used to indicate solubility of CO_2 and H_2. In the literature some VLE order trends are found: binary mixtures of benzene based structures (benzene, methyl benzoate and ethylbenzene) with CO_2 have a lower bubblepoint than mixtures of cyclohexane based structures (cyclohexane, propyl cyclohexane) with CO_2. The solubility order is changed with an additional acetate group: binary mixtures of phenyl acetate and CO_2 have a higher bubblepoint line than mixtures of cyclohexyl acetate and hexyl acetate with CO_2. Binary mixtures of benzene with a small mole fraction of H_2 have a higher bubblepoint pressure than mixtures of cyclohexane with H_2, in contract to those of with CO_2. Mixtures of ethylbenzene with low concentration of H_2 have a lower bubblepoint than mixtures of benzene with H_2.
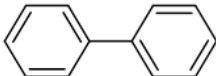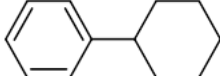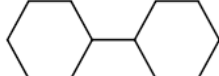
3.0 Modeling of binary systems in Aspen

To predict the most promising LC molecular structure for CO_2 capture Aspen is used to simulate the bubblepoint line of LC structures. Phase transition temperature of basic double ring LCs is in between 298-398 K [12], therefore solubility is indicated in this temperature range. To validate the solubility of CO_2 or H_2 in the LC, a dilute mixture (1 mole % CO_2 or H_2) is used to be able to make use of Henry's law. The research was focused on the influence of polarity with additional chemical groups on the solubility of CO_2 and H_2. From the selectivity analysis the most promising LC structures can be predicted.

3.1 Structure of Liquid crystals

The general molecular structure of LC consists of a double ring structure and an additional chemical group consisting of hydrocarbon chains and including ether, alcohol ester or aldehyde groups [12]. UNIFAC group numbers are identified in Aspen Plus using their individual contribution to the bubblepoint curve. The basic building blocks of LCs are ring structures, therefore the base model consists of double ring structures (A) (table 3.1). Additional group contribution is verified with additional structures (B) (table 3.1). The individual group contribution numbers and structures can be found in Appendix F (table F.1).

Table 3.1: Molecular structure building blocks

Group	Structure					
A	*1.*		*2.*		*3.*	
B	CH_x	OH	CH_xCO	CHO	CH_xCOO	HCOO
	1.	*2.*	*3.*	*4.*	*5.*	*6.*
	CH_xO	CH_xCN	COOH			
	7.	*8.*	*9.*			

Most common molecular structures found in LCs are ring based; biphenyl (A1), cyclohexylbenzene (A2) and bicyclohexyl (A3) [12]. Using the group method (A,B) at least nineteen different LC structures will be modelled to verify and predict their solubility of CO_2 and H_2. The outcome of the selectivity analysis indicates a possible structure for CO_2 capture from syngas.

3.2 Syngas CO_2 capture

An indication of the solubility of CO_2 and H_2 in different LC structures is made with the bubblepoint line simulation in Aspen. From the bubblepoint pressure and temperature, in combination with the calculated fugacity the Henry coefficients can be calculated. The ratio in solubility between H_2 and CO_2 is determining the selectivity; from this an analysis of all structures can be made.

3.2.1 Liquid crystals + CO_2

First only the ring based structures (A) are modelled with CO_2, this is shown in figure 3.1. In figures 3.2 to 3.4 different additional structures (B) are attached to the ring structures. High solubility (e.g. low Henry coefficients) of CO_2 is preferred. In figure 3.1 the solubility order remains the same over the whole temperature range. In the simulation bicyclohexyl has the highest solubility of CO_2 and biphenyl the lowest.
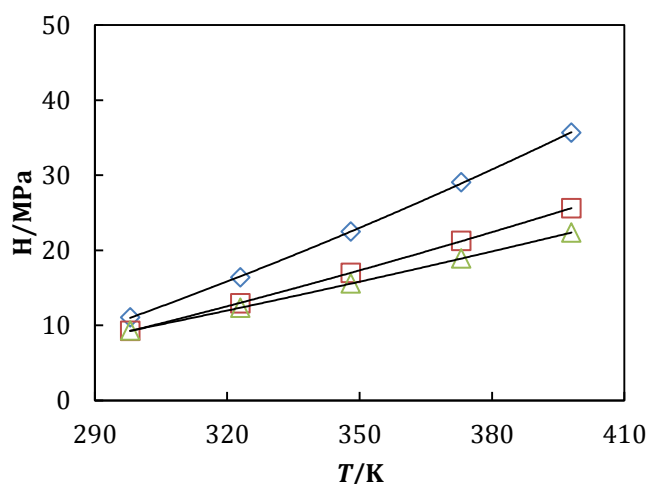
Figure 3.1: Henry coefficients (H) as function of temperature (*T*) of double ring based structures (A) and 1 mole % CO_2 (Appendix E.1). Description of symbols used: (blue ◇) biphenyl (A1), (red ☐) cyclohexylbenzene (A2), (green △) bicyclohexyl (A3).

In figures 3.2a-b the structure includes an alcohol group, in figure 3.3a-d additional functional groups are similar to those in the experimental LCs used. The figures 3.4a-d uses respectively a ketone, aldehyde, ester and formate group next to the ring structures to examine the influence of polarity on the solubility of CO_2.
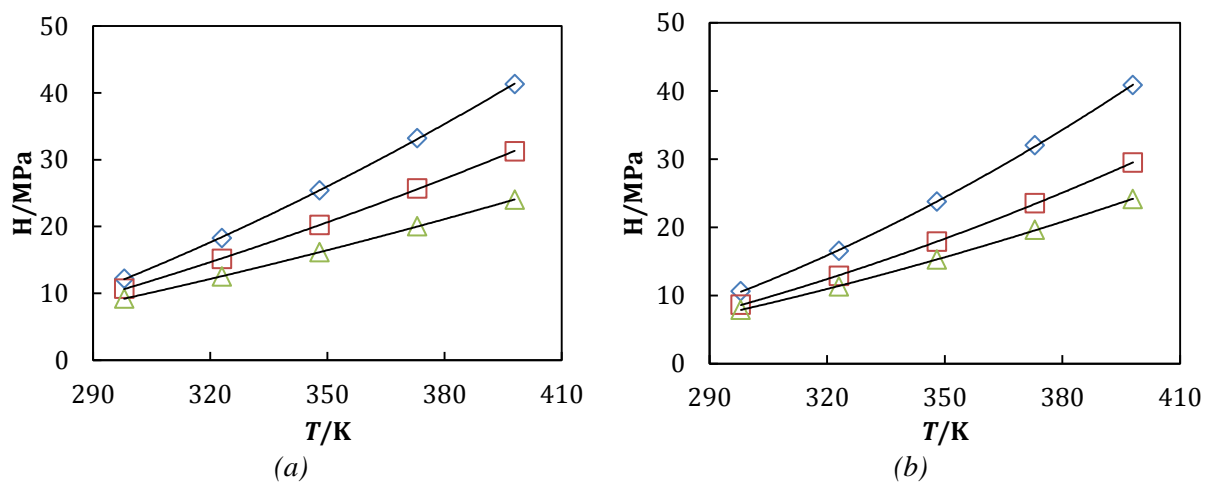
Figure 3.2: Henry coefficients (H) as function of temperature (*T*) of double ring based structures (A) with additional structures and 1 mole % CO_2: (a) alcohol-group (B2, Appendix E.4) and (b) carboxylic acid-group (B9, Appendix E.11).Description of symbols used: (blue ◇) biphenyl-based, (red □) cyclohexylbenzene-based, (green △) bicyclohexyl-based.

In this comparison an alcohol group (figure 3.2a) is added and a carboxyl group (figure 3.2b) is added to the ring structure. The alcohol group has a lower solubility than the double ring structures.
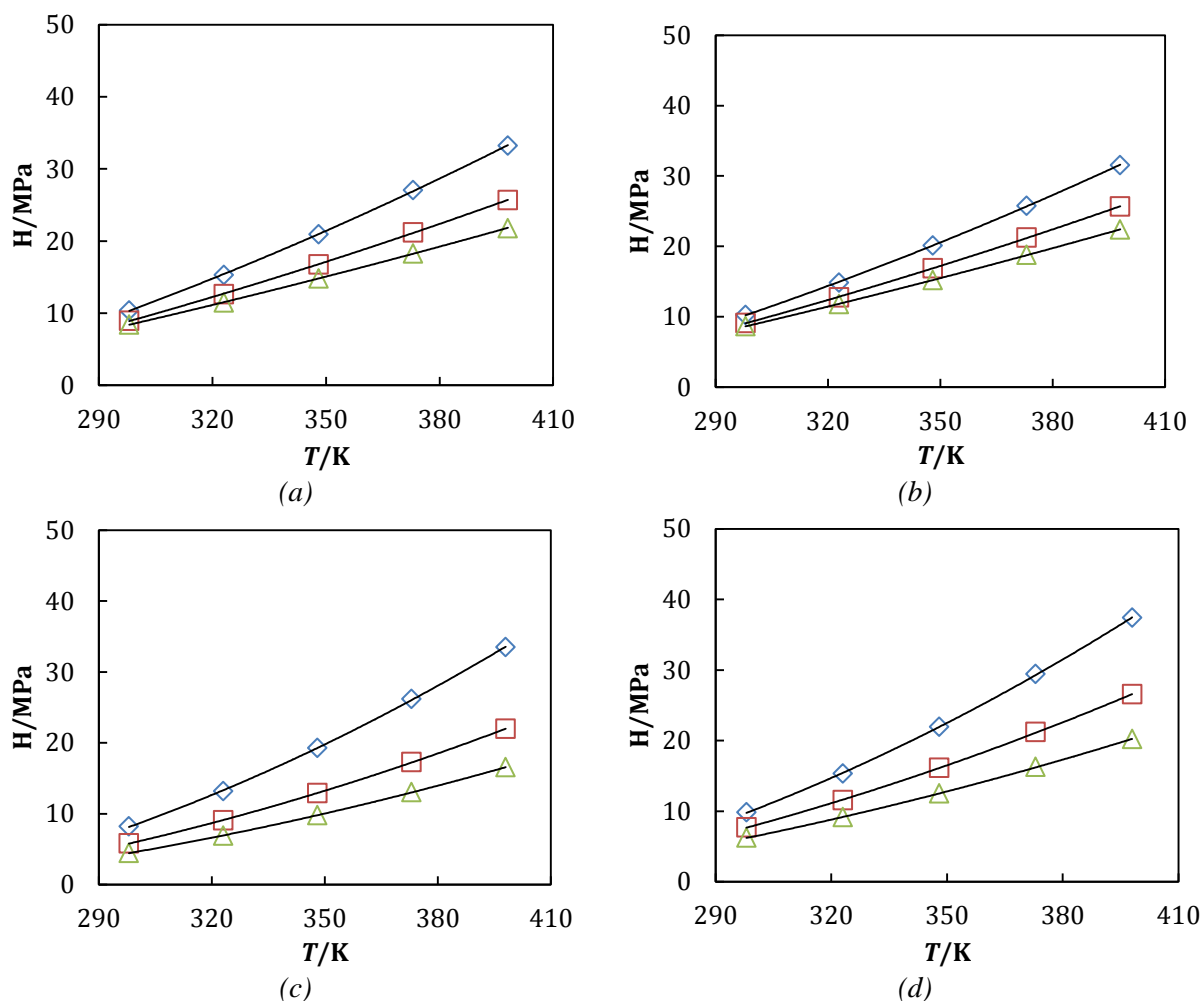
Figure 3.3: Henry coefficients (H) as function of temperature (T) of double ring based structures (A) with additional structures and 1 mole % CO_2: (a) saturated hydrocarbon chain ($C_n = 2$) (B1, Appendix E.2), (b) saturated hydrocarbon chain ($C_n = 5$) (B1, Appendix E.3), (c) ether-group (B7, Appendix E.9) and (d) cyano-group (B8, Appendix E.10). Description of symbols used: (blue ◇) biphenyl-based, (red □) cyclohexylbenzene-based, (green △) bicyclohexyl-based.

With a hydrocarbon chain ($C_n = 2$) (figure 3.3a) the solubility of the ring structures increases, but when the chain is increased ($C_n = 5$) (figure 3.3b) only the biphenyl based (A1B1, $C_n = 5$) increases in solubility while the other two decrease in CO_2 solubility. Ring structures including an ether group (figure 3.3c) increase the solubility of CO_2. Solubility of CO_2 in biphenyl and cyclohexylbenzene ring structures, including a cyano group (figure 3.3d), increases for low temperatures (<380 K). For the bicyclohexyl structures including a cyano group the solubility of CO_2 increases over the whole temperature range.

Figure 3.4: Henry coefficients (H) as function of temperature (*T*) of double ring based structures (A) with additional structures and 1 mole % CO_2: (a) ketone group (B3, Appendix E.5), (b) aldehyde group (B4, Appendix E.6), (c) ester group (B5, Appendix E.7) and (d) formate group (B6, Appendix E.8). Description of symbols used: (blue ◇) biphenyl-based, (red □) cyclohexylbenzene-based, (green △) bicyclohexyl-based.

In this comparison some carbonyl groups are added to the double ring structures, such as a ketone group (figure 3.4a), an aldehyde group (figure 3.4b), an ester group (figure 3.4c) and finally a formate group (figure 3.4d). With the additional ketone group (a) and ester group (c) the bubblepoint curvature is less than with the aldehyde (b) and formate (d) group, this indicates that also at high temperatures the solubility of CO_2 is high. The more polar structure, due to the missing CH_3 group, of the aldehyde (b) and formate (d) group thus decreases the solubility of CO_2. Most striking results are the decrease of CO_2 solubility when an alcohol group is added, largest increase in CO_2 solubility is achieved with an additional ketone, ester and ether group.

3.2.2 Liquid crystals + H_2

First only the ring based structures (A) are modelled with H_2, this is shown in figure 3.5. In figures 3.6 to 3.8 different additional structures (B) are attached to the ring structures. Low solubility (e.g. high Henry coefficients) of the H_2 is preferred. In figure 3.5 the solubility order remains the same over the whole temperature range. In the simulation the bicyclohexyl has the highest solubility of H_2 and biphenyl the lowest.
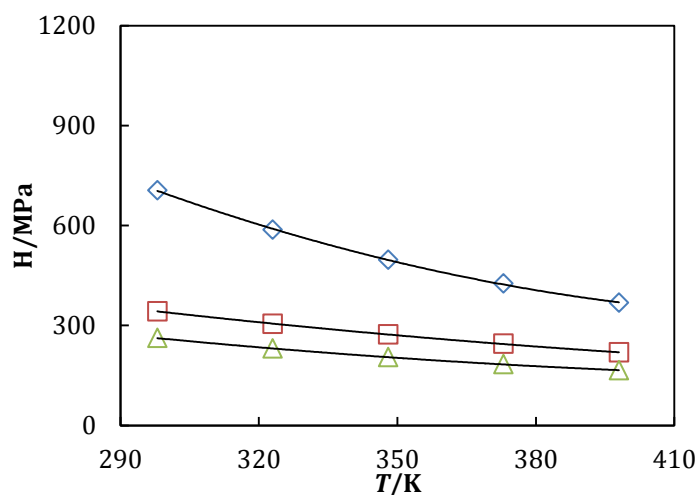
Figure 3.5: Henry coefficients (H) as function of temperature (T) of double ring based structures (A) and 1 mole % H_2 (Appendix E.12). Description of symbols used: (blue ◇) biphenyl (A1), (red □) cyclohexylbenzene (A2), (green △) bicyclohexyl (A3).

When comparing the additional functional groups it will be referred to the double ring structures. In figures 3.6a-b the structure includes an alcohol group, in figure 3.7a-d additional functional groups are similar to those in the experimental LCs used. The figures 3.8a-d uses respectively a ketone, aldehyde, ester and formate group next to the ring structures to examine the influence of polarity on the solubility of H_2.
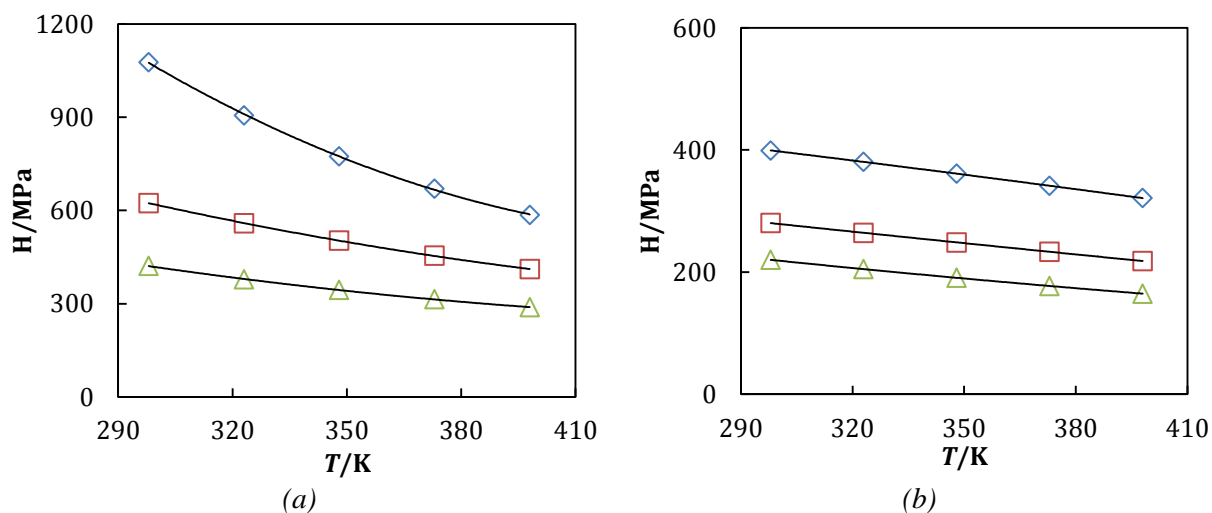
Figure 3.6: Henry coefficients (H) as function of temperature (*T*) of double ring based structures (A) with additional structures and 1 mole % H_2: (a) alcohol group (B2, Appendix E.15) and (b) carboxylic acid group (B9, Appendix E.22).Description of symbols used: (blue ◇) biphenyl-based, (red □) cyclohexylbenzene-based, (green △) bicyclohexyl-based.

In this comparison an alcohol group (figure 3.6a) is added and a carboxyl group (figure 3.6b) is added to the ring structure. The alcohol group decreases H_2 solubility compared to the double ring structure, while carboxyl group increases solubility of H_2.
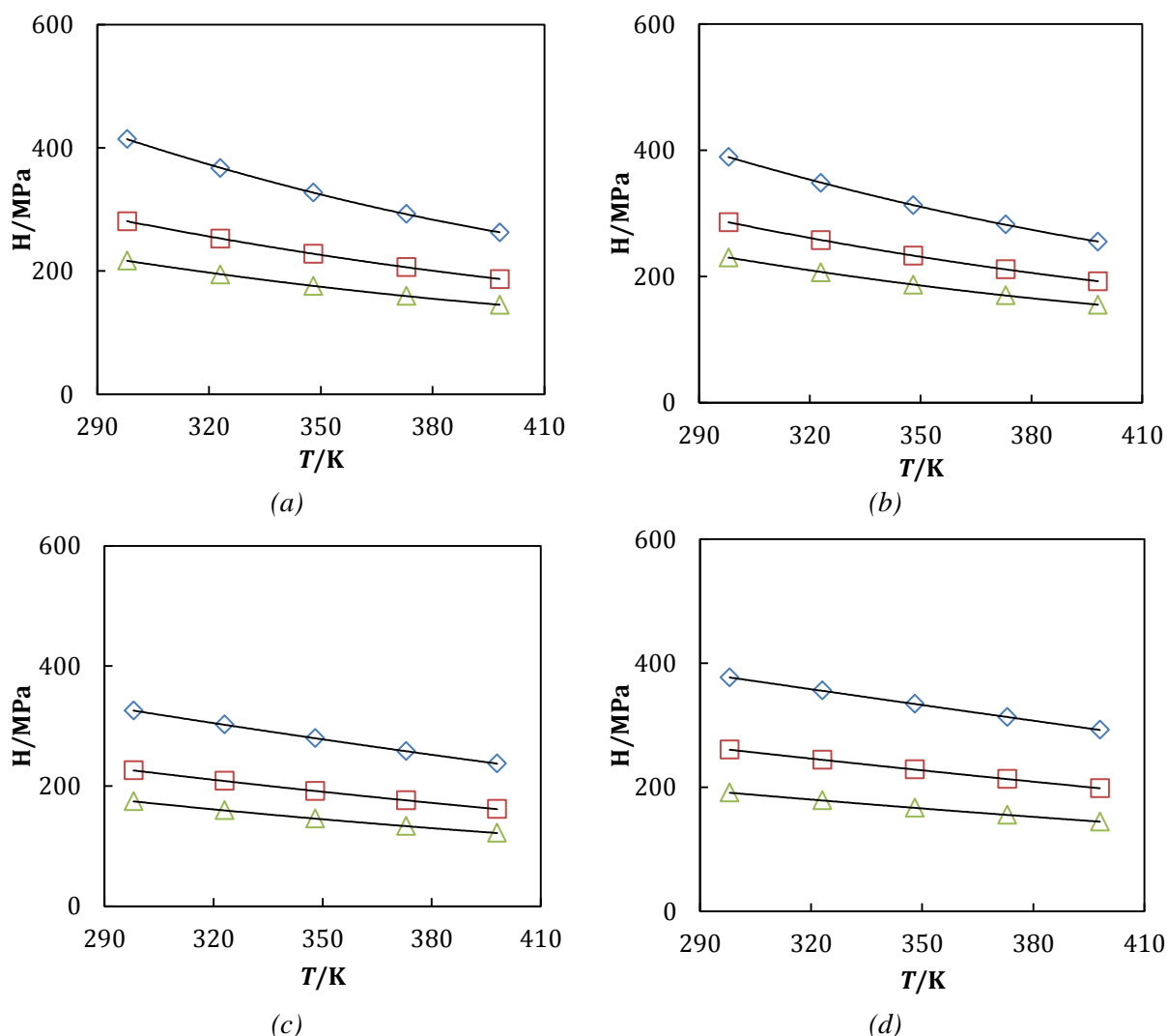
Figure 3.7: Henry coefficients (H) as function of temperature (T) of double ring based structures (A) with additional structures and 1 mole % H_2: (a) saturated hydrocarbon chain ($C_n = 2$) (B1, Appendix E.13), (b) saturated hydrocarbon chain ($C_n = 5$) (B1, Appendix E.14), (c) ether group (B7, Appendix E.20) and (d) cyano group (B8, Appendix E.21). Description of symbols used: (blue ◇) biphenyl-based, (red □) cyclohexylbenzene-based, (green △) bicyclohexyl-based.

With a hydrocarbon chain ($C_n = 2$) (figure 3.7a) the solubility of the ring structures increases, but when the chain is increased ($C_n = 5$) (figure 3.7b) only the biphenyl based increases in solubility while the other two decrease in H_2 solubility. Ring structures including an ether group (figure 3.7c) and a cyano group (figure 3.7d) increase the solubility of H_2.
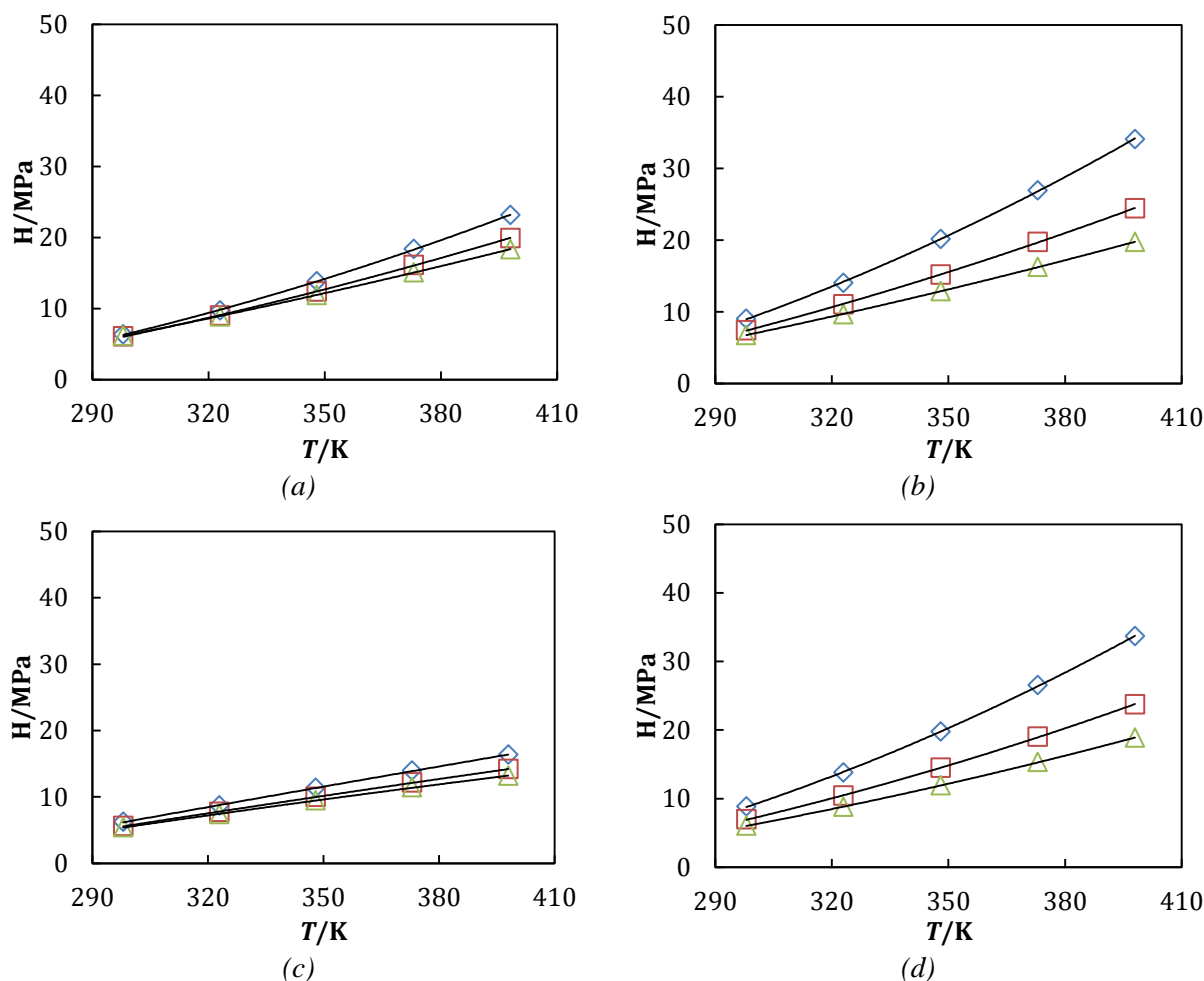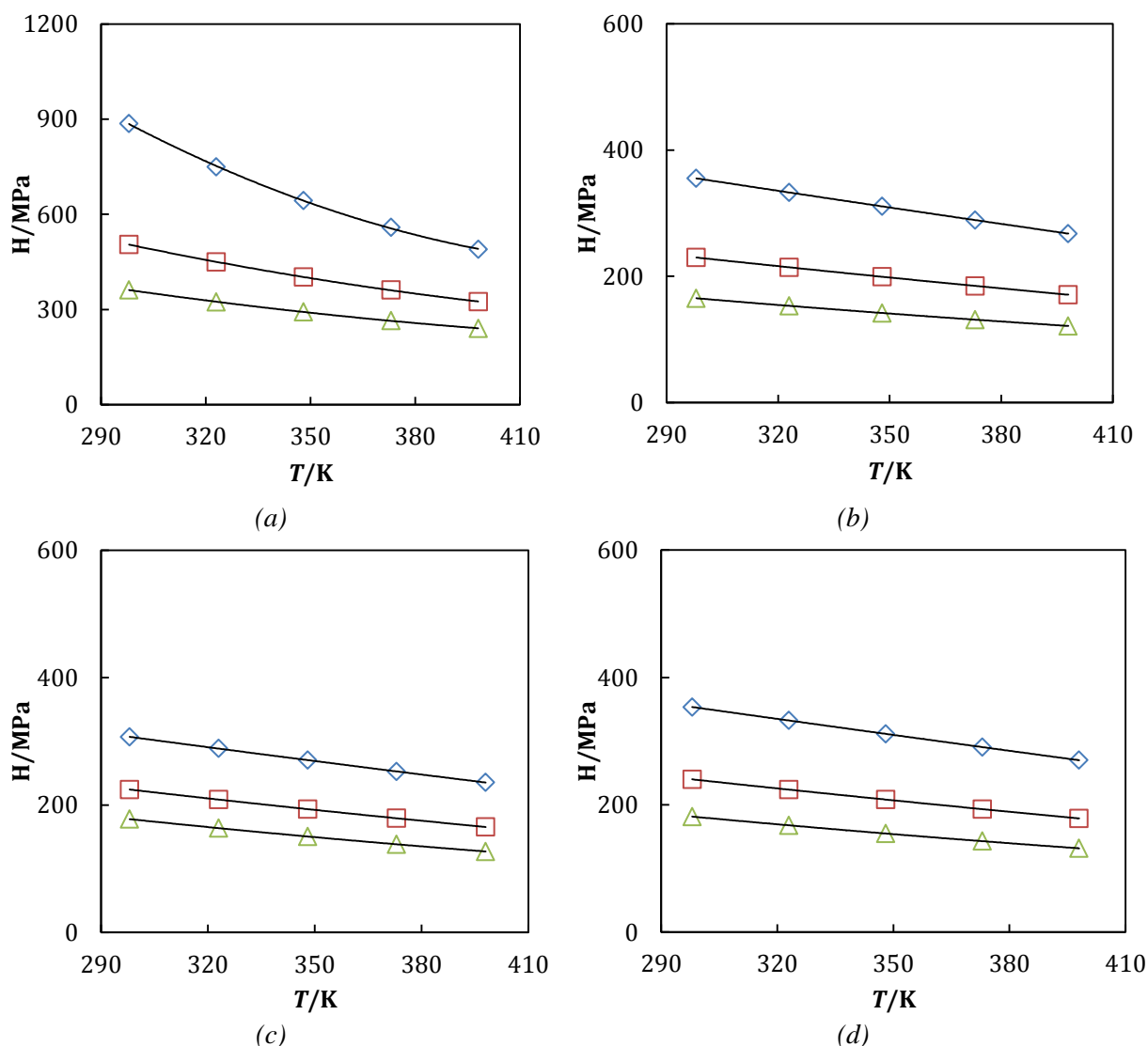
Figure 3.8: Henry coefficients (H) as function of temperature (T) of double ring based structures (A) with additional structures and 1 mole % H_2: (a) ketone group (B3, Appendix E.16), (b) aldehyde group (B4, Appendix E.17), (c) ester group (B5, Appendix E.18) and (d) formate group (B6, Appendix E.19). Description of symbols used: (blue ◇) biphenyl-based, (red □) cyclohexylbenzene-based, (green △) bicyclohexyl-based.

In this comparison some carbonyl groups are added to the double ring structures, such as a ketone group (figure 3.8a), an aldehyde group (figure 3.8b), an ester group (figure 3.8c) and finally a formate group (figure 3.8d). In all the additional functional groups the solubility of H_2 increases concerning the double ring based structures, lowest solubility of H_2 is attained with a ketone group. Most striking results are the decrease of H_2 solubility when an alcohol or ketone group is added, largest increase in H_2 solubility is achieved with an additional ester and ether group.

3.3 Selectivity analysis

To select the most suitable LC structure a selectivity analysis is performed. The Henry coefficients (table 3.2) are used to determine the ideal selectivity (α) predicting the solubility of both gases in the LC. Preferable is high selectivity [eq. 3.1]. The ideal selectivity is more accurate at 298 K.

$$\alpha_{H_2/CO_2} = \frac{H_{H_2}}{H_{CO_2}} \qquad\qquad 3.1$$

Table 3.2: Henry coefficients and ideal selectivity at $T = 298\ K$.

Structure name	H_{CO_2}/MPa	H_{H_2}/MPa	α_{H_2/CO_2}
Biphenyl	11.1	705.9	63.76
Cyclohexylbenzene	9.3	342.6	36.98
Bicyclohexyl	9.3	262.2	28.22
1,1'-Biphenyl, 4-ethyl-	10.4	414.2	39.94
Benzene, (4-ethylcyclohexyl)-	8.9	281.0	31.48
1,1'-Bicyclohexyl, 4-ethyl-	8.4	216.8	25.78
1,1'-Biphenyl, 4-pentyl-	10.3	389.4	37.92
Benzene, (4-pentylcyclohexyl)-	9.1	286.0	31.40
1,1'-Bicyclohexyl, 4-pentyl-	8.7	230.2	26.58
[1,1'-Biphenyl]-4-ol	12.2	1077.2	88.33
Cyclohexanol, 4-phenyl-	10.7	624.1	58.36
[1,1'-Bicyclohexyl]-4-ol	9.2	421.2	45.59
Ethanone, 1-[1,1'-biphenyl]-4-yl-	*6.4*	*886.5*	*139.23*
Ethanone, 1-(4-phenylcyclohexyl)-	*6.1*	*505.1*	*82.98*
Ethanone, 1-[1,1'-bicyclohexyl]-4-yl-	*6.2*	*361.8*	*58.28*
[1,1'-Biphenyl]-4-carboxaldehyde	9.0	355.1	39.31
Cyclohexanecarboxaldehyde, 4-phenyl-	7.4	229.9	30.93
[1,1'-Bicyclohexyl]-4-carboxaldehyde	6.8	165.3	24.35
[1,1'-Biphenyl]-4-ol, 4-acetate	*6.2*	*307.0*	*49.33*
Cyclohexanol, 4-phenyl-, 1-acetate	*5.6*	*224.3*	*40.05*
[1,1'-Bicyclohexyl]-4-ol, 4-acetate	5.4	177.9	32.84
[1,1'-Biphenyl]-4-ol, 4-formate	8.8	353.5	39.99
Cyclohexanol, 4-phenyl-, 1-formate	7.0	240.0	34.49
[1,1'-Bicyclohexyl]-4-ol, 4-formate	6.1	181.6	29.98
1,1'-Biphenyl, 4-methoxy-	8.2	325.6	39.66
Benzene, (4-methoxycyclohexyl)-	*5.8*	*226.1*	*38.77*
1,1'-Bicyclohexyl, 4-methoxy-	*4.5*	*174.6*	*38.99*
[1,1'-Biphenyl]-4-acetonitrile	9.8	377.1	38.37
Cyclohexaneacetonitrile, 4-phenyl-	7.7	260.7	33.87
[1,1'-Bicyclohexyl]-4-acetonitrile	6.2	191.4	30.75
[1,1'-Biphenyl]-4-carboxylic acid	10.6	399.2	37.60
Cyclohexanecarboxylic acid, 4-phenyl-	8.6	280.2	32.41
[1,1'-Bicyclohexyl]-4-carboxylic acid	7.9	220.1	27.79

The selectivity analysis is divided into the three ring structures, biphenyl based structures (figure 3.9), cyclohexylbenzene based structures (figure 3.10) and bicyclohexyl based structures (figure 3.11). In this way the influence of the additional group on the solubility and selectivity can be compared for each ring structure.
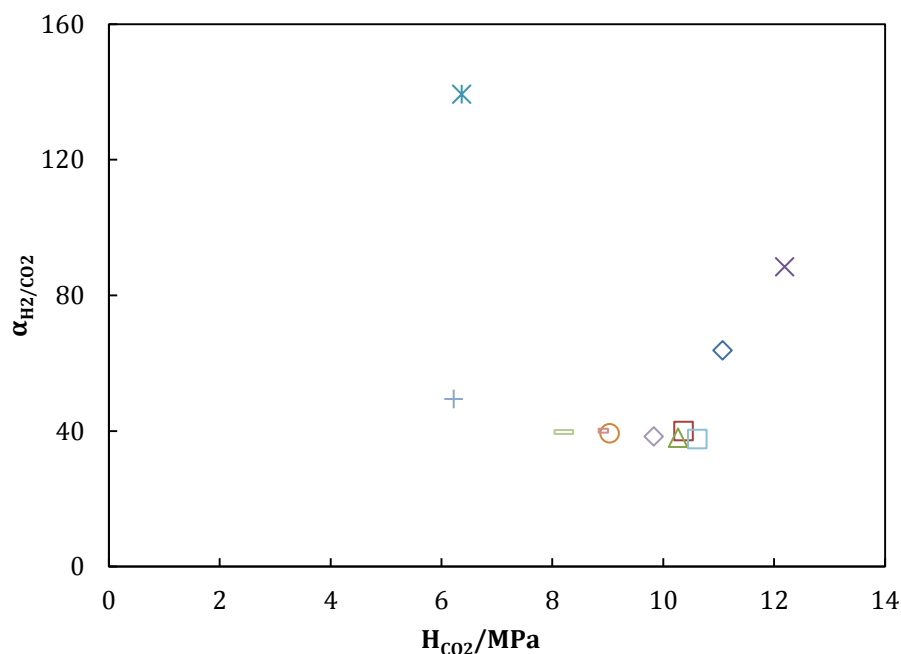
Figure 3.9: Selectivity analysis of biphenyl (A1) based structures as function of Henry coefficients (H) of CO_2. Description of symbols used: (blue ◇) Biphenyl, (red □) 1,1'-Biphenyl, 4-ethyl-, (green △) 1,1'-Biphenyl, 4-pentyl-, (purple ✕) [1,1'-Biphenyl]-4-ol, (light blue ✶) Ethanone, 1-[1,1'-biphenyl]-4-yl-, (orange ◯) [1,1'-Biphenyl]-4-carboxaldehyde, (blue ✛) [1,1'-Biphenyl]-4-ol, 4-acetate, (red ▱) [1,1'-Biphenyl]-4-ol, 4-formate, (light green ▭) 1,1'-Biphenyl, 4-methoxy-, (purple ◇) [1,1'-Biphenyl]-4-acetonitrile, (light blue ☐) [1,1'-Biphenyl]-4-carboxylic acid.

From the groups added to biphenyl the most promising groups are the ketone group [✶] and the ester group [✛]. From all groups added only the alcohol group [✕] decreases the solubility of CO_2. All groups increase solubility of H_2 except the alcohol group [✕] and the ketone group [✶]. Worst performing additional structure is the alcohol group [✕] due to the decrease in solubility of CO_2.
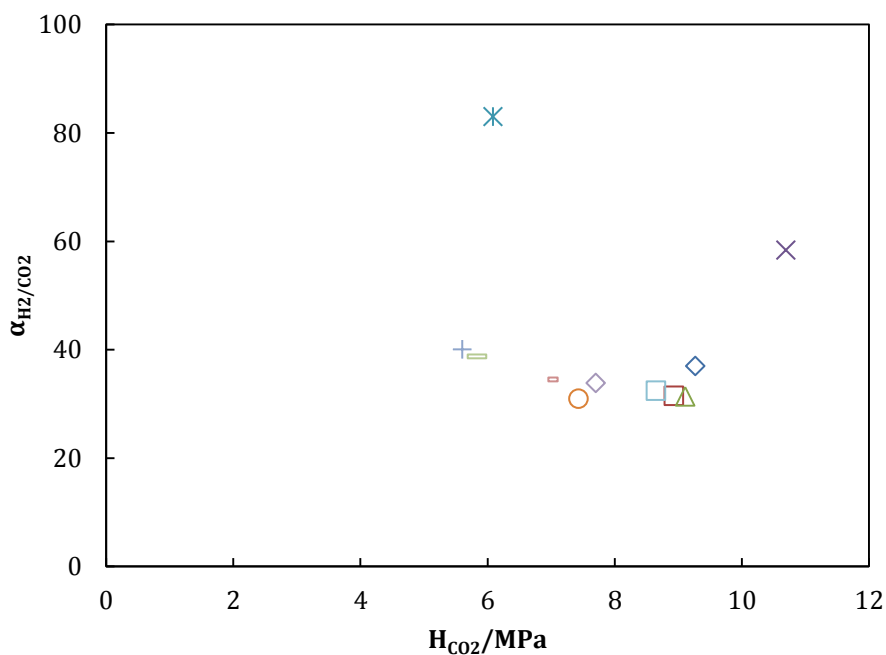
Figure 3.10: Selectivity analysis of cyclohexylbenzene (A2) based structures as function of Henry coefficients (H) of CO_2. Description of symbols used: (blue ◇) Cyclohexylbenzene, (red □) Benzene, (4-ethylcyclohexyl)-, (green △) Benzene, (4-pentylcyclohexyl)-, (purple ✕) Cyclohexanol, 4-phenyl-, (light blue ✳) Ethanone, 1-(4-phenylcyclohexyl)-, (orange ○) Cyclohexanecarboxaldehyde, 4-phenyl-, (blue ✛) Cyclohexanol, 4-phenyl-, 1-acetate, (red ▭) Cyclohexanol, 4-phenyl-, 1-formate, (light green ▬) Benzene, (4-methoxycyclohexyl)-, (purple ◇) Cyclohexane acetonitrile, 4-phenyl-, (light blue ☐) Cyclohexane carboxylic acid, 4-phenyl-.

From the groups added to cyclohexylbenzene the most promising groups are the ketone group [✳], the ester group [✛] and the ether group [▬]. From all groups added only the alcohol group [✕] decreases the solubility of CO_2. The ketone group [✳], the alcohol group [✕], the ester group [✛] and the ether group [▬] all decrease the solubility of H_2. Worst performing additional structure is the alcohol group [✕] due to the decrease in solubility of CO_2.
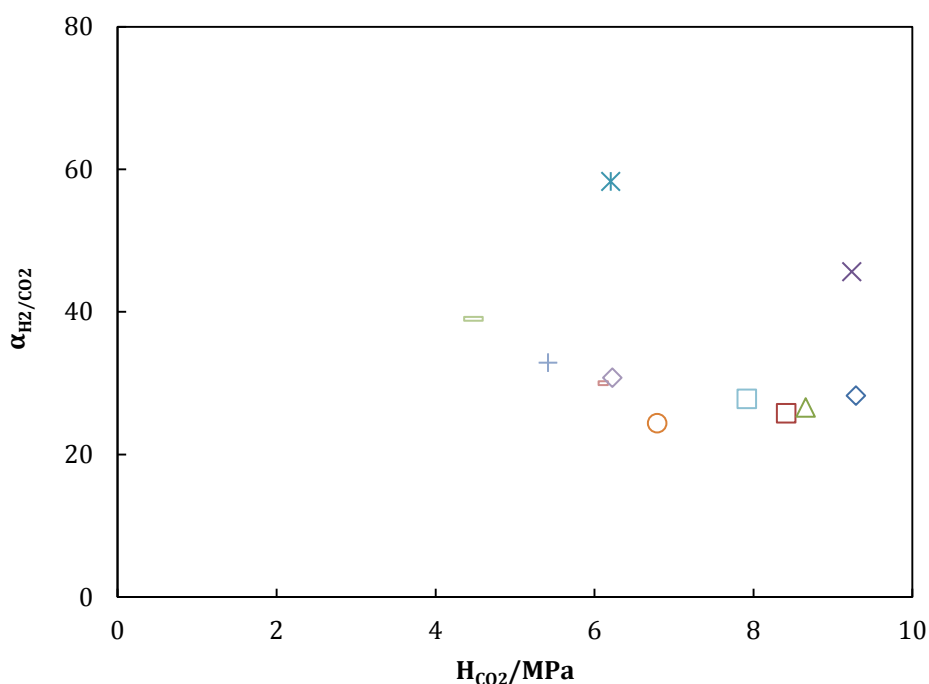
Figure 3.11: Selectivity analysis of bicyclohexyl (A3) based structures as function of Henry coefficients (H) of CO_2. Description of symbols used: (blue ◇) Bicyclohexyl, (red ☐) 1,1'-Bicyclohexyl, 4-ethyl-, (green △) 1,1'-Bicyclohexyl, 4-pentyl-, (purple ✕) [1,1'-Bicyclohexyl]-4-ol, (light blue ✳) Ethanone, 1-[1,1'-bicyclohexyl]-4-yl-, (orange ◯) [1,1'-Bicyclohexyl]-4-carboxaldehyde, (blue ✛) [1,1'-Bicyclohexyl]-4-ol, 4-acetate, (red ▭) [1,1'-Bicyclohexyl]-4-ol, 4-formate, (light green ▬) 1,1'-Bicyclohexyl, 4-methoxy-, (purple ◇) [1,1'-Bicyclohexyl]-4-acetonitrile, (light blue ☐) [1,1'-Bicyclohexyl]-4-carboxylic acid.

From the groups added to bicyclohexyl the most promising groups are the ketone group [✳], the ether group [▬] and the ester group [✛]. From all groups added only the alcohol group [✕] decreases the solubility of CO_2. The groups that increase the increase the solubility of H_2 are; aldehyde group [◯], carboxylic acid group [☐] and the single hydrocarbon chains added [☐,△]. All additional structures increase CO_2 solubility, the increase is solubility if marginal for the alcohol group [✕].

From the three selectivity analysis a selection of the best performing can be made. In all three analyses the ketone group is predicted to perform best while the alcohol group is predicted to perform worst. When Henry coefficients of CO_2 in LC are selected below 8 MPa and the ideal selectivity above 38 MPa we find the following LC structures (figure 3.12).
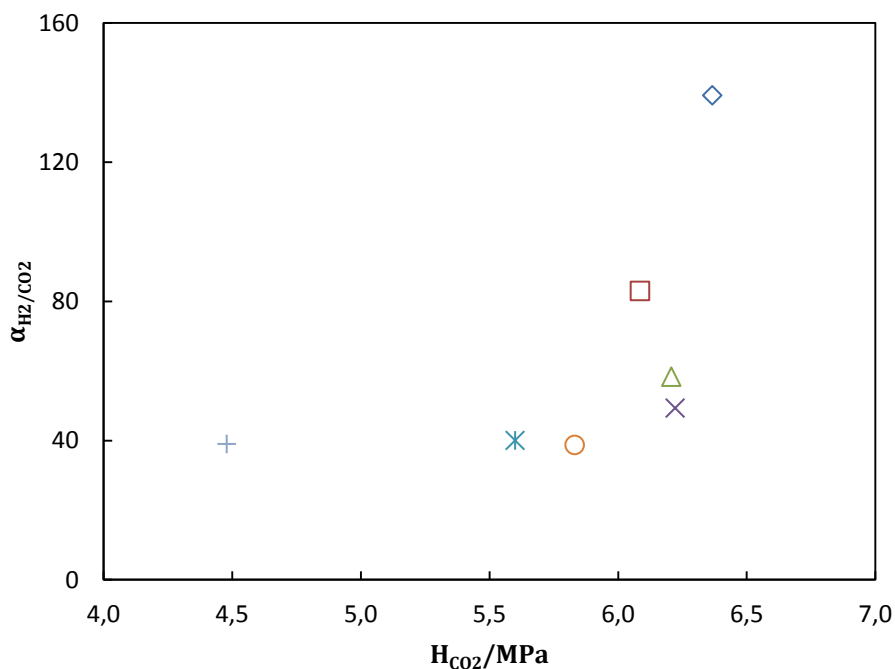
Figure 3.12: Selectivity analysis of structures with $\alpha_{H2/CO2}$>38 MPa and Henry coefficients (H) of CO_2 H<8 MPa. Description of symbols used: (blue ◇) Ethanone, 1-[1,1'-biphenyl]-4-yl-, (red □) Ethanone, 1-(4-phenylcyclohexyl)-, (green △) Ethanone, 1-[1,1'-bicyclohexyl]-4-yl-, (purple ✕) [1,1'-Biphenyl]-4-ol, 4-acetate, (light blue ✳) Cyclohexanol, 4-phenyl-, 1-acetate, (orange ○) Benzene, (4-methoxycyclohexyl)-, (blue ┼) 1,1'-Bicyclohexyl, 4-methoxy-.

From the total selectivity analysis the best performing additional structures for CO_2 capture from syngas are predicted to be the ketone group [◇,□,△], the ether group [○,┼] and the ester group [✕,✳]. The ketone group is predicted to perform well for all three double-ring structures, the ether and ester group only in combination with cyclohexylbenzene and bicyclohexyl.

3.4 Conclusion modeling of binary systems

The simulation of bubblepoint lines in Aspen is used to identify the most promising molecular structure for CO_2 capture from syngas. Simulations of the molecular structures include group (B) contribution to identify the solubility of CO_2 and H_2. These are used for selecting the most suitable LC structure for CO_2 capture. High solubility of CO_2 (e.g. low Henry coefficient) and low solubility of H_2 (e.g. high Henry coefficient) means high selectivity coefficient ($\alpha_{H2/CO2}$) and thus a more favourable structure.

According to the PSRK EOS, binary mixtures of 1 mole % of CO_2 with biphenyl structures have the highest Henry coefficients, followed by the structures with cyclohexylbenzene and bicyclohexyl. . This solubility order is found for all additional groups. The Henry coefficients increase when an alcohol group (OH) is added to the structure. All other simulation structures decrease the Henry coefficients of the mixture. The ketone group (CH_xCO), ester group (CH_xCOO) and ether group (CH_xO) increase the CO_2 solubility. As was found for CO_2, binary mixture of 1 mole % H_2 with biphenyl have the highest Henry coefficients, followed by cyclohexylbenzene and bicyclohexyl. The addition of several side groups did not change the order. Addition of an alcohol group (OH) or ketone group (CH_xCO) caused a decrease in H_2 solubility. The VLE simulated in chapter 2 is found to be more accurate for binary mixtures with CO_2 than those in combination with H_2. For this reason expected is that the accuracy of the bubblepoint curves of binary mixture with CO_2 is higher. As the PSRK EOS uses the UNIFAC parameters which are fitted at 298 K, it is expected that the selectivity analysis will give the most accurate results at this temperature. And, as small molecular structures are found to be more accurate (chapter 2), in the LC modelling also small structures are used to increase accuracy of prediction.

4.0 Experimental results of binary mixtures

4.1 Experimental method

In the Cailletet setup the phase transitions are measured visually; this method is also called the synthetic visual method (SynVis). The filling (isopleth) constrains the phase behaviour to two degrees of freedom, namely pressure and temperature, for the complete filling procedure and corrections made to the measured data, see Appendix A. The Cailletet setup (figure 4.1) holds the Cailletet tube supplying it with variable temperature (thermostatic bath/electric coil heater) and pressure (dead weight gauge); keeping one variable constant one degree of freedom (Gibbs phase rule) is achieved. The experiments are executed on binary systems containing LC and CO_2 ($N = 2$) and at least one phase ($\pi = 1$), therefore the maximum amount of variables is three (namely; pressure (P), temperature (T) and composition (x)). When filling the tube the system becomes an isopleth (i.e. 1 mass % CO_2), at which point the system has only two degrees of freedom (P,T) which are controlled with the laboratory setup. [5] [7]
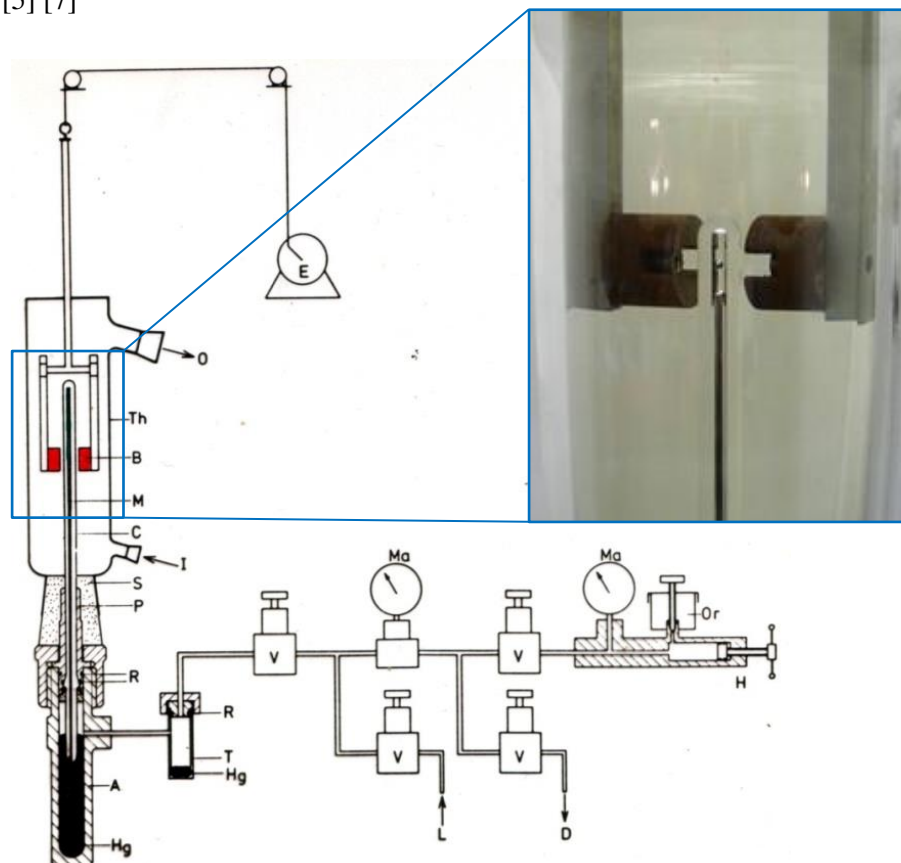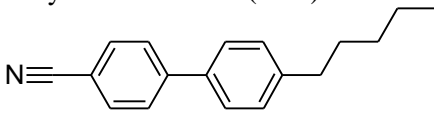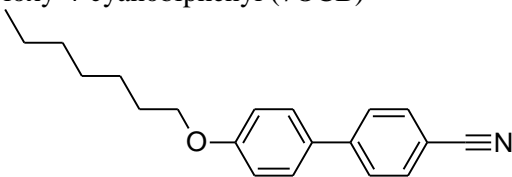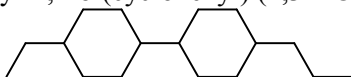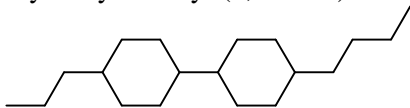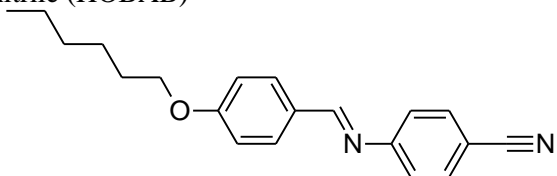
Figure 4.1: Cailletet setup. Description: A autoclave, B button magnets for stirring, C Cailletet tube, D drain, H rotating hand pump, Hg mercury, I thermostat input, O thermostat output, L line to dead weight pressure gauge, M mixture measured, Ma manometers, Or hydraulic oil reservoir, P closing plug, R Viton O-rings, S silicone rubber stopper (or cork), T mercury trap, Th glass thermostat, V valve.

Accuracy reached in the VLE measurement is limited to the equipment used in the laboratory experiments. Controlling the pressure while keeping the temperature constant will give an accuracy of $u(P)=\pm0.005$ MPa, when varying the temperature while keeping the pressure constant the accuracy is $u(T)=\pm0.01$ K (thermostatic bath) or $u(T)=\pm0.1$ K (electric coil heater). Accuracy of the Isotropic to Isotropic + Gas (I→I+G) and of the Condensed to Condensed + Gas (C→C+G) measurements is u(P)=±0.005 MPa. The accuracy of the Isotropic + Gas to Condensed + Gas phase (I+G→C+G) measurements is $u(P)=\pm0.005$ MPa. Accuracies of the phase equilibria lines for Condensed + Isotropic to Isotropic (C+I→I) and Condensed to Condensed + Isotropic (C→C+I) measurements are $u(T)=\pm0.01$ K in a water filled thermostatic bath , and $u(T)=\pm0.1$ K in an oil filled electric coil heater. The gas rack used for filling the Cailletet tube has an accuracy of u(P)=±0.1 mbar which leads to an uncertainty in the composition of $u(x)=\pm0.001$. To verify if the deviation of the measured equilibria points are within the accuracy limit a polynomial curve or linear line is plotted. Deviation from the plotted line or curve can be used to identify if the measured point is within the set accuracy limit. For curves measured with varying pressure the deviation limit is $u(P)=\pm0.005$ MPa and for those measured with varying temperature the deviation limit is $u(T)=\pm0.01$ K (or $u(T)=\pm0.1$ K when using an electric coil heater). The uncertainty in mole fraction, due to the filling accuracy, results in additional deviation of the measured equilibria points. Plotting the three phase curve of the mixture with different compositions can be used to identify if the measured samples are accurately filled and measured.

The Cailletet experiments are executed with different molecular structured LCs in combination with CO_2 and H_2. The molecule name and structure, purity and its phase transition of the LCs used are shown in table 4.1. Used LCs are selected based on their different molecular structure (e.g. benzene ring/cyclohexyl ring and polarity). Laboratory data can be found in Appendix C. The chemicals were used as received.

Table 4.1: Chemicals used in experiment. Description of symbols used: (N) nematic, (S) solid, (I) isotropic, (Sm) smectic, (C) critical point.

Name, abbreviation and structure	Brand, purity	Phase transitions
4'-pentylbiphenyl-4-carbonitrile (5CB)	Alfa Aesar >99 wt %	T_{SN}=297.15 K [12] T_{NI}=308.45 K [12]
4'-Heptyloxy-4-cyanobiphenyl (7OCB)	Alfa Aesar >99 wt %	T_{SN}=326.65 K [12] T_{NI}=348.15 K [12]
4-ethyl-4'-propyl-1,1'bi(cyclohexyl) (2,3-BCH)	Merck >98 wt %	T_{SmI}=341 K [4]
4-propyl-4'-butyl-bicyclohexyl (3,4-BCH)	Merck >98 wt %	T_{SmI}=370 K [4]
4-((4-(hexyloxy)benzylidene)amino) benzonitrile (HOBAB)	Frinton Laboratories >98 wt %	T_{SN}= 334.05 K [42] T_{NI}= 375.10 K [42]
Phenyl cyclohexyl (PCH-type) *Confidential*	Merck >98 wt %	T_{SN}=318.15[1] K T_{NI}=319.15[1] K
Carbon dioxide(CO$_2$) O=C=O	Linde gas 4.5	T_c=304.1282 K [6] P_c=7.3773 MPa [6]
Hydrogen (H$_2$) H$_2$	Hoekloos 5.0	T_c=32.97 K [26] P_c=1.293 MPa [26]

[1]Provided by Merck

4.2 Bubblepoint curve CO_2

In figure 4.2 the P,T-diagram of pure CO_2 is shown, obtained from a Cailletet experiment and checked with an appropriate EOS [6]. The data set of the measured and calculated CO_2 vapour pressure is given in Appendix B.
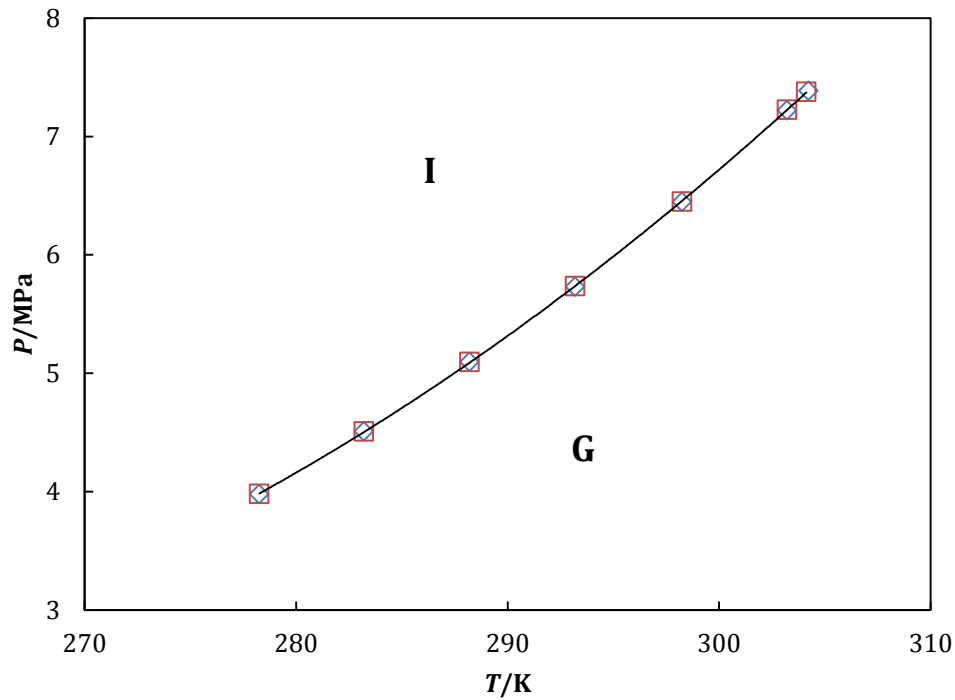
Figure 4.2: P,T-diagram of CO_2. Description of symbols used: (blue ◇) I↔V experimental, (red □) I↔V equation of state. The polynomial curve represents the bubblepoint curve of CO_2.

The accuracy of the experimentally measured vapour pressure of CO_2 is $u(P)=\pm0.005$ MPa. When comparing the experimental results with the EOS a maximum deviation of $u(P)=\pm0.005$ MPa was found, this is between the accuracy limit set by the pressure balance. This means that the measured CO_2 has, within the accuracy range, similar VLE points as the EOS and therefore the CO_2 is pure.

4.3 Experimental results of binary mixtures liquid crystals and carbon dioxide

4.3.1 Pentyl cyanobiphenyl (5CB) + CO$_2$

4'-pentylbiphenyl-4-carbonitrile (5CB) has a nematic phase in between the solid and isotropic liquid phase. Pure component solid to nematic phase transition (S→N) occurs at 288 K, nematic to isotropic liquid phase transition (N→I) occurs at 307 K (table 4.1). The phase transition enthalpy, nematic to isotropic (N→I), is 0.4 kJ/mol [12]. For the binary mixture of 5CB + 1 mass % (5.5 mole %) CO$_2$, six different phase equilibria lines are measured (figure 4.3, Table C.3): Isotropic + Gas to Isotropic (I+G↔I), the Nematic + Isotropic to Isotropic (N+I↔I), the Nematic to Nematic + Isotropic (N↔N+I), the Nematic + Gas to Nematic (N+G↔N), the Nematic + Gas to Nematic + Isotropic (N+G↔N+I) and the three-phase line: Nematic + Gas to Isotropic + Gas (N+G↔I+G). The two-phase area (N + I) has a width of approximately ΔT=0.50 K.
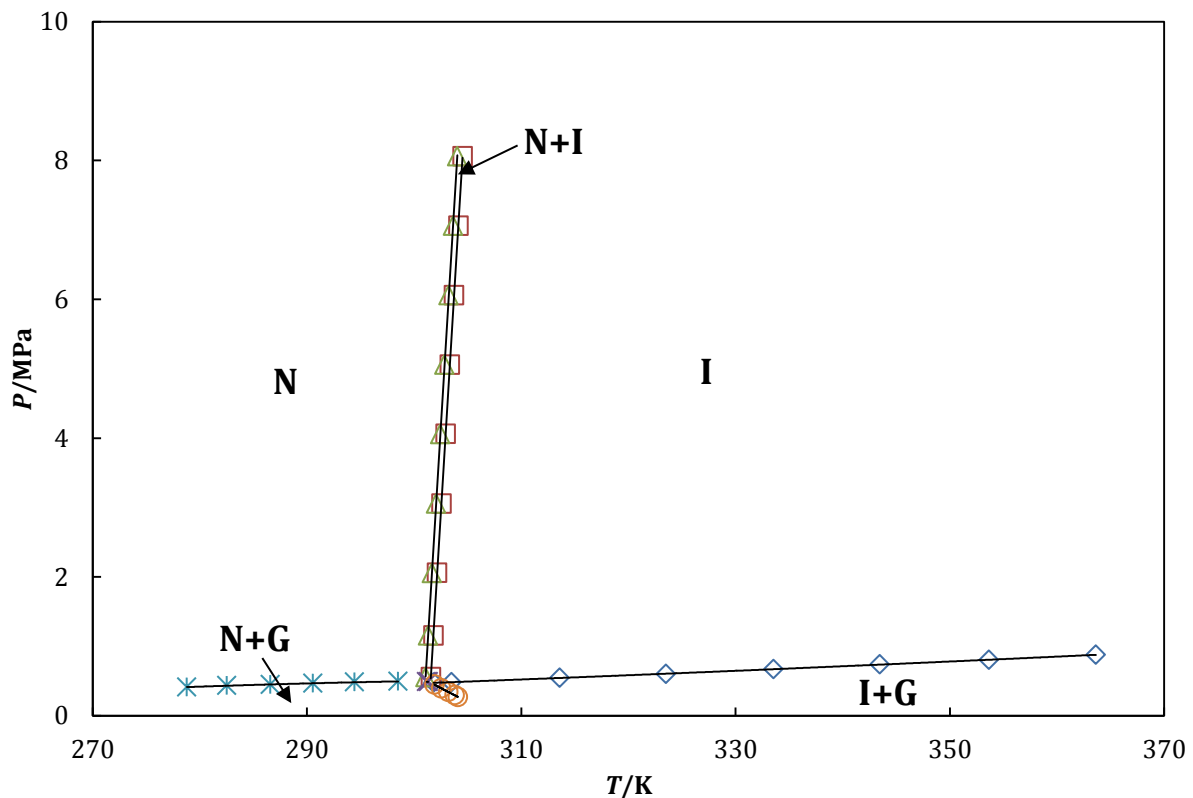
Figure 4.3: *P,T*-diagram of pentyl cyanobiphenyl (5CB) + 5.5 mole % CO$_2$. Description of symbols used: (blue ◇) I↔G+I, (red ☐) N+I↔I, (green △) N↔N+I, (purple ✕) N+I↔N+G, (light blue ✳) N↔N+G, (orange ◯) N+G↔I+G.

The mixture ratio of the filling is 5.5 mole % CO$_2$ and 94.5 mole % 5CB. Temperature was controlled using a Lauda RC20 thermostatic bath, accuracy range within $u(T)$=±0.01 K. The pressure was measured using a dead weight gauge (Budenberg) with an accuracy of $u(P)$=±0.005 MPa.

The phase transition lines are measured for two different mixture ratios and are plotted in a *P,T*-diagram (figure 4.4), including the pure LC nematic to isotropic phase transition. The three-phase curve (NIG) and the nematic to isotropic liquid line (NI) are used to verify and validate the measurements. Extrapolating the three-phase line (NIG) must result in interception of the nematic to isotopic (NI) line of the pure component.
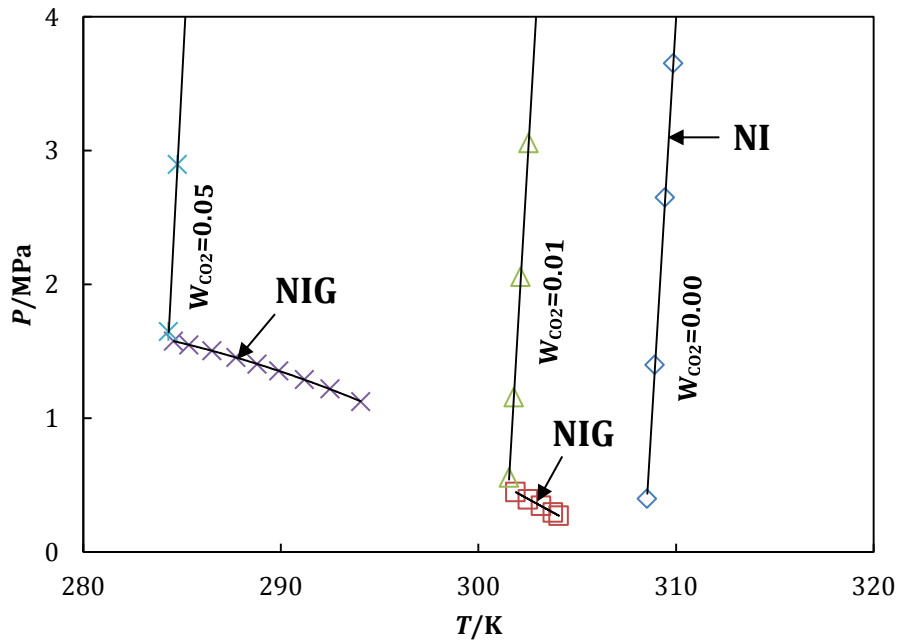
Figure 4.4: *P,T*-diagram of pentyl cyanobiphenyl (5CB) with different mass % of CO_2. Description of symbols used: (blue ◇) N↔I [4], (red ▢) N+G↔I+G, (green △) N+I↔I, (purple ✕) N+G↔I+V [4], (light blue ✳) N+I↔I [4].

The end of the three-phase curve (NIG) intercepts with the nematic to isotropic (NI) line from the pure LC, accuracy of the nematic to isotropic phase transition (N→I) line measurement is *u*(*T*)=±0.01 K. From this the purity of the components in the mixture can be concluded.

4.3.2 Heptyloxy cyanobiphenyl (7OCB) + CO_2

4'-Heptyloxy-4-cyanobiphenyl (7OCB) has a nematic phase in between the solid and isotropic liquid phase. Pure component solid to nematic phase transition (S→N) occurs at 326.65 K, nematic to isotropic liquid phase transition (N→I) occurs at 348.15 K (table 4.1). Phase transition enthalpy, nematic to isotropic (N→I), is 0.6 kJ/mol [12]. For the binary mixture of 7OCB + 1 mass % (6.3 mole %) CO_2, six different phase equilibria lines are measured (figure 4.5, Table C.4): Isotropic + Gas to Isotropic (I+G↔I), the Nematic + Isotropic to Isotropic (N+I↔I), the Nematic to Nematic + Isotropic (N↔N+I), the Nematic + Gas to Nematic (N+G↔N), the Nematic + Gas to Nematic + Isotropic (N+G↔N+I) and the three-phase line: Nematic + Gas to Isotropic + Gas (N+G↔I+G). The two-phase area (N + I) has a width of approximately ΔT=0.10 K.
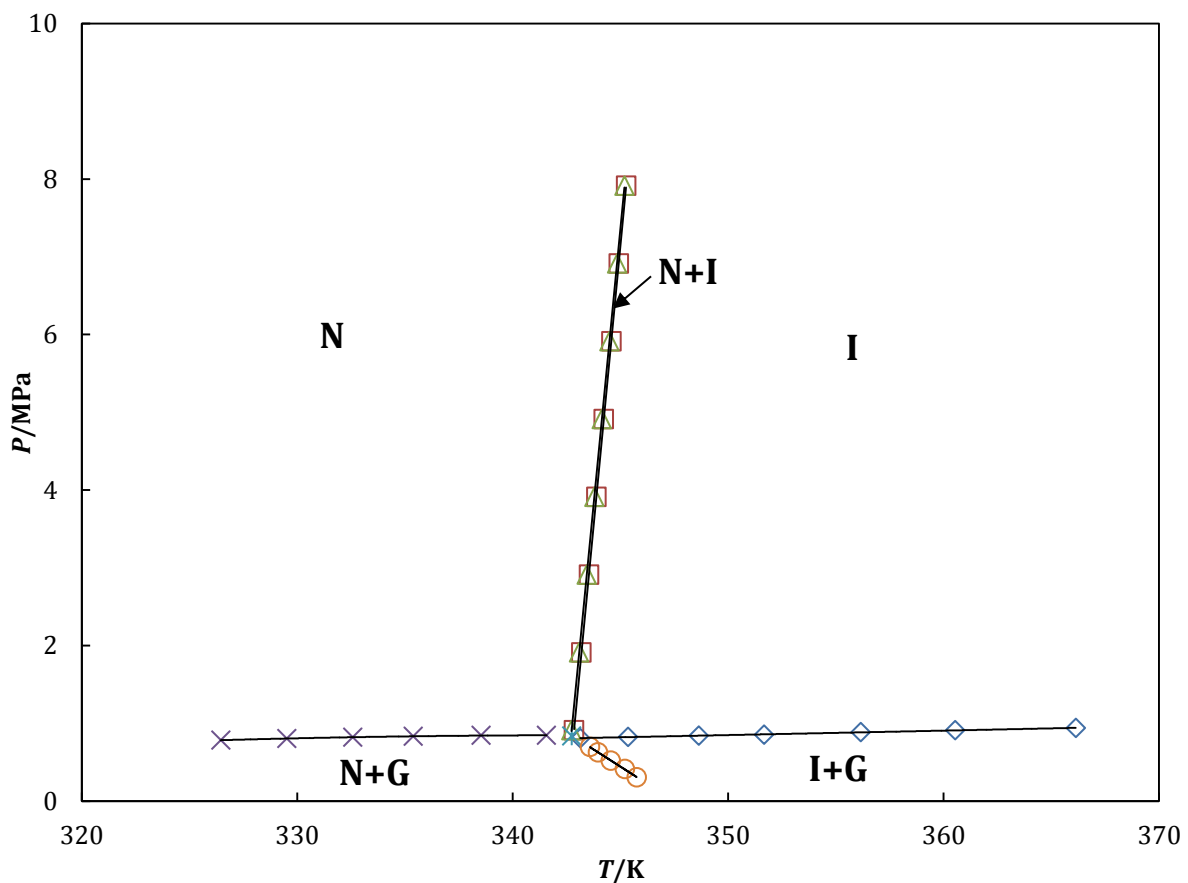
Figure 4.5: *P,T*-diagram of heptyloxy cyanobiphenyl (7OCB) + 6.3 mole % CO_2. Description of symbols used: (blue ◇) I↔G+I, (red □) N+I↔I, (green △) N↔N+I, (purple ✕) N ↔N+G, (light blue ✳) N+I↔N+G, (orange ◯) N+G↔I+G.

The mixture ratio of the filling is 6.3 mole % CO_2 and 93.7 mole % 7OCB. Temperature was controlled using a Lauda RC20 thermostatic bath, accuracy range within $u(T)$=±0.01 K. The pressure was measured using a dead weight gauge (de Wit) with an accuracy of $u(P)$=±0.005 MPa.

The phase transition lines are measured for two different mixture ratios and are plotted in a *P,T*-diagram (figure 4.6), including the pure LC nematic to isotropic phase transition. The three-phase curve (NIG) and the nematic to isotropic liquid line (NI) are used to verify and validate the measurements. Extrapolating the three-phase line (NIG) must result in interception of the nematic to isotopic (NI) line of the pure component.
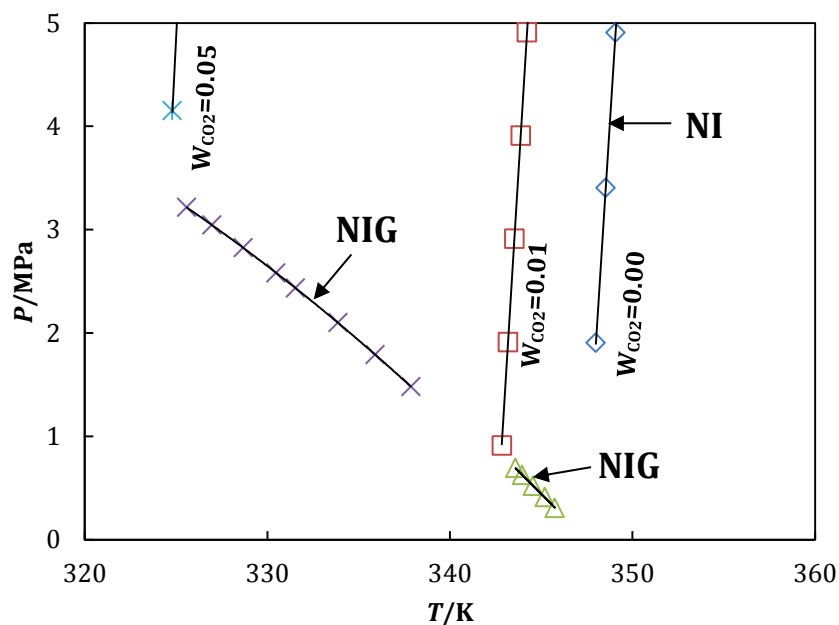
Figure 4.6: *P,T*-diagram of heptyloxy cyanobiphenyl (7OCB) with different mass % of CO_2. Description of symbols used: (blue ◇) N↔I [44], (red □) N+I↔I, (green △) N+G↔I+G, (light blue ✳) N+I↔I [44], (purple ✕) N+G↔I+G [44].

The end of the three-phase curve (NIG) intercepts with the nematic to isotropic (NI) line from the pure LC, accuracy of the nematic to isotropic phase transition (N→I) line measurement is $u(T)=\pm0.01$ K. From this the purity of the components in the mixture can be concluded.

4.3.3 Ethyl propyl bicyclohexyl (2,3-BCH) + CO$_2$

4-ethyl-4'-propyl-1,1'bi(cyclohexyl) (2,3-BCH) has a smectic phase in between the solid and isotropic liquid phase. Pure component solid to smectic phase transition (Sm→I) occurs at 341 K (table 4.1). For the binary mixture of 2,3-BCH + 1 mass % (5.2 mole %) CO$_2$, three different phase equilibria lines are measured (figure 4.7, Table C.5): Isotropic + Gas to Isotropic (I+G↔I), the Smectic + Isotropic to Isotropic (Sm+I↔I) and the three-phase line: Smectic + Gas to Isotropic + Gas (Sm+G↔I+G).
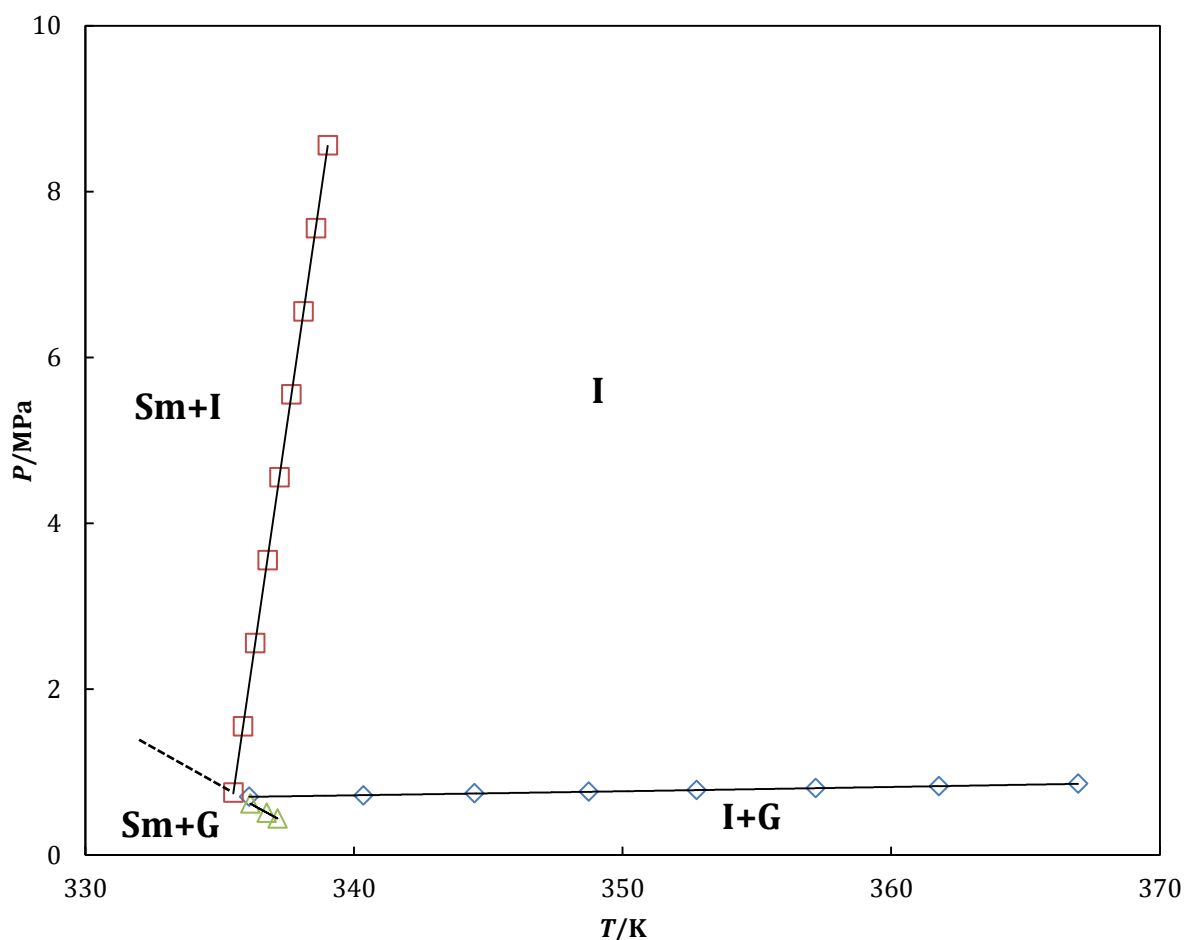
Figure 4.7: *P,T*-diagram of ethyl propyl bicyclohexyl (2,3-BCH) + 5.2 mole % CO$_2$. Description of symbols used: (blue ◇) I↔G+I, (red □) Sm+I↔I, (green △) Sm+G↔I+G.

The mixture ratio of the filling is 5.2 mole % CO$_2$ and 94.8 mole % 2,3-BCH. Temperature was controlled using a Lauda RC20 thermostatic bath, accuracy range within $u(T)=\pm0.01$ K. The pressure was measured using a dead weight gauge (Budenberg) with an accuracy of $u(P)=\pm0.005$ MPa.

The phase transition lines are measured for two different mixture ratios and are plotted in a *P,T*-diagram (figure 4.8), including the pure LC smectic to isotropic phase transition. The three-phase curve (SmIG) and the nematic to isotropic liquid line (SmI) are used to verify and validate the measurements. Extrapolating the three-phase line (SmIG) must result in interception of the smectic to isotopic (SmI) line of the pure component.
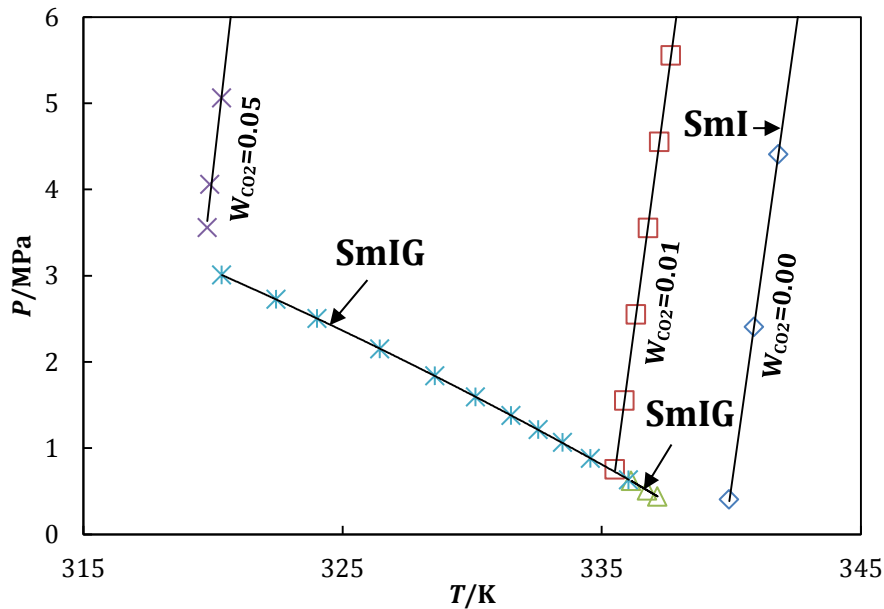
Figure 4.8: *P,T*-diagram of ethyl propyl bicyclohexyl (2,3-BCH) with different mass % of CO_2. Description of symbols used: (blue ◇) Sm↔I [4], (red □) Sm+I↔I, (green △) Sm+G↔I+G, (light blue ✳) Sm+I↔I [4], (purple ✕) Sm+G↔I+G [4].

The end of the three-phase curve (SmIG) intercepts with the smectic to isotropic (SmI) line from the pure LC, accuracy of the smectic to isotropic phase transition (Sm→I) line measurement is $u(T)=\pm0.01$ K. From this the purity of the components in the mixture can be concluded.

4.3.4 Propyl butyl bicyclohexyl (3,4-BCH) + CO$_2$

4-propyl-4'-butyl-bicyclohexyl (3,4-BCH) has a smectic phase in between the solid and isotropic liquid phase. Pure component solid to smectic phase transition (Sm→I) occurs at 370 K (table 4.1). For the binary mixture of 3,4-BCH + 1 mass % (5.7 mole %) CO$_2$, three different phase equilibria lines are measured (figure 4.9, Table C.1): Isotropic + Gas to Isotropic (I+G↔I), the Smectic + Isotropic to Isotropic (Sm+I↔I) and the three-phase line: Smectic + Gas to Isotropic + Gas (Sm+G↔I+G).
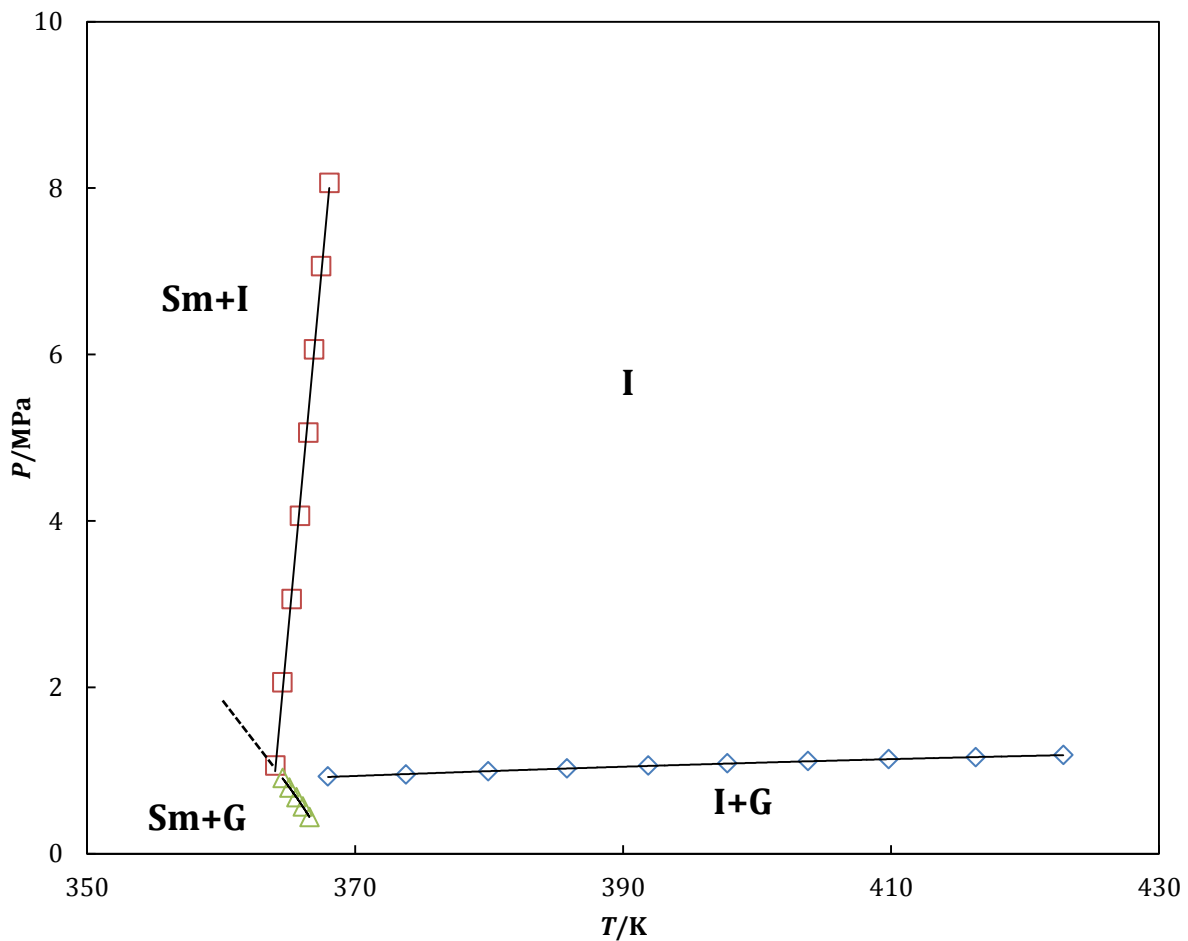
Figure 4.9: *P,T*-diagram of propyl butyl bicyclohexyl (3,4-BCH) + 5.7 mole % CO$_2$. Description of symbols used: (blue ◇) I↔G+I, (red □) Sm+I↔I, (green △) Sm+G↔I+G.

The mixture ratio of the filling is 5.7 mole % CO$_2$ and 94.3 mole % 3,4-BCH. Temperature was controlled using a Shimaden electric coil heater, accuracy range within $u(T)=\pm0.1$ K. The pressure was measured using a dead weight gauge (Budenberg) with an accuracy of $u(P)=\pm0.005$ MPa.

The phase transition lines are measured for two different mixture ratios and are plotted in a *P,T*-diagram (figure 4.10), including the pure LC smectic to isotropic phase transition. The three-phase curve (SmIG) and the nematic to isotropic liquid line (SmI) are used to verify and validate the measurements. Extrapolating the three-phase line (SmIG) must result in interception of the smectic to isotopic (SmI) line of the pure component.
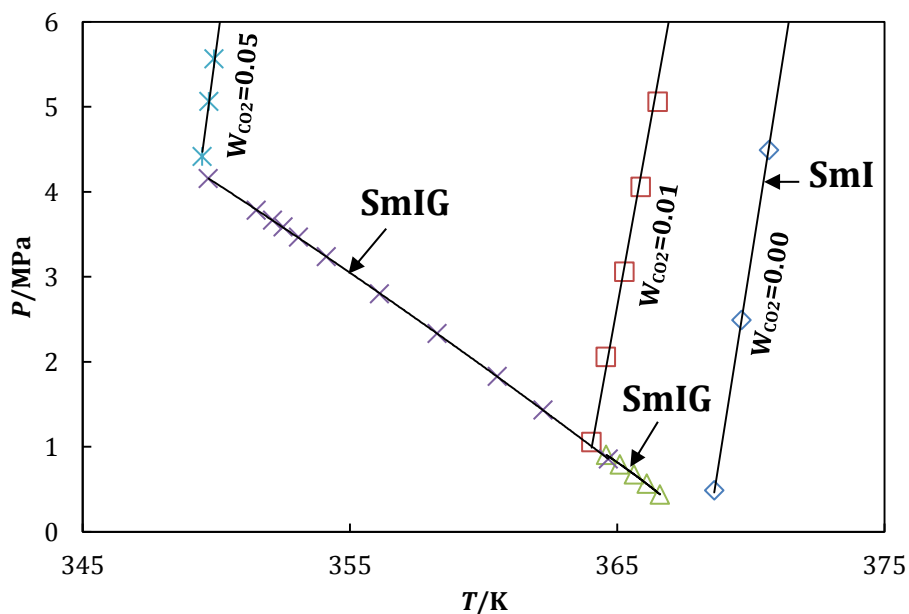
Figure 4.10: *P,T*-diagram of propyl butyl bicyclohexyl (3,4-BCH) with different mass % of CO_2. Description of symbols used: (blue ◇) Sm↔I [4], (red □) Sm+I↔I, (green △) Sm+G↔I+G, (light blue ✳) Sm+I↔I [4], (purple ✕) Sm+G↔I+G [4].

The end of the three-phase curve (SmIG) intercepts with the smectic to isotropic (SmI) line from the pure LC, accuracy of the smectic to isotropic phase transition (Sm→I) line measurement is $u(T)=\pm0.01$ K. From this the purity of the components in the mixture can be concluded.

4.3.5 Hexyloxybenzylidene aminobenzonitrile (HOBAB) + CO_2

4-((4-(hexyloxy)benzylidene)amino)benzonitrile (HOBAB) has a nematic phase in between the solid and isotropic liquid phase. Pure component solid to nematic phase transition (S→N) occurs at 334.05 K, nematic to isotropic liquid phase transition (N→I) occurs at 375.10 K (table 4.1). Phase transition enthalpy, nematic to isotropic, is 1.75 kJ/mol [42]. For the binary mixture of HOBAB + 1 mass % (6.3 mole %) CO_2, seven different phase equilibria lines are measured (figure 4.11, Table C.2): Isotropic + Gas to Isotropic (I+G↔I), the Nematic + Isotropic to Isotropic (N+I↔I), the Nematic to Nematic + Isotropic (N↔N+I), the Nematic + Gas to Nematic (N+G↔N), the Nematic + Gas to Nematic + Isotropic (N+G↔N+I), the Solid + Nematic to Nematic (S+N↔N) and the three-phase line: Nematic + Gas to Isotropic + Gas (N+G↔I+G). The two-phase area (N + I) has a width of approximately ΔT=0.67 K.
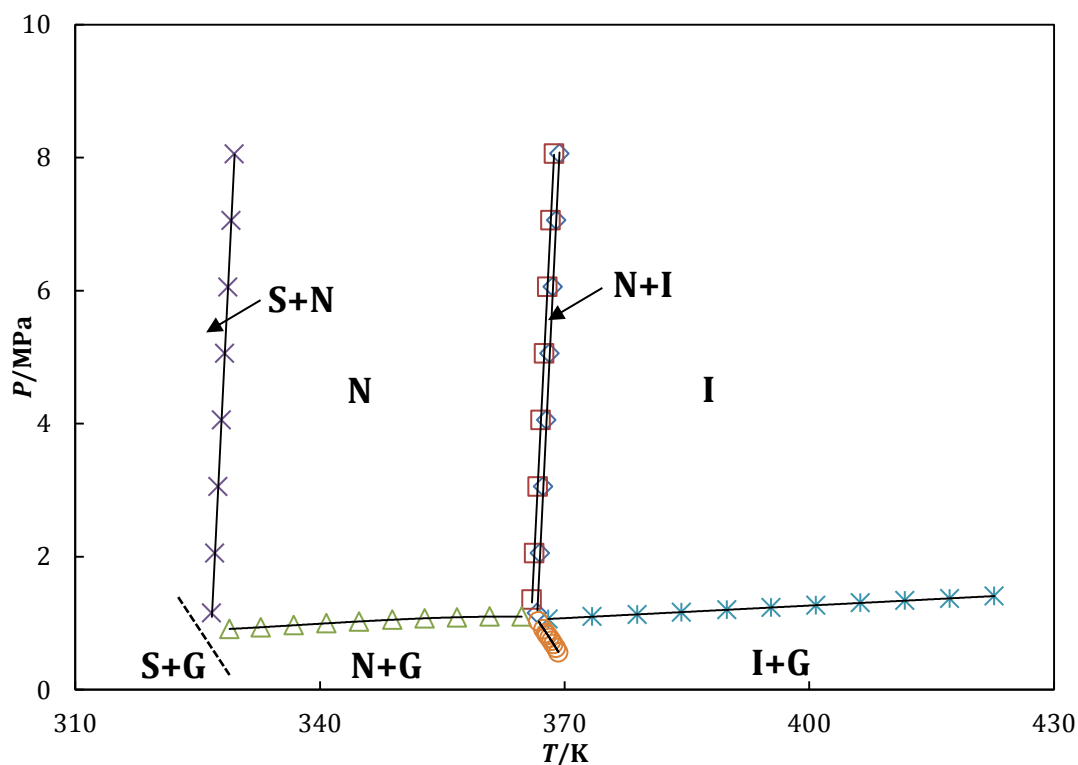
Figure 4.11: *P,T*-diagram of hexyloxybenzylidene aminobenzonitrile (HOBAB) + 6.3 mole % CO_2. Description of symbols used: (light blue ✳) I↔I+G, (blue ◇) N+I↔I, (red □) N↔N+I, (green △) N↔N+G, (orange ○) N+G↔I+G, (purple ✕) S+N↔N.

The mixture ratio of the filling is 6.3 mole % CO_2 and 93.7 mole % HOBAB. Temperature was controlled using a Lauda RC20 thermostatic bath for temperatures until 370 K (accuracy range within $u(T)=\pm0.01$ K) and above 370 K a Shimaden electric coil heater was used (accuracy range within $u(T)=\pm0.1$ K. The pressure was measured using a dead weight gauge (Budenberg) with an accuracy of $u(P)=\pm0.005$ MPa.

4.3.6 Phenyl cyclohexyl (PCH-type) + CO$_2$

Phenyl cyclohexyl (PCH-type) has a nematic phase in between the solid and isotropic liquid phase. Pure component solid to nematic phase transition (S→N) occurs at 315.85 K, nematic to isotropic liquid phase transition (N→I) occurs at 319.05 K (table 4.1). For the binary mixture of PCH-type + 1 mass % (5.0 mole %) CO$_2$, seven different phase equilibria lines are measured (figure 4.12, Table C.6): Isotropic + Gas to Isotropic (I+G↔I), the Nematic + Isotropic to Isotropic (N+I↔I), the Nematic to Nematic + Isotropic (N↔N+I), the Nematic + Gas to Nematic (N+G↔N), the Nematic + Gas to Nematic + Isotropic (N+G↔N+I), the Solid + Isotropic to Isotropic (S+I↔I) and the three-phase line: Nematic + Gas to Isotropic + Gas (N+G↔I+G). The two-phase area (N + I) has a width of approximately ΔT=0.97 K.
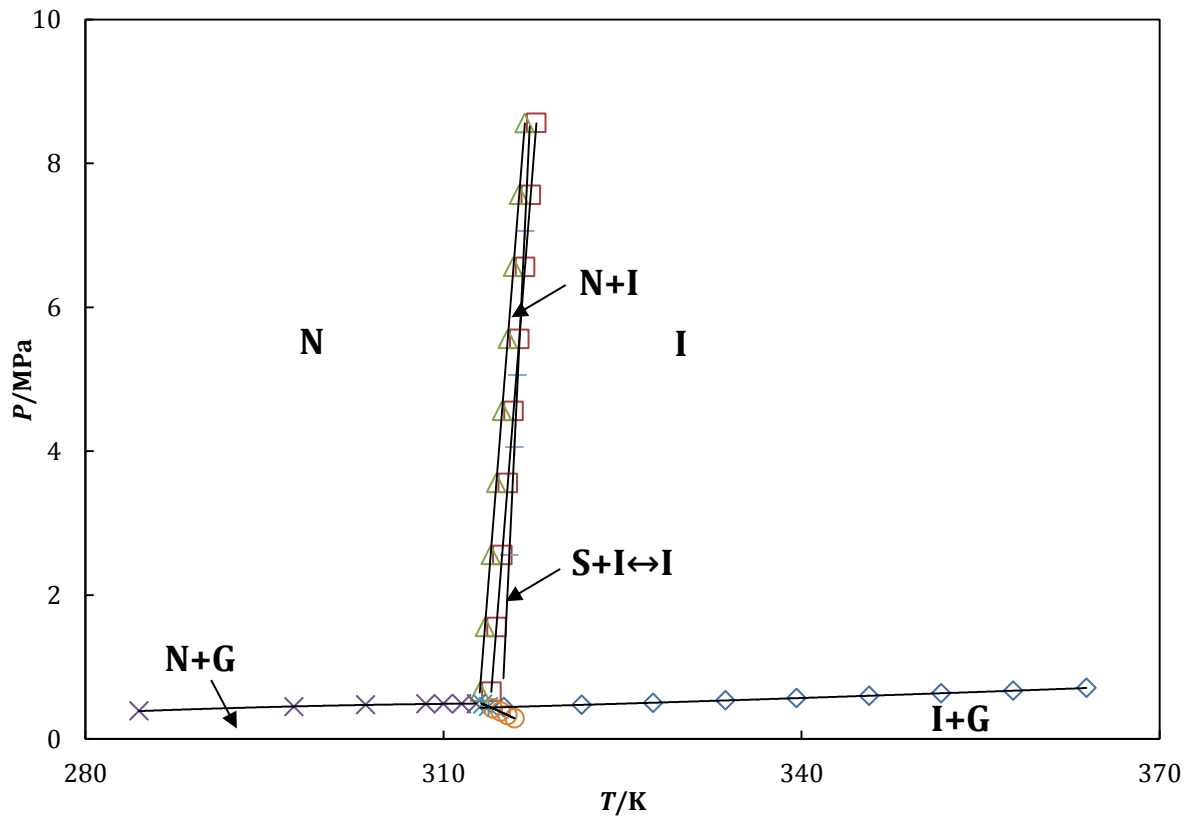
Figure 4.12: *P,T*-diagram of phenyl cyclohexyl (PCH-type) + 5.0 mole % CO$_2$. Description of symbols used: (blue ◇) I↔I+G, (red ☐) N+I↔ I, (green △) N↔N+I, (purple ✕) N↔N+G, (light blue ✳) N+I↔N+G, (orange ◯) N+G↔I+G, (light blue +) S+I↔I

The mixture ratio of the filling is 5.0 mole % CO$_2$ and 95.0 mole % PCH-type. Temperature was controlled using a Lauda RC20 thermostatic bath, accuracy range within $u(T)=\pm0.01$ K. The pressure was measured using a dead weight gauge (Budenberg) with an accuracy of $u(P)=\pm0.005$ MPa. The SI-line is present in the isopleth of 5.0 mole %, meaning that the nematic phase is already metastable and therefore PCH-type is a low capacity LC.

The phase transition line measured 1 mass % CO_2 and the pure LC nematic to isotropic phase transition are plotted in a P,T-diagram (figure 4.13). The three-phase curve (NIG) and the nematic to isotropic liquid line (NI) are used to verify and validate the measurements. Extrapolating the three-phase line (NIG) must result in interception of the nematic to isotopic (NI) line of the pure component.
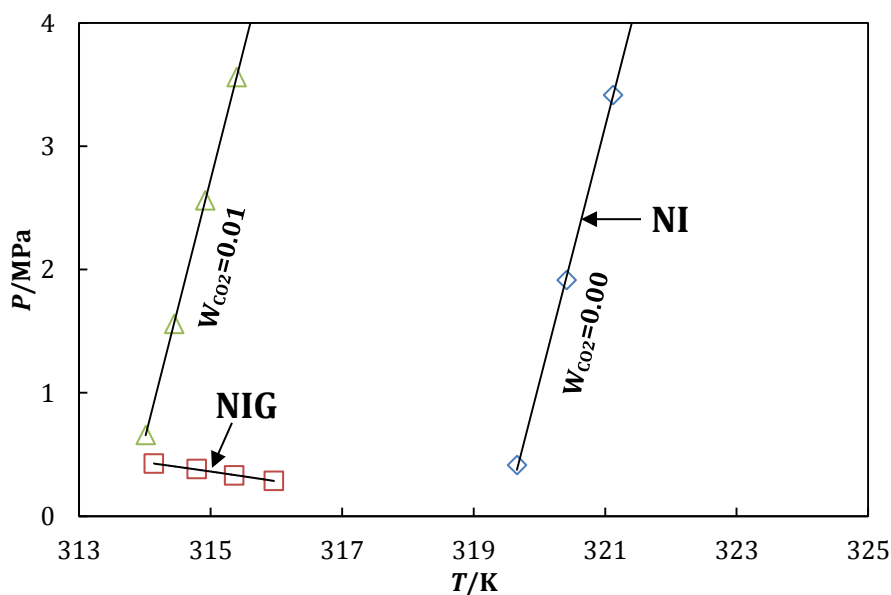
Figure 4.13: P,T-diagram of phenyl cyclohexyl (PCH-type) with different mass % of CO_2. Description of symbols used: (blue ◇) N↔I [44], (red □) N+G↔I+G, (green △) N+I↔I, (purple ✕) N+I↔I.

The end of the three-phase curve (NIG) intercepts with the nematic to isotropic (NI) line from the pure LC, accuracy of the nematic to isotropic phase transition (N→I) line measurement is $u(T)=\pm0.01$ K. From this the purity of the components in the mixture can be concluded.

4.3.7 Comparison LC + CO$_2$ experimental results

The three phase curves obtained from the measurement can be compared to measurements of different compositions to validate the purity of the components. Another comparison can be made in CO$_2$ solubility with use of Henry coefficients.

The three phase curve connects the different compositions and therefore can be used to validate the experimental measurements. The available LC + CO$_2$ three phase curves (CIG) are shown in figure 4.14 to validate the consistency of the experimental measurement of 1 and 5 mass % CO$_2$.
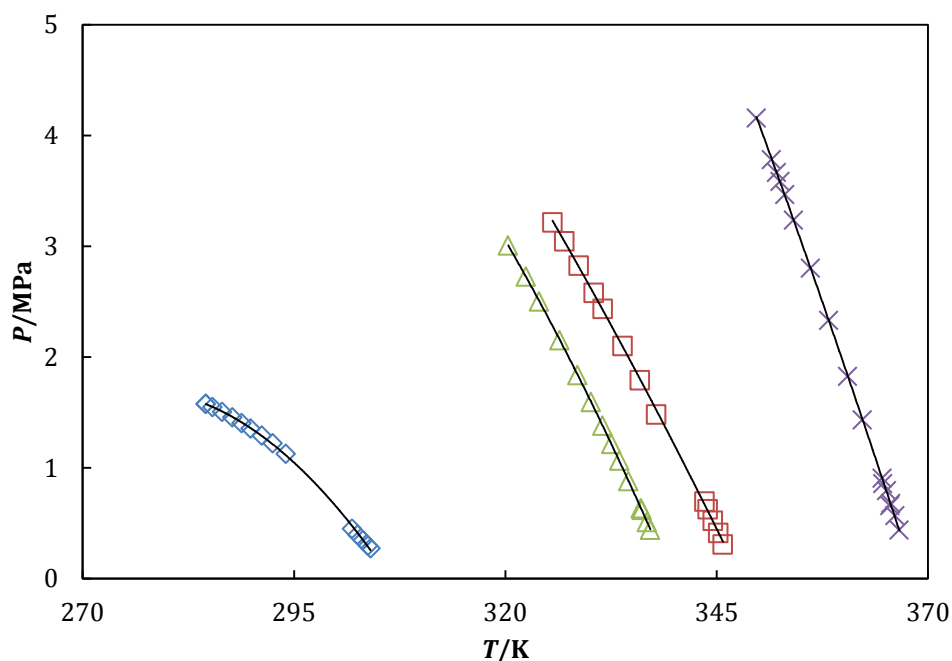
Figure 4.14: Three phase (CIG) curves of Liquid Crystals with CO$_2$. Description of symbols used: (blue ◇) 5CB + CO$_2$, (red □) 7OCB + CO$_2$, (green △) 2,3-BCH + CO$_2$, (purple ✕) 3,4-BCH + CO$_2$.

The CIG curves measured (1 mass % CO$_2$) seem to be in agreement with those previously measured (5 mass % CO$_2$) for 5CB, 7OCB, 2,3-BCH and 3,4-BCH, furthermore the CIG curve intersect with the pure component phase transition (CI).

The solubility of CO_2 in the LC can be concluded from the Henry coefficients found from the experimental data. The mole fraction of CO_2 in the binary mixture is low enough to comply with Henry's law. Henry coefficients (Appendix D) are calculated from the fugacity coefficients obtained from ALLPROPS. The small mole fraction (5-6.3 mole %) of CO_2 in the solvent enables to simplify the calculation of the Henry coefficient [eq. 1.16] to the following equation [eq. 4.1].

$$H = \frac{\hat{f}_{CO_2}}{x_{CO_2}}$$

4.1

The Henry coefficients of the different binary mixtures are calculated and shown in figure 4.15.
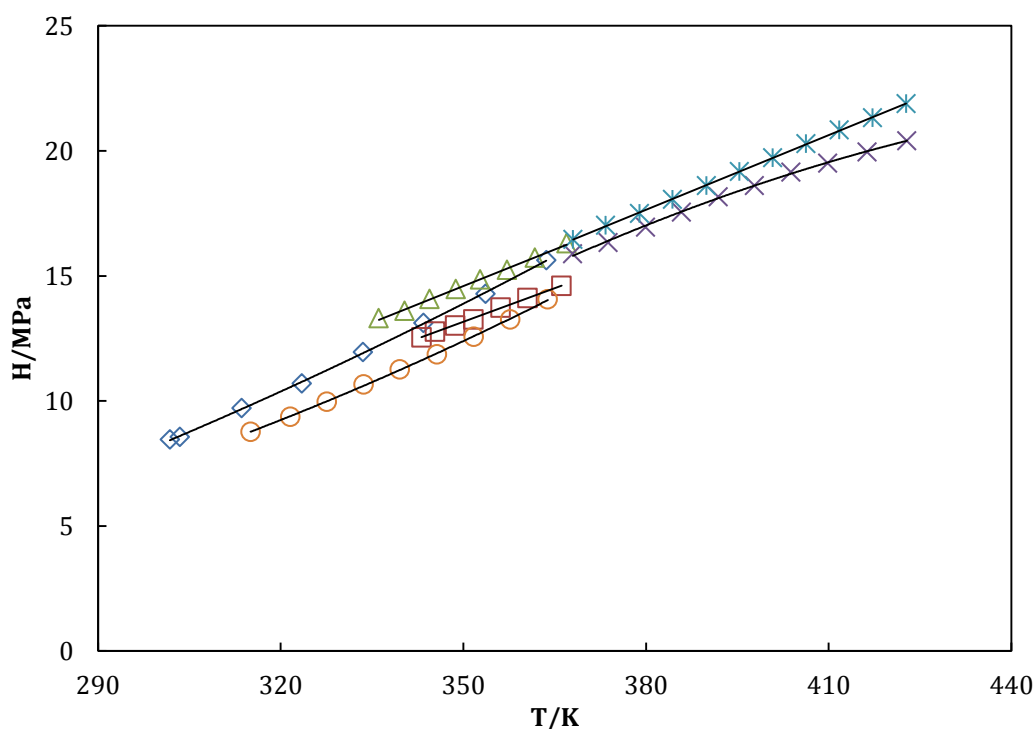
Figure 4.15: Henry coefficients (H) of Liquid Crystals with CO_2. Description of symbols used: (blue ◇) 5CB + CO_2, (red ☐) 7OCB + CO_2, (green △) 2,3-BCH + CO_2, (purple ✕) 3,4-BCH + CO_2, (light blue ✳) HOBAB + CO_2, (orange ○) PCH-type + CO_2.

From figure 4.14 it can be observed that CO_2 solubility in LCs is temperature dependent, furthermore PCH-type has the highest solubility of CO_2 (e.g. lowest Henry coefficients) and HOBAB the lowest solubility of CO_2.

4.4 Experimental results of binary mixtures liquid crystals and hydrogen

The phase behaviour of LC with H_2 in the Cailletet setup are visualized in P,T-diagrams. The H_2 experiments are only executed to verify the solubility (e.g. Henry coefficients) of H_2 in the binary mixture, therefore only the bubblepoint lines are measured in this stage of the experiments.

4.4.1 Ethyl propyl bicyclohexyl (2,3-BCH) + H_2

4-ethyl-4'-propyl-1,1'bi(cyclohexyl) (2,3-BCH) has a smectic phase in between the solid and isotropic liquid phase. Pure component solid to smectic phase transition (Sm→I) occurs at 341 K (table 4.1, Table C.7). For the binary mixture of 2,3-BCH + 5.0 mole % H_2, the bubblepoint curve is the only phase equilibrium line measured (figure 4.16): Isotropic + Gas to Isotropic (I+G↔I). The mixture is measured in the Cailletet setup with use of a thermostatic bath, accuracy range within $u(T)=\pm0.01$ K. The pressure was measured using a dead weight gauge (de Wit) with an accuracy of $u(P)=\pm0.005$ MPa.
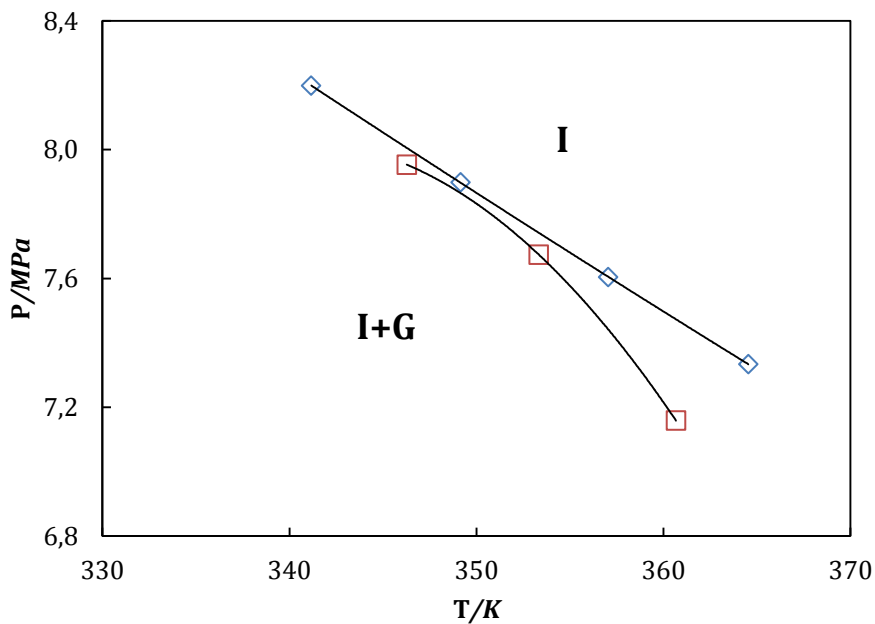
Figure 4.16: P,T-diagram bubblepoint curve of ethyl propyl bicyclohexyl (2,3-BCH) + 5.0 mole % H_2. Description of symbols used: (blue ◇) 1st measurement, (red □) 2nd measurement.

The first measurement was executed at 16th of April and the second, to validate the first measurement, was executed at 18th of April. Clearly the bubblepoint curve dropped over 2 days, implicating that the concentration of H_2 in the mixture decreased. The curvature in the 2nd measurement could be an indication that the decrease of H_2 is accelerated or partly enabled due to a higher temperature.

4.4.2 Phenyl cyclohexyl (PCH-type) + H_2

Phenyl cyclohexyl (PCH-type) has a nematic phase in between the solid and isotropic liquid phase. Pure component solid to nematic phase transition (S→N) occurs at 315.85 K, nematic to isotropic liquid phase transition (N→I) occurs at 319.05 K (table 4.1, Table C.8). For the binary mixture of PCH-type + 3.0 mole % H_2, the bubblepoint curve is the only phase equilibrium line measured (figure 4.17): Isotropic + Gas to Isotropic (I+G↔I). A second composition of PCH-type + 10 mole % H_2 was measured in the high pressure Autoclave (1000 bar). The mixture is measured in the Cailletet setup with use of a thermostatic bath, accuracy range within $u(T)=\pm0.01$ K. The pressure was measured using a dead weight gauge (de Wit) with an accuracy of $u(P)=\pm0.005$ MPa.
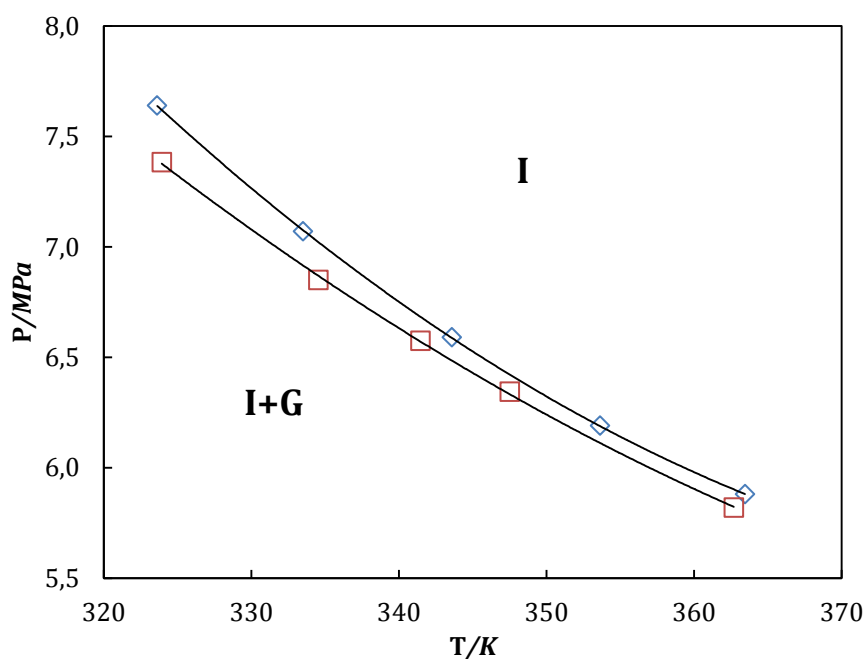
Figure 4.17: *P,T*-diagram bubblepoint curve of phenyl cyclohexyl (PCH-type) + 3.0 mole % H_2. Description of symbols used: (blue ◇) 1st measurement, (red □) 2nd measurement.

The first measurement was executed from the 18th until the 25th of March with every day measured 10 K increase in temperature. The second measurement was executed from 8th until the 9th of April, which results in a bubblepoint curve lower than the one measured before. In the 1000 bar Autoclave, PCH-type + 10 mole % H_2, the same decrease of bubblepoint pressure over time was found. This implicates that the concentration of H_2 in the mixture decreased.

4.4.3 Heptyloxy cyanobiphenyl (7OCB) + H$_2$

4'-Heptyloxy-4-cyanobiphenyl (7OCB) has a nematic phase in between the solid and isotropic liquid phase. Pure component solid to nematic phase transition (S→N) occurs at 326.65 K, nematic to isotropic liquid phase transition (N→I) occurs at 348.15 K (table 4.1, Table C.9). For the binary mixture of 7OCB + 3.0 mole % H$_2$, the bubblepoint curve is the only phase equilibrium line measured (figure 4.18): Isotropic + Gas to Isotropic (I+G↔I). The mixture is measured in the Cailletet setup with use of an electric coil heater (Shimaden), accuracy range within $u(T)=\pm0.1$ K. The pressure was measured using a dead weight gauge (Budenberg, 1000 bar) with an accuracy of $u(P)=\pm0.005$ MPa.
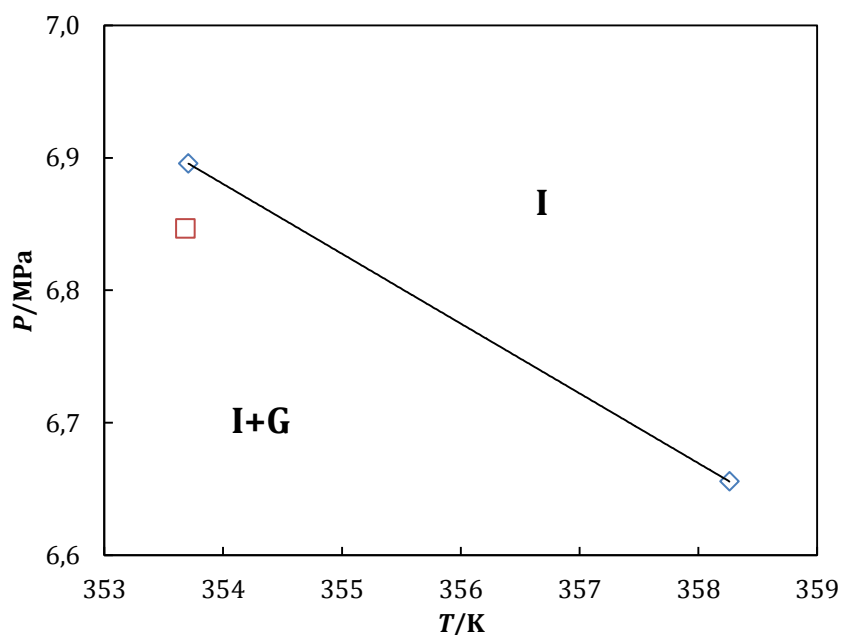
Figure 4.18: *P,T*-diagram bubblepoint curve of heptyloxy cyanobiphenyl (7OCB) + 3.0 mole % H$_2$. Description of symbols used: (blue ◇) 1st measurement, (red □) 2nd measurement.

The first measurement was executed at 26th of April and the second, to validate the first measurement, was executed at 1st of May. Clearly the bubblepoint curve dropped over a few days, implicating that the concentration of H$_2$ in the mixture decreased.

4.4.4 Hydrogen measurement implication

The experimental results of the solubility measurements with H_2 show that the bubblepoint pressure of the sample decreases over time. A logical conclusion would be that the concentration of H_2 decreases over time. Possible causes for this decrease are a reaction of H_2 with an impurity or with the sample, or diffusion of H_2 through the sample tube. To rule out the first hypothesis, the presence of a reaction, at first the presence of a reaction between the liquid crystal itself and H_2 is ruled out by using a glass-coated stirrer to prevent catalysis, and liquid crystals with only saturated bonds were used. This did not solve the problem. Mercury is not known for catalysing hydrogenations. Secondly, the presence of impurities has been examined. First of all, liquid crystals of different suppliers were used to exclude contamination of an impurity caused by a specific production process. Next, the purity of one of the liquid crystals (PCH-type) was determined with DSC, yielding a purity of 99.96%. This means that, as a result of this high purity, impurities in the liquid crystal are an unlikely cause for this phenomenon. A last impurity which cannot be ruled out completely is the presence of a small amount of vacuum grease in the sample, which is used for sealing the sample from the environment during the filling procedure. However, if grease is present at all, it will be at very low amounts. The hypothesis of H_2 diffusion is more difficult to test.

However, this behaviour is not abnormal for hydrogen measurements. In the publication of S. Raeissi et al. [45], the solubility of hydrogen in an ionic liquid measured with a Cailletet setup, a decrease in bubblepoint pressure over time is found as well.

4.5 Conclusion experimental data

Phase behaviour of LCs with CO_2 is measured experimentally to validate feasibility of different LC structures for syngas CC process. The experimentally found bubblepoint curves of the binary mixtures of LCs and CO_2 can be used to compare the solubility (e.g. Henry coefficients) of CO_2 in the LCs. From the Henry coefficients it can be concluded that the highest solubility of CO_2 is found with PCH-type (figure 4.12), and the lowest with HOBAB. Unfortunately, the binary mixtures of LC with H_2 are not measured correctly yet, due to the decrease of the bubblepoint curve over time.

Comparison between the Henry coefficients of CO_2 in 5CB and 7OCB shows that more polar molecules have a higher solubility of CO_2, 7OCB has a higher solubility of CO_2. Differences between 5CB and 7OCB are one additional CH_2 group and an ether (CH_2O) group, which increases the solubility of CO_2. PCH-type is a cyclohexylbenzene based structure, which in comparison with the other LCs has a high solubility of CO_2. From this it is expected that cyclohexylbenzene structures have a higher solubility of CO_2 than biphenyl and bicyclohexyl structures. From this it is expected that cyclohexylbenzene based LCs have a higher solubility of CO_2 than biphenyl bases LCs. Although 7OCB and HOBAB have very similar molecular structures the solubility difference is high, this difference could be explained by the double bonded nitrogen in between the two phenyl rings. Bicyclohexyl structures, 2,3-BCH and 3,4-BCH, have a lower solubility of CO_2 than cyclohexylbenzene based structures, less distinction between CO_2 solubilities is found for biphenyl and bicyclohexyl structures. The 3,4-BCH molecular structure is similar as that of 2,3-BCH except it has a longer hydrocarbon chain next to the cyclohexyl rings. When comparing 2,3-BCH with 3,4-BCH it can be observed that CO_2 solubility is higher in 3,4-BCH, thus an increase in the hydrocarbon chain increases the CO_2 solubility of bicyclohexyl structures.

Bicyclohexyl structures, like 2,3-BCH and 3,4-BCH, have a smectic phase, which is highly viscous. Highly viscous fluids are not usable in the proposed CC process. PCH-type has a higher phase transition (N→I) enthalpy than 5CB and 7OCB at low temperature meaning that higher capacity is expected (van 't Hoff equation, equation 1.18). However, figure 4.10 shows the measured solid + isotropic to isotropic (S+I→I) line, meaning that the nematic phase is metastable, implicating that PCH-type has a low capture capacity and thus is not favourable for the proposed CC process.

Highest Henry coefficients found with the experimental VLE are bicyclohexyl structures (except HOBAB), lowest Henry coefficients with cyclohexylbenzene while in the simulation the highest Henry coefficients are found with biphenyl, the lowest with bicyclohexyl. An ether group (CH_2O) seems to increase solubility in the PSRK simulation, in the experiments the same trend is found when comparing 5CB and 7OCB. In the experiments high solubility of CO_2 in 7OCB is found, this corresponds to the predicted with the PSRK simulation.

5.0 Predictive Soave-Redlich-Kwong Equation of State validation with experimental data

The PSRK EOS is compared to the experimentally measured bubblepoint line to validate the PSRK EOS to simulate binary mixtures of LC and CO_2. In Aspen Plus the PSRK EOS is used to simulate the VLE on identical temperature and mixture ratio as in the experiments. The bubblepoint line of both the experimental data and the PSRK simulation data from Aspen are plotted (figure 5.1-5.6) to identify the accuracy of simulation. The PSRK EOS can only be validated when simulating the VLE of binary mixtures because nematic and/or smectic phases behaviour are not featured in Aspen.

5.1 PSRK EOS VLE simulation of Cailletet data

The 5CB, 7OCB, HOBAB and PCH-type molecule consist of a cyano group, which is not an actual group in UNIFAC. To overcome this modeling obstacle the molecules including a cyano group are modelled with shifting one CH_2 group from the hydrocarbon chain next to the triple bonded nitrogen CH_xCN).
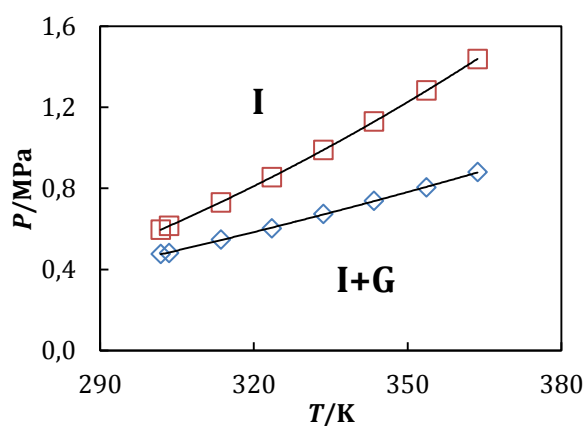
Figure 5.1: *P,T*-diagram bubblepoint curve of 5CB with 5.5 mole % CO_2. Description of symbols used: (blue ◇) experimental data, (red □) PSRK simulation.
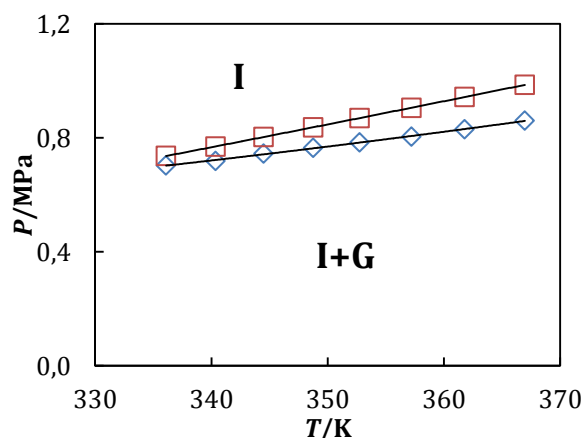
Figure 5.2: *P,T*-diagram bubblepoint curve of 2,3-BCH with 5.2 mole % CO_2. Description of symbols used: (blue ◇) experimental data, (red □) PSRK simulation.
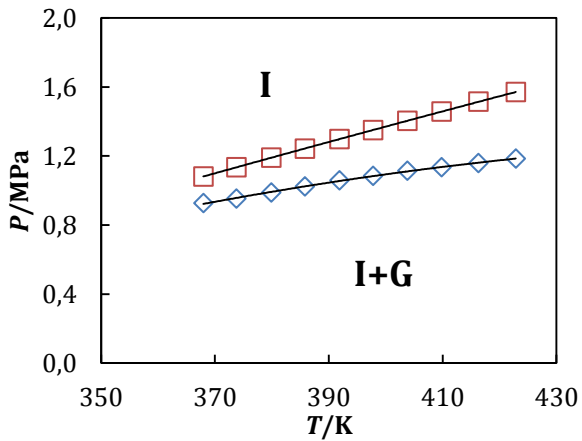
Figure 5.3: *P,T*-diagram bubblepoint curve of 3,4-BCH with 5.2 mole % CO_2. Description of symbols used: (blue ◇) experimental data, (red □) PSRK simulation.
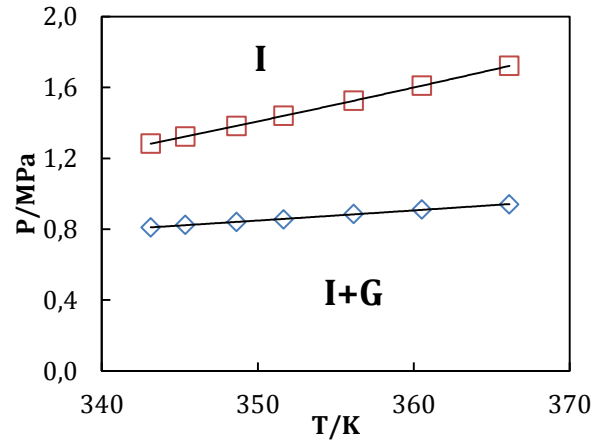
Figure 5.4: *P,T*-diagram bubblepoint curve of 7OCB with 5.7 mole % CO_2. Description of symbols used: (blue ◇) experimental data, (red □) PSRK simulation.
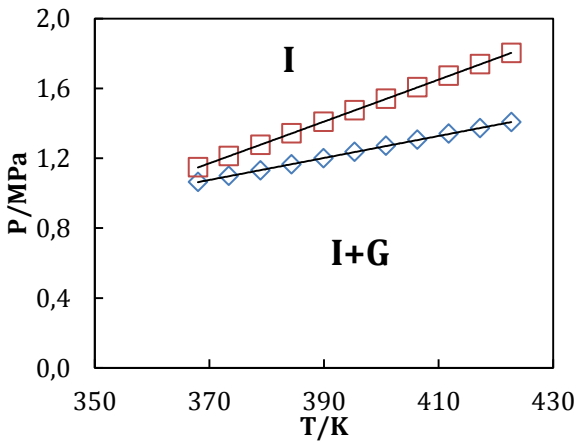
Figure 5.5: *P,T*-diagram bubblepoint curve of HOBAB with 6.3 mole % CO_2. Description of symbols used: (blue ◇) experimental data, (red □) PSRK simulation.
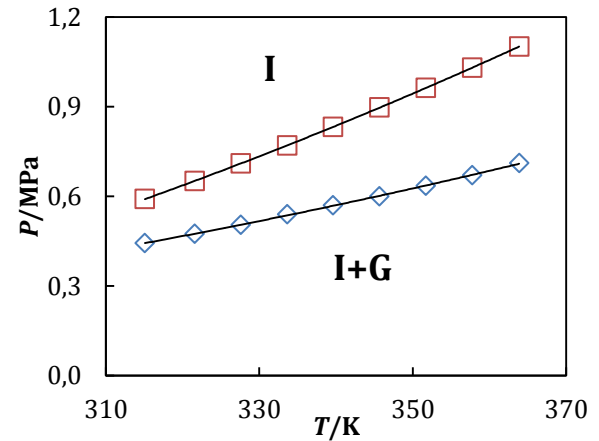
Figure 5.6: *P,T*-diagram bubblepoint curve of PCH-type with 5.0 mole % CO_2. Description of symbols used: (blue ◇) experimental data, (red □) PSRK simulation.

Observed from all six bubblepoint line simulations is that at lower temperature the accuracy of the PSRK simulation increases. Another observation made is that PSRK simulation overpredicts all bubblepoint curves. The deviation between the PSRK and experimental bubblepoint is shown in table 5.1.

Table 5.1: Validation PSRK EOS with experimental data range

Liquid crystal used	Absolute pressure difference [MPa]	Absolute deviation from experiment [%]
5CB[1]	0.12-0.56	25.2-63.4
7OCB[1]	0.47-0.78	58.4-83.0
2,3-BCH[3]	0.03-0.13	4.7-14.6
3,4-BCH[3]	0.15-0.39	16.6-32.5
HOBAB[1]	0.08-0.40	7.9-28.2
PCH-type[2]	0.15-0.39	33.3-54.9

[1]biphenyl based structure.

[2]cyclohexylbenzene based structure.

[3]bicyclohexyl based structure.

The PSRK EOS predicts 2,3-BCH bubblepoint line most accurate, between 4.7-14.6 % deviation, the least accurate prediction of bubblepoint line is with simulation of 7OCB, with an average deviation of 58.4-83.0 %. In figures 5.7 and 5.8 the bubblepoint curve order respectively between the experimental values and the PSRK simulation is compared. The UNIFAC parameters are fitted at 298 K, resulting in a more accurate prediction of the bubblepoint curve at lower temperature.
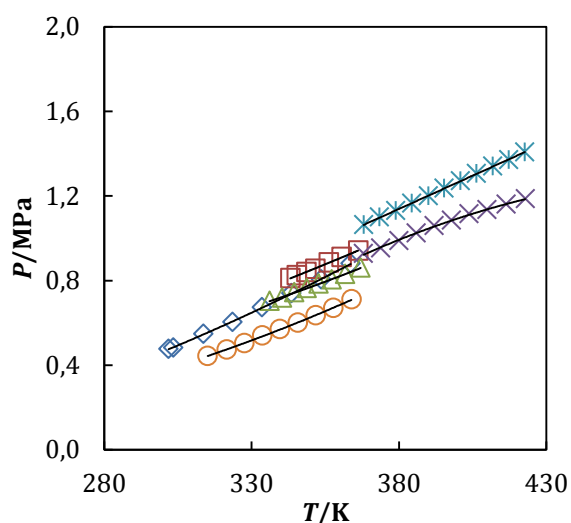
Figure 5.7: *P,T*-diagram of experimental data Liquid Crystals with 1 mass % CO_2. Description of symbols used: (blue ◇) 5CB, (red □) 7OCB, (green △) 2,3-BCH, (purple ✕) 3,4-BCH, (light blue ✳) HOBAB, (orange ○) PCH-type.
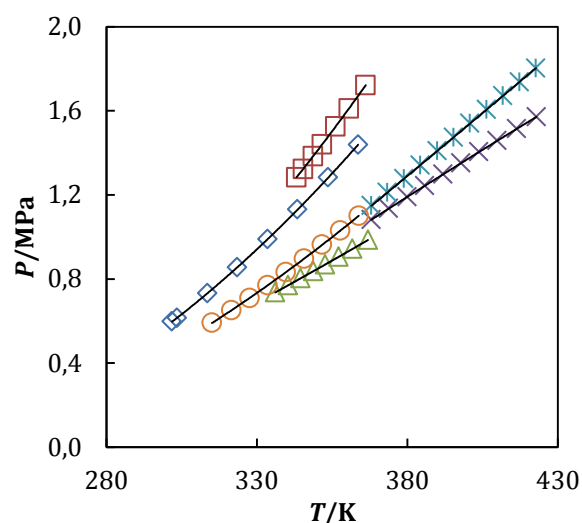
Figure 5.8: *P,T*-diagram of PSRK simulated Liquid Crystals with 1 mass % CO_2. Description of symbols used: (blue ◇) 5CB, (red □) 7OCB, (green △) 2,3-BCH, (purple ✕) 3,4-BCH, (light blue ✳) HOBAB, (orange ○) PCH-type.

The bubblepoint curve order of biphenyl structures; 5CB, 7OCB and HOBAB, is different in the PSRK simulation. 5CB and 7OCB have the same bubblepoint curve order, HOBAB is predicted lower than both 5CB and 7OCB while the experimental data proofs otherwise. The bubblepoint curve order of bicyclohexyl structures; 2,3-BCH and 3,4-BCH, is maintained the same as found in the experiments. The bubblepoint curve of PCH-type is simulated above those of 2,3-BCH and 3,4-BCH, while in the experiments the opposite is found.

5.2 Conclusion on PSRK EOS validation with Cailletet experiments

In this chapter the experimental bubblepoint line is used to validate the PSRK EOS with the Cailletet measurement (Chapter 4). The PSRK EOS predicts the bubblepoint line of binary mixtures of CO_2 with 2,3-BCH and HOBAB most accurately (see table 5.1), respectively on average 10.1 % and 18.8 % deviation over the whole temperature range and 4.7 % and 7.9 % at the lowest measured temperature.

Observed from the literature is that phenyl structures with acetate are underpredicted with the PSRK EOS, while the PSRK EOS overpredicts the bubblepoint curve of the Cailletet experiments. Also all bicyclohexyl structures found in literature are underpredicted with the PSRK EOS, while the PSRK EOS overpredicts the bubblepoint curve of the Cailletet experiments

From the PSRK simulation of the Cailletet experiments it can be concluded that all measured LC bubblepoint curves are overpredicted by the PSRK EOS. Nevertheless apolar LCs, like 2,3-BCH and 3,4-BCH, are simulated more accurately than polar LCs (except for HOBAB).

Besides HOBAB, all other LCs with a cyano group is predicted worse than the ones that do not include a cyano group. The prediction that larger molecules are modelled less accurate with the PSRK holds for 2,3-BCH and 3,4-BCH, when comparing HOBAB and 7OCB are similar in molecular size but have a large difference in accuracy. When comparing the molecular sizes of 7OCB with 5CB, it can be concluded that the smaller 5CB is modelled more accurately with the PSRK EOS. In the PSRK EOS validation of the experimental data from literature it is found that the acetonitrile (table 2.2) also is overpredicted at low concentration. From this it can be expected that LC that include a cyano or nitrile group decreases the accuracy of the PSRK EOS at low CO_2 concentrations.

The PSRK simulation bubblepoint curve order of biphenyl structures differs from the experimentally found one. Main cause of the difference found is the large overprediction with 5CB and 7OCB while HOBAB is simulated rather accurate. The order of the bicyclohexyl structures, 2,3-BCH and 3,4-BCH, remains the same in the PSRK simulation as in the experimentally found values. PCH-type bubblepoint curve is simulated in the same order with 5CB and 7OCB due to the relative equal overpredicted deviation, while the others are simulated more accurate.

6.0 Conclusion & Recommendations

This report focusses on two main elements of CO_2 capture with liquid crystals from syngas, namely; the solubility of CO_2 and H_2, and the usability of the PSRK EOS for simulating these binary mixtures.

The chemicals from literature and the bubblepoint curves from the Cailletet experiments are simulated with the PSRK EOS exposing the strengths and weaknesses of this EOS for the purpose of modelling binary mixtures of LC with CO_2 or H_2. The PSRK EOS uses the UNIFAC group contribution to predict phase behaviour, and uses the critical points of the LCs for this prediction. UNIFAC groups are fitted to actual VLE data at 298 K, which immediately implicates high temperature bubblepoint curve simulation. Another weakness from the UNIFAC group contribution method is that it relates all groups included in the mixture, resulting in less accuracy for larger molecular structures. The PSRK overpredicts all Cailletet measured bubblepoint curves while in the simulation of the literature bubblepoint curves are mostly underpredicted (except most benzene structures). Deviations from experimental data from literature data is large for binary mixtures including H_2, also the acetate structures from literature are simulated inaccurate. Most accurately simulated are the bicyclohexyl based structures.

From the ideal selectivity it can be concluded that a ketone group, ester group or ether group is predicting an increase in solubility of CO_2 and a decrease of H_2. A similarity in these three groups is the presence of an oxygen molecule next to the ring structure. Highest selectivity is found in the ketone- and ester group, which both include a double bonded oxygen molecule next to the carbon chain. The inaccuracy of the PSRK to simulate binary mixtures that include H_2 results in a less reliable prediction of phase behaviour and thus selectivity. The ester group is predicted to have a high selectivity for CO_2, nevertheless the acetate structures from literature are underpredicted with a large deviation and moreover the H_2 prediction is inaccurate. This results in a questionable high selectivity of groups that include oxygen molecules next to the ring structure.

Highest solubility of CO_2 is found in PCH-type with the Cailletet experiments, the lowest for HOBAB. However, from PCH-type molecule solid to isotropic liquid phase transition line was measured above the temperature of the nematic to isotropic phase transition. This indicates that the measured nematic + isotropic two-phase area, the nematic phase and part of the three-phase curve is in a metastable zone. From the measurable solid to isotropic liquid phase transition line it can be concluded that the capacity of PCH-type is low. Second highest solubility of CO_2 is in 7OCB, which consist of a biphenyl structure including an ether group next to ring structure. In the phase transition Cailletet experiment of LC with H_2 a pressure decrease over time in bubblepoint curve is measured. The cause of this is not yet known and therefore needs more investigation.

From the PSRK simulation it is found that bicyclohexyl based structures have the highest CO_2 solubility, cyclohexylbenzene intermediate and biphenyl the lowest solubility of CO_2. In the experiments the estimated solubility the highest CO_2 solubility if found for cyclohexylbenzene, an intermediate solubility for biphenyl and lowest for bicyclohexyl. The difference between last two structures are less distinct, opposite to that is only one PCH-type is measured.

Differences found between the PSRK simulation and the experimental results can be explained by the accuracy found in the PRSK simulation with predicting experimental bubblepoint curves. High accuracy is found for bicyclohexyl structures, with only a small overprediction, while those of cyclohexylbenzene and biphenyl are overpredicted with larger deviation from the experimental values.

The proposed CO_2 capture process is based on continuous absorption of CO_2; therefore highly viscous fluids are not employable. Smectic phase viscosity is relatively high and for that 2,3-BCH and 3,4-BCH are not usable in this application.

It is indicated from the solubility prediction and the experiments that the polarity change resulting from the addition of an oxygen molecule increases the solubility of CO_2 and decreases solubility of H_2 (simulation). Before the actual selectivity can be determined, the problems with the experimental H_2 measurements need to be solved. Research should continue focussing on LC structures that include oxygen molecules.

References

[1] Bernstein, L., Bosch, P., Canziani O., Climate Change 2007: Synthesis Report, Intergovernmental Panel on Climate Change (IPCC), 2007.

[2] Metz. B., Davidson O., De Coninck, H., Loos, M., Meyer, L., IPCC Special Report on Carbon Dioxide Capture and Storage, 2005, Cambridge University press.

[3] D'alessandro, D.M., Smit, B., Long, J.R., Carbon Dioxide Capture: Prospects for New Materials, 2010, Angewandte Chemie International edition, 6058-6082.

[4] De Groen, M., Vlught, T.J.H., De Loos, T.W., Phase Behaviour of Liquid Crystals with CO_2, 2012, The Journal of Physical Chemistry, 9101-9106.

[5] Smith, J.M., Van Ness, H.C., Abbott, M.M., 'Introduction to Chemical Engineering Thermodynamics', 2005, McGraw-Hill international edition, 7th edition.

[6] Span, R., Wagner, W., 'A New Equation of State for Carbon Dioxide Covering the Fluid Region from the Triple-Point Temperature to 1100 K at Pressures up to 800 MPa', 1994, The Journal of Physical Chemistry, vol. 25, no.6, 1996.

[7] Grandia, L., De Loos, Th. W., 'Heterogene evenwichten', 1995, Laboratorium voor Toegepaste Thermodynamica en Fasenleer.

[8] Singh S., Phase transitions in liquid crystals, 1999, Physics Reports 324 (2000) 107-269, Elsevier.

[9] Mullin, J.W., Crystallization, 2001, Butterworth Heinemann, 4th edition.

[10] P. Yurkanis Bruice, Organic Chemistry, 2006, Prentice Hall, 4th edition.

[11] McMurry, J., Ballanine, D.S., Hoeger, C.A., Peterson, V.E., Fundamentals of General, Organic, and Biological Chemistry, Pearson , 7th edition.

[12] Martienssen, W., Warlimont, H., Springer Handbook of Condensed Matter and Materials data, Springer Berlin Heidelberg, 2005.

[13] Holderbaum, T., Gmehling, J., PSRK: A Group Contribution Equation of State Based on UNIFAC, Elsevier, Fluid Phase equilibria, 70 (1991) 251-265.

[14] Maurer, G., Dieter, W., Schmelzer, J., Bamberger, A., 'High pressure vapour-liquid equilibria in binary mixtures of carbon dioxide and benzene compounds: experimental data for mixtures with ethylbenzene, isopropylbenzene, 1,2,4-trimethylbenzene, 1,3,5-trimethylbenzene, ethenylbenzene and isopropenylbenzene, and their correlation with the generalized Bender and Skjold-Jorgensen's group contribution equation of state', 1994, Fluid Phase Equilibria, vol. 97, 167-189.

[15] Enick, R.M., Bendale, P.G., 'Use of carbon dioxide to shift benzene/acetonitrile and benzene/cyclohexane azeotropes', 1994, Fluid Phase Equilibria, vol. 94, 227-253.

[16] Peters, C.J., Van Nielen, R.M., Schenk, A.P., Kordikowski, A., 'Volume Expansions and Vapor-Liquid Equilibria of Binary Mixtures of a Variety of Polar Solvents and Certain Near-Critical Solvents, 1995, The Journal of Supercritical Fluids, vol. 8, 205-216.

[17] de Swaan Arons, J., de Loos, Th. W., Jager, M.D., van Roermund, J.C., Stevens, R.M.M., 'High-pressure vapour-liquid equilibria in the systems carbon dioxide + 2-butanol, +2-butyl acetate, +vinyl acetate and calculations with three EOS methods', 1997, Fluid Phase Equilibria, vol. 138, 159-178.

[18] Richon, D., Laugier, S., 'High-Pressure Vapor-Liquid Equilibria of Two Binary Systems: Carbon Dioxide + Cyclohexanol and Carbon Dioxide + Cyclohexanone', 1997, J. Chem. Eng. Data, vol. 42, 155-159.

[19] Chen, C., Chang, C., Lin, H., 'Solubilities of Carbon Dioxide and Nitrous Oxide in Cyclohexanone, Toluene, and N,N-Dimethylformamide at Elevated Pressures', 1995, J. Chem. Eng. Data, vol. 40, 850-855.

[20] Maurer, G., Bamberger, A., 'High-Pressure Vapor-Liquid Equilibria in Binary Mixtures of Carbon Dioxide and Aromatic Hydrocarbons: Experimental Data and Correlation of CO_2 + Acetophenone, CO_2 + 1-Chloronaphthalene, CO_2 + Methyl Benzoate and CO_2 + n-Propylbenzene', 1994, The Journal of Supercritical Fluids, vol. 7, 115-127.

[21] Soave, G.S., Rasmussen, P., Persson, O., Jonasson, A., 'Vapor-liquid equilibria of systems containing acetic acid and gaseous components, Measurements and calculations by a cubic equation of state', 1998, Fluid Phase Equilibria, vol. 152, 67-94.

[22] Pruden, B. B., Peramanu, S., 'Solubility Study for the Purification of Hydrogen from High Pressure Hydrocracker Off-gas by an Absorption-Stripping Process', 1997, The Canadian journal of Chemical Engineering, vol. 75, 535-543.

[23] Gasem, K.A.M., Robinson, R.L., Shaver, R.D., 'An automated apparatus for equilibrium phase compositions, densities, and interfacial tensions: data for carbon dioxide + decane', 2001, Fluid Phase Equilibria, vol. 179, 43-66.

[24] Peters, C.J., Florusse, L.J., Vega, L.F., Pamies, J.C., Meijer, H., 'Solubility of Hydrogen in Heavy n-Alkanes: Experiments and SAFT Modeling',2003, AIChE Journal, vol. 49, no. 12, 3260-3269.

[25] Zhang, D., Wang, L., Sheng, W., Lu, B.C.Y., 'Experimental determination of P-x, L=G Critical Locus and UCEP for Biphenyl-CO_2 Mixtures, 1991, The Canadian journal of Chemical Engineering, vol. 69, 1352-1356.

[26] Qian, J. W., Jaubert, J.N., 'Phase equilibria in hydrogen-containing binary systems modeled with the Peng-Robinson equation of state and temperature-dependent binary interaction parameter calculated through a group-contribution method', 2013, The Journal of Supercritical Fluids', vol. 75, 58-71.

[27] Holderbaum T., Gmehling J., Fluid Phase Equilib. 1991, 70, 251-265.

[28] Holderbaum T., Gmehling J., Chem.Ing.Tech. 1991, 63(1), 57-59.

[29] Gmehling J., Fluid Phase Equilib. 1995, 107, 1-29.

[30] Fischer K., Gmehling J., Fluid Phase Equilib. 1996, 121, 185-206.

[31] Gmehling J., Li J., Fischer K., Fluid Phase Equilib. 1997, 141, 113-127.

[32] Li J., Fischer K., Gmehling J., Fluid Phase Equilib. 1998, 143, 71-82.

[33] Horstmann S., Fischer K., Gmehling J., Fluid Phase Equilib. 2000, 167, 173-186.

[34] Horstmann S., Fischer K., Gmehling J., Kolar P., J.Chem.Thermodyn. 2000, 32, 451-464.

[35] Guilbot P., Theveneau P., Baba-Ahmed A., Horstmann S., Fischer K., Richon D., Fluid Phase Equilib. 2000, 170, 193-202.

[36] Chem J., Fischer K., Gmehling J., Fluid Phase Equilib. 2002, 200, 411-429.

[37] Li M., Wang L., Gmehling J., Chin.J.Chem.Eng. 2004, 12(3), 454-457.

[38] Horstmann S., Fischer K., Gmehling J., J.Chem.Eng. Commun. 2005, 192, 336-350.

[39] Horstmann S., Jabloniec A., Krafczyk J., Fischer K., Gmehling J., Fluid Phase Equilib. 2005, 227(2), 157-164.

[40] Srivastava R. D., McIlvried H., Plasynski, S., Four, T., Figueroa J.D., 'Advances in CO_2 capture technology – The U.S. Department of Energy's Carbon Sequestration Program', 2008, Internation Journal of Greenhouse Gas Control, 9-20.

[41] Poling, B.E., Prausnitz, J.M., O'Connell, J.P., 'The Properties of Gases and Liquids', 2007, McGraw-Hill international edition, 5th edition.

[42] Tsuji, K., Sorai, M., Suga, H., Seki, S., Heat capacity and thermodynamic properties of p'-substituted p-n-hexyloxybenzylideneaniline. 1. p-n-hexyloxybenzylideneamino-p'-benzonitrile (HBAB), Mol. Cryst. Liq. Cryst., 1979, 55, 71-87.

[43] Ramdin, M., de Loos, Th. W., Vlugt, T.J.H, 'State-of-the-Art of CO_2 Capture with Ionic Liquids', 2012, Ind. Eng. Chem. Res., 51 (24), 8149-8177.

[44] De Groen, M., personal communication, May 15, 2013.

[45] Raeissi, S., Florusse, L.J., Peters, C.J., 'Hydrogen Solubilities in the IUPAC Ionic Liquid 1-Hexyl-3-methylimidazolium Bis(Trifluoromethylsulfonyl)lmide', 2011, J. Chem. Eng. Data, 56,1105-1107.

Appendix A

Experimental method: Cailletet setup

The Cailletet setup is used to visually measure the phase equilibrium lines of the pure component or mixture of components. First a filling of the desired component(s) is made and then this filling is positioned in the Cailletet setup.

The mixture of LC and gas, including a magnetic ball for stirring is placed in a thick walled Pyrex glass tube (Cailletet tube). The amount of LC is carefully weighed (typically between 100 and 200 mg, accuracy is 0.1 mg) of which, taking in account the filling pressure and temperature, the amount of gas added is determined. Before adding the gas the LC must be degassed, the Cailletet tube is connected to the gas filling station creating a vacuum in the tube from a vacuum pump. The LC is then heated or cooled, depending on the prior phase change. In the isotropic phase the gaseous impurities will escape and are released from the tube by the vacuum. This is repeated until the pressure of the degassed LC in the Cailletet tube is at vacuum. When the LC is degassed the gas can be added to the sample in the Cailletet tube. The partial pressure of gas is calculated from the virial equation of state to determine the amount of gas which needs to be added in order to reach the correct sample ratio between gas and LC. The virial equation (Berlin form) of state used:

$$Z = \frac{p \cdot v}{R \cdot T} = 1 + B'(T)p + C'(T)p^2 + D'(T)p^3 + \ldots$$

$$B' = \frac{B}{RT}$$

At the calculated partial pressure the valve of gas at the gas filling is closed and N_2 gas is used to push the mercury into the Cailletet tube closing the sample. The partial pressure of the filled CO_2 is measured from which the actual amount of gas added can be calculated.

Corrections on experimental data

The following corrections need to be made on the measured pressure

1) Atmospheric pressure correction: the dead weight gauge is at atmospheric pressure in the laboratory.

2) Gravity correction for laboratory latitude (52°):

$$P_{1,corrected} = P_{measured} \cdot (9.81247/9.80665) = P_{measured} \cdot 1.00059$$

3) Temperature correction for the influence of the temperature $t(\degree C)$ on the piston area:

$$P_{2,corrected} = P_1 \cdot (1 - (t - 20) \cdot 2.3 \cdot 10^{-5})$$

4) Mercury column correction for the pressure transmitted by the fluid in the Cailletet column:

$$\rho_{Hg}(T) = -12.281 \cdot T + 13595$$
$$P_{Hg} = \rho_{Hg}(T) \cdot g \cdot \Delta h$$

The actual experimental pressure becomes: $P_{experiment} = P_2 + P_{atm} - P_{Hg}$

Appendix B

Carbon dioxide bubblepoint curve

To test the Cailletet equipment and the purity of the CO_2, a phase diagram of CO_2 is made and verified with an adequate EOS. The experimental VLE and the VLE of the EOS are shown in table B.1 plotted in a CO_2 phase diagram (figure 5.1). In the Cailletet apparatus the VLE points of CO_2 (Linde gas, purity 4.5) are determined (table B.1).

Table B.1: EOS and laboratory data

CO_2 (EOS)		CO_2 (Experiment)		ΔP
P/MPa	T/K	P/MPa	T/K	P/MPa
L↔G		L↔G		
3.98	278.26	3.98	278.26	0.002
4.51	283.20	4.51	283.20	0.000
5.09	288.20	5.09	288.20	-0.001
5.73	293.19	5.73	293.19	0.005
6.45	298.25	6.44	298.25	0.004
7.23	303.22	7.22	303.22	0.005
7.38[1]	304.13[2]	7.38[1]	304.13[2]	-0.004

[1]Critical pressure
[2]Critical temperature

Comparing the experimental results with an adequate EOS [6] will show if the experimental values for the bubblepoint curve are in the accuracy range of $u(P)=\pm 0.005$ MPa. The EOS is based on the sublimation pressure of CO_2 and is fitted on the vapor-liquid equilibrium line. The EOS formula used for the CO_2 bubblepoint curve can be written as:

$$\ln\left(\frac{P}{P_c}\right) = \frac{T_c}{T} \cdot \left[\sum_{i=1}^{4} a_i \cdot \left(1 - \frac{T}{T_c}\right)^{t_i}\right]$$

The constants in the EOS used for the bubblepoint curve can be found in the paper of Span, R., Wagner, W. [6]. In table B.1 the deviation shows that all Cailletet measurements are between accuracy limits, so the CO_2 filled satisfied the general EOS in terms of bubblepoint curve.

Appendix C

Laboratory data Cailletet measurements

Table C.1   **Table C.2**

3,4-BCH + CO$_2$	
P/MPa	T/K
I↔G+I	
0.927	367.98
0.953	373.80
0.988	379.93
1.023	385.81
1.059	391.88
1.084	397.78
1.114	403.79
1.135	409.83
1.160	416.31
1.185	422.85
Sm+G↔I+G	
0.439	366.60
0.568	366.11
0.678	365.63
0.792	365.10
0.907	364.59
Sm+I↔I	
1.057	364.04
2.058	364.58
3.058	365.27
4.059	365.89
5.060	366.51
6.060	366.93
7.061	367.46
8.061	368.08

HOBAB + CO$_2$			
P/MPa	T/K	P/MPa	T/K
I↔G+I		N↔N+I	
1.064	368.01	1.355	366.00
1.099	373.38	2.055	366.30
1.129	378.92	3.056	366.72
1.165	384.33	4.056	367.10
1.200	389.93	5.057	367.50
1.235	395.33	6.057	367.91
1.271	400.83	7.058	368.31
1.306	406.28	8.059	368.71
1.341	411.75		
1.371	417.22		
1.407	422.70		
N+I↔I		N↔N+G	
1.156	366.65	0.913	328.92
2.056	366.98	0.938	332.76
3.057	367.38	0.969	336.83
4.057	367.78	0.999	340.80
5.058	368.19	1.023	344.81
6.059	368.57	1.053	348.90
7.059	368.98	1.073	352.86
8.060	369.39	1.088	356.82
		1.099	360.85
		1.099	364.75
Sm+N↔N			
1.153	326.73		
2.054	327.12		
3.054	327.53		
4.055	327.94		
5.055	328.33		
6.056	328.71		
7.056	329.12		
8.057	329.52		
N+G↔I+G			
0.560	369.25		
0.629	368.95		
0.685	368.66		
0.734	368.41		
0.779	368.17		
0.824	367.89		
0.849	367.74		
0.909	367.44		
1.029	366.80		

Table C.3			Table C.4			Table C.5	
5CB + CO_2			**7OCB + CO_2**			**2,3-BCH + CO_2**	
P/MPa	T/K		P/MPa	T/K		P/MPa	T/K
I↔G+I			I↔G+I			I↔G+I	
0.477	301.81		0.810	343.14		0.703	336.10
0.482	303.48		0.825	345.36		0.719	340.35
0.547	313.59		0.840	348.64		0.744	344.48
0.603	323.49		0.855	351.67		0.764	348.74
0.673	333.53		0.885	356.15		0.784	352.76
0.739	343.45		0.911	360.53		0.805	357.19
0.804	353.65		0.941	366.14		0.830	361.78
0.880	363.63					0.860	366.96
N+I↔I			N+I↔I			Sm+I↔I	
0.556	301.55		0.910	342.85		0.754	335.51
1.157	301.80		1.910	343.18		1.553	335.87
2.057	302.15		2.911	343.54		2.553	336.33
3.058	302.55		3.912	343.89		3.554	336.79
4.058	302.94		4.912	344.23		4.554	337.23
5.059	303.34		5.912	344.58		5.555	337.67
6.060	303.73		6.913	344.93		6.556	338.12
7.060	304.14		7.914	345.26		7.556	338.59
8.061	304.51					8.557	339.03
N↔N+I			N↔N+I			Sm+G↔I+G	
0.555	301.07		0.910	342.73		0.441	337.15
1.155	301.30		1.910	343.09		0.511	336.76
2.056	301.65		2.911	343.44		0.620	336.14
3.057	302.05		3.912	343.79			
4.058	302.44		4.912	344.14			
5.058	302.83		5.913	344.50			
6.059	303.22		6.913	344.86			
7.060	303.63		7.914	345.19			
8.061	304.02						
N+I↔N+G			N+I↔N+G				
0.490	301.15		0.835	342.74			
0.490	301.32						
N↔N+G			N↔N+G				
0.414	278.77		0.784	326.46			
0.434	282.51		0.804	329.52			
0.449	286.56		0.819	332.59			
0.469	290.54		0.834	335.39			
0.485	294.42		0.845	338.54			
0.495	298.50		0.845	341.57			
N+G↔I+G			N+G↔I+G				
0.272	304.07		0.308	345.75			
0.296	303.77		0.412	345.20			
0.346	303.18		0.521	344.55			
0.395	302.52		0.625	343.96			
0.450	301.88		0.695	343.59			

Table C.6

PCH-type + CO_2	
P/MPa	*T*/K
I↔G+I	
0.443	315.07
0.474	321.58
0.504	327.57
0.539	333.62
0.569	339.58
0.600	345.67
0.635	351.69
0.670	357.72
0.710	363.87
N+I↔I	
0.658	314.01
1.558	314.45
2.559	314.92
3.560	315.40
4.560	315.87
5.560	316.35
6.560	316.83
7.561	317.31
8.562	317.78
N↔N+I	
0.657	313.04
1.557	313.48
2.558	313.96
3.558	314.43
4.559	314.90
5.559	315.39
6.560	315.86
7.561	316.34
8.561	316.81
N+I↔N+G	
0.486	313.30
0.451	313.78
N↔N+G	
0.491	308.53
0.491	310.00
0.491	311.52
0.491	312.75
N+G↔I+G	
0.426	314.14
0.381	314.79
0.331	315.36
0.287	315.96

Table C.7

2,3-BCH + H_2	
P/MPa	*T*/K
I↔G+I	
7.889	349.15
7.604	357.05
7.334	364.54
8.198	341.17
7.953	346.27
7.673	353.34
7.158	360.67

Table C.8

PCH-type + H_2	
P/MPa	*T*/K
I↔G+I	
6.849	334.55
6.574	341.48
6.344	347.52
7.383	323.92
5.819	362.71

Table C.8

7OCB + H_2	
P/MPa	*T*/K
I↔G+I	
7.115	356.84
7.775	356.28
7.780	356.44

Appendix D

Henry coefficients

Table D.1

5CB + CO_2				
P/MPa	T/K	ϕ_{CO_2}/−	f_{CO_2}/MPa	H/MPa
I↔G+I				
0.477	301.81	0.97758	0.46597	8.474
0.482	303.48	0.97776	0.47101	8.564
0.547	313.59	0.97737	0.53480	9.724
0.603	323.49	0.97754	0.58931	10.715
0.673	333.53	0.97739	0.65809	11.965
0.739	343.45	0.97755	0.72219	13.131
0.804	353.65	0.97790	0.78648	14.300
0.880	363.63	0.97806	0.86041	15.644

Table D.2

7OCB + CO_2				
P/MPa	T/K	ϕ_{CO_2}/−	f_{CO_2}/MPa	H/MPa
I↔G+I				
0.810	343.14	0.97532	0.78992	12.538
0.825	345.36	0.97542	0.80464	12.772
0.840	348.64	0.97576	0.81977	13.012
0.855	351.67	0.97605	0.83476	13.250
0.885	356.15	0.97627	0.86443	13.721
0.911	360.53	0.97661	0.88922	14.115
0.941	366.14	0.97710	0.91934	14.593

Table D.3

PCH-type + CO_2				
P/MPa	T/K	ϕ_{CO_2}/−	f_{CO_2}/MPa	H/MPa
I↔G+I				
0.443	315.07	0.98194	0.43520	8.704
0.474	321.58	0.98199	0.46498	9.300
0.504	327.57	0.98200	0.49473	9.895
0.539	333.62	0.98189	0.52933	10.587
0.569	339.58	0.98200	0.55912	11.182
0.600	345.67	0.98216	0.58892	11.778
0.635	351.69	0.98220	0.62360	12.472
0.670	357.72	0.98228	0.65829	13.166
0.710	363.87	0.98230	0.69789	13.958

Table D.4

3,4-BCH + CO_2				
P/MPa	T/K	ϕ_{CO_2}/−	f_{CO_2}/MPa	H/MPa
I↔G+I				
0.927	367.98	0.97781	0.90689	15.910
0.953	373.80	0.97843	0.93220	16.354
0.988	379.93	0.97889	0.96721	16.969
1.023	385.81	0.97930	1.00217	17.582
1.059	391.88	0.97976	1.03724	18.197
1.084	397.78	0.98038	1.06270	18.644
1.114	403.79	0.98091	1.09303	19.176
1.135	409.83	0.98160	1.11383	19.541
1.160	416.31	0.98227	1.13932	19.988
1.185	422.85	0.98292	1.16507	20.440

Table D.5

HOBAB + CO_2				
P/MPa	T/K	ϕ_{CO_2}/−	f_{CO_2}/MPa	H/MPa
I↔G+I				
1.064	368.005	0.97458	1.03683	16.458
1.099	373.381	0.97504	1.07170	17.011
1.129	378.922	0.97566	1.10192	17.491
1.165	384.328	0.97614	1.13689	18.046
1.200	389.932	0.97667	1.17197	18.603
1.235	395.325	0.97715	1.20701	19.159
1.271	400.829	0.97766	1.24212	19.716
1.306	406.277	0.97816	1.27723	20.273
1.341	411.749	0.97866	1.31240	20.832
1.371	417.220	0.97923	1.34282	21.315
1.407	422.698	0.97973	1.37807	21.874

Table D.6

2,3-BCH + CO_2				
P/MPa	T/K	ϕ_{CO_2}/−	f_{CO_2}/MPa	H/MPa
I↔G+I				
0.703	336.100	0.97699	0.68725	13.216
0.719	340.351	0.97747	0.70254	13.510
0.744	344.479	0.97762	0.72730	13.987
0.764	348.742	0.97796	0.74731	14.371
0.784	352.755	0.97826	0.76730	14.756
0.805	357.192	0.97864	0.78738	15.142
0.830	361.775	0.97892	0.81230	15.621
0.860	366.955	0.97922	0.84217	16.196

Appendix E

Modeling of different LC structures with CO_2 and H_2 in Aspen Plus

Table E.1: A +CO_2

Molecular structure	Mole fraction −	Pressure P/MPa	Temperature T/K	Fugacity coefficient ϕ_{CO_2}/−	Fugacity f_{CO_2} /MPa	Henry coefficient H/MPa
A1	0.01	0.111	298	0.99454	0.1107	11.1
	0.01	0.165	323	0.99380	0.1638	16.4
	0.01	0.226	348	0.99341	0.2249	22.5
	0.01	0.292	373	0.99331	0.2903	29.0
	0.01	0.359	398	0.99348	0.3565	35.7
A2	0.01	0.093	298	0.99543	0.0927	9.3
	0.01	0.130	323	0.99512	0.1294	12.9
	0.01	0.171	348	0.99501	0.1700	17.0
	0.01	0.214	373	0.99510	0.2126	21.3
	0.01	0.257	398	0.99533	0.2558	25.6
A3	0.01	0.093	298	0.99543	0.0929	9.3
	0.01	0.124	323	0.99534	0.1231	12.3
	0.01	0.156	348	0.99545	0.1556	15.6
	0.01	0.190	373	0.99565	0.1891	18.9
	0.01	0.224	398	0.99593	0.2234	22.3

Table E.2: AB1 + CO_2

Molecular structure	Mole fraction −	Pressure P/MPa	Temperature T/K	Fugacity coefficient ϕ_{CO_2}/−	Fugacity f_{CO_2} /MPa	Henry coefficient H/MPa
A1B1 n=2	0.01	0.104	298	0.99489	0.1037	10.4
	0.01	0.154	323	0.99422	0.1529	15.3
	0.01	0.211	348	0.99385	0.2095	21.0
	0.01	0.272	373	0.99377	0.2704	27.0
	0.01	0.334	398	0.99394	0.3323	33.2
A2B1 n=2	0.01	0.090	298	0.99557	0.0893	8.9
	0.01	0.127	323	0.99523	0.1263	12.6
	0.01	0.169	348	0.99507	0.1678	16.8
	0.01	0.213	373	0.99512	0.2119	21.2
	0.01	0.258	398	0.99531	0.2567	25.7
A3B1 n=2	0.01	0.084	298	0.99587	0.0841	8.4
	0.01	0.115	323	0.99568	0.1146	11.5
	0.01	0.149	348	0.99565	0.1480	14.8
	0.01	0.184	373	0.99578	0.1828	18.3
	0.01	0.219	398	0.99602	0.2180	21.8

Table E.3: AB1 + CO₂

Molecular structure	Mole fraction −	Pressure P/MPa	Temperature T/K	Fugacity coefficient ϕ_{CO_2}/−	Fugacity f_{CO_2} /MPa	Henry coefficient H/MPa
A1B1	0.01	0.103	298	0.99493	0.1027	10.3
n=5	0.01	0.149	323	0.99441	0.1487	14.9
	0.01	0.202	348	0.99411	0.2012	20.1
	0.01	0.259	373	0.99407	0.2578	25.8
	0.01	0.317	398	0.99424	0.3155	31.5
A2B1	0.01	0.091	298	0.99552	0.0911	9.1
n=5	0.01	0.128	323	0.99519	0.1278	12.8
	0.01	0.170	348	0.99504	0.1688	16.9
	0.01	0.213	373	0.99512	0.2124	21.2
	0.01	0.258	398	0.99531	0.2566	25.7
A3B1	0.01	0.087	298	0.99572	0.0866	8.7
n=5	0.01	0.118	323	0.99557	0.1178	11.8
	0.01	0.153	348	0.99554	0.1521	15.2
	0.01	0.189	373	0.99567	0.1879	18.8
	0.01	0.225	398	0.99591	0.2238	22.4

Table E.4: AB2 + CO₂

Molecular structure	Mole fraction −	Pressure P/MPa	Temperature T/K	Fugacity coefficient ϕ_{CO_2}/−	Fugacity f_{CO_2} /MPa	Henry coefficient H/MPa
A1B2	0.01	0.123	298	0.99395	0.1219	12.2
	0.01	0.184	323	0.99309	0.1827	18.3
	0.01	0.256	348	0.99254	0.2541	25.4
	0.01	0.335	373	0.99233	0.3323	33.2
	0.01	0.416	398	0.99245	0.4132	41.3
A2B2	0.01	0.108	298	0.99469	0.1069	10.7
	0.01	0.152	323	0.99429	0.1515	15.1
	0.01	0.203	348	0.99408	0.2022	20.2
	0.01	0.258	373	0.99409	0.2567	25.7
	0.01	0.315	398	0.99428	0.3127	31.3
A3B2	0.01	0.093	298	0.99543	0.0924	9.2
	0.01	0.126	323	0.99527	0.1251	12.5
	0.01	0.162	348	0.99528	0.1616	16.2
	0.01	0.201	373	0.99539	0.2005	20.0
	0.01	0.241	398	0.99562	0.2402	24.0

Table E.5: AB3 + CO$_2$

Molecular structure	Mole fraction −	Pressure P/MPa	Temperature T/K	Fugacity coefficient $\phi_{CO_2}/-$	Fugacity f_{CO_2} /MPa	Henry coefficient H/MPa
A1B3	0.01	0.064	298	0.99685	0.0637	6.4
	0.01	0.098	323	0.99632	0.0976	9.8
	0.01	0.139	348	0.99595	0.1384	13.8
	0.01	0.185	373	0.99576	0.1839	18.4
	0.01	0.233	398	0.99577	0.2318	23.2
A2B3	0.01	0.061	298	0.99700	0.0609	6.1
	0.01	0.091	323	0.99658	0.0902	9.0
	0.01	0.125	348	0.99635	0.1244	12.4
	0.01	0.162	373	0.99629	0.1614	16.1
	0.01	0.200	398	0.99637	0.1994	19.9
A3B3	0.01	0.062	298	0.99695	0.0621	6.2
	0.01	0.089	323	0.99666	0.0890	8.9
	0.01	0.120	348	0.99650	0.1194	11.9
	0.01	0.152	373	0.99652	0.1514	15.1
	0.01	0.184	398	0.99666	0.1835	18.3

Table E.6: AB4 + CO$_2$

Molecular structure	Mole fraction −	Pressure P/MPa	Temperature T/K	Fugacity coefficient $\phi_{CO_2}/-$	Fugacity f_{CO_2} /MPa	Henry coefficient H/MPa
A1B4	0.01	0.091	298	0.99552	0.0903	9.0
	0.01	0.141	323	0.99471	0.1407	14.1
	0.01	0.203	348	0.99408	0.2015	20.2
	0.01	0.271	373	0.99379	0.2697	27.0
	0.01	0.343	398	0.99377	0.3412	34.1
A2B4	0.01	0.075	298	0.99631	0.0743	7.4
	0.01	0.111	323	0.99583	0.1104	11.0
	0.01	0.153	348	0.99554	0.1522	15.2
	0.01	0.199	373	0.99544	0.1976	19.8
	0.01	0.246	398	0.99553	0.2445	24.5
A3B4	0.01	0.068	298	0.99666	0.0679	6.8
	0.01	0.097	323	0.99636	0.0966	9.7
	0.01	0.129	348	0.99624	0.1288	12.9
	0.01	0.163	373	0.99626	0.1629	16.3
	0.01	0.198	398	0.99640	0.1975	19.8

Table E.7: AB5 + CO₂

Molecular structure	Mole fraction	Pressure	Temperature	Fugacity coefficient	Fugacity	Henry coefficient
	−	P/MPa	T/K	ϕ_{CO_2}/−	f_{CO_2} /MPa	H/MPa
A1B5	0.01	0.062	298	0.99695	0.0622	6.2
	0.01	0.087	323	0.99673	0.0872	8.7
	0.01	0.114	348	0.99667	0.1135	11.4
	0.01	0.140	373	0.99679	0.1395	13.9
	0.01	0.164	398	0.99702	0.1636	16.4
A2B5	0.01	0.056	298	0.99725	0.0560	5.6
	0.01	0.078	323	0.99707	0.0775	7.8
	0.01	0.100	348	0.99708	0.0999	10.0
	0.01	0.122	373	0.99720	0.1217	12.2
	0.01	0.142	398	0.99742	0.1417	14.2
A3B5	0.01	0.054	298	0.99734	0.0542	5.4
	0.01	0.074	323	0.99722	0.0741	7.4
	0.01	0.095	348	0.99723	0.0946	9.5
	0.01	0.115	373	0.99736	0.1142	11.4
	0.01	0.132	398	0.99760	0.1319	13.2

Table E.8: AB6 + CO₂

Molecular structure	Mole fraction	Pressure	Temperature	Fugacity coefficient	Fugacity	Henry coefficient
	−	P/MPa	T/K	ϕ_{CO_2}/−	f_{CO_2} /MPa	H/MPa
A1B6	0.01	0.089	298	0.99562	0.0884	8.8
	0.01	0.138	323	0.99482	0.1378	13.8
	0.01	0.199	348	0.99420	0.1978	19.8
	0.01	0.267	373	0.99388	0.2653	26.5
	0.01	0.339	398	0.99384	0.3367	33.7
A2B6	0.01	0.070	298	0.99656	0.0696	7.0
	0.01	0.105	323	0.99606	0.1042	10.4
	0.01	0.146	348	0.99574	0.1450	14.5
	0.01	0.191	373	0.99562	0.1902	19.0
	0.01	0.239	398	0.99566	0.2375	23.7
A3B6	0.01	0.061	298	0.99700	0.0606	6.1
	0.01	0.088	323	0.99669	0.0878	8.8
	0.01	0.120	348	0.99650	0.1192	11.9
	0.01	0.154	373	0.99647	0.1534	15.3
	0.01	0.189	398	0.99657	0.1888	18.9

Table E.9: AB7 + CO₂

Molecular structure	Mole fraction	Pressure	Temperature	Fugacity coefficient	Fugacity	Henry coefficient
	$-$	P/MPa	T/K	ϕ_{CO_2}/$-$	f_{CO_2} /MPa	H/MPa
A1B7	0.01	0.082	298	0.99597	0.0821	8.2
	0.01	0.132	323	0.99504	0.1317	13.2
	0.01	0.194	348	0.99434	0.1927	19.3
	0.01	0.263	373	0.99397	0.2618	26.2
	0.01	0.337	398	0.99388	0.3349	33.5
A2B7	0.01	0.058	298	0.99715	0.0583	5.8
	0.01	0.091	323	0.99658	0.0905	9.0
	0.01	0.130	348	0.99621	0.1292	12.9
	0.01	0.174	373	0.99601	0.1729	17.3
	0.01	0.221	398	0.99598	0.2196	22.0
A3B7	0.01	0.045	298	0.99764	0.0448	4.5
	0.01	0.069	323	0.99741	0.0690	6.9
	0.01	0.098	348	0.99714	0.0980	9.8
	0.01	0.131	373	0.99700	0.1305	13.1
	0.01	0.166	398	0.99698	0.1655	16.5

Table E.10: AB8 + CO₂

Molecular structure	Mole fraction	Pressure	Temperature	Fugacity coefficient	Fugacity	Henry coefficient
	$-$	P/MPa	T/K	ϕ_{CO_2}/$-$	f_{CO_2} /MPa	H/MPa
A1B8	0.01	0.099	298	0.99513	0.0983	9.8
	0.01	0.154	323	0.99422	0.1529	15.3
	0.01	0.221	348	0.99356	0.2193	21.9
	0.01	0.296	373	0.99322	0.2943	29.4
	0.01	0.376	398	0.99317	0.3738	37.4
A2B8	0.01	0.077	298	0.99621	0.0770	7.7
	0.01	0.116	323	0.99564	0.1155	11.6
	0.01	0.162	348	0.99528	0.1611	16.1
	0.01	0.213	373	0.99512	0.2119	21.2
	0.01	0.267	398	0.99515	0.2654	26.5
A3B8	0.01	0.062	298	0.99695	0.0623	6.2
	0.01	0.092	323	0.99654	0.0912	9.1
	0.01	0.126	348	0.99633	0.1251	12.5
	0.01	0.163	373	0.99626	0.1626	16.3
	0.01	0.203	398	0.99631	0.2021	20.2

Table E.11: AB9 + CO$_2$

Molecular structure	Mole fraction	Pressure	Temperature	Fugacity coefficient	Fugacity	Henry coefficient
	−	P/MPa	T/K	$\phi_{CO_2}/-$	f_{CO_2}/MPa	H/MPa
A1B9	0.01	0.107	298	0.99474	0.1062	10.6
	0.01	0.166	323	0.99377	0.1653	16.5
	0.01	0.239	348	0.99303	0.2377	23.8
	0.01	0.323	373	0.99260	0.3202	32.0
	0.01	0.412	398	0.99252	0.4085	40.9
A2B9	0.01	0.087	298	0.99572	0.0865	8.6
	0.01	0.129	323	0.99516	0.1288	12.9
	0.01	0.180	348	0.99475	0.1791	17.9
	0.01	0.236	373	0.99459	0.2352	23.5
	0.01	0.296	398	0.99462	0.2948	29.5
A3B9	0.01	0.080	298	0.99607	0.0792	7.9
	0.01	0.114	323	0.99572	0.1134	11.3
	0.01	0.154	348	0.99551	0.1529	15.3
	0.01	0.197	373	0.99548	0.1962	19.6
	0.01	0.243	398	0.99559	0.2416	24.2

Table E.12: A + H$_2$

Molecular structure	Mole fraction	Pressure	Temperature	Fugacity coefficient	Fugacity	Henry coefficient
	−	P/MPa	T/K	$\phi_{H_2}/-$	f_{H_2}/MPa	H/MPa
A1	0.01	6.774	298	1.0420	7.0587	705.9
	0.01	5.687	323	1.0332	5.8755	587.5
	0.01	4.841	348	1.0266	4.9703	497.0
	0.01	4.167	373	1.0216	4.2571	425.7
	0.01	3.618	398	1.0177	3.6821	368.2
A2	0.01	3.357	298	1.0206	3.4262	342.6
	0.01	3.000	323	1.0174	3.0521	305.2
	0.01	2.691	348	1.0147	2.7303	273.0
	0.01	2.417	373	1.0125	2.4471	244.7
	0.01	2.171	398	1.0106	2.1937	219.4
A3	0.01	2.582	298	1.0158	2.6224	262.2
	0.01	2.275	323	1.0132	2.3051	230.5
	0.01	2.026	348	1.0111	2.0485	204.8
	0.01	1.819	373	1.0094	1.8360	183.6
	0.01	1.644	398	1.0080	1.6568	165.7

Table E.13: AB1 + H$_2$

Molecular structure	Mole fraction	Pressure	Temperature	Fugacity coefficient	Fugacity	Henry coefficient
	$-$	P/MPa	T/K	$\phi_{H_2}/-$	f_{H_2}/MPa	H/MPa
A1B1	0.01	4.041	298	1.0249	4.1421	414.2
n=2	0.01	3.597	323	1.0209	3.6724	367.2
	0.01	3.216	348	1.0176	3.2728	327.3
	0.01	2.885	373	1.0149	2.9278	292.8
	0.01	2.593	398	1.0127	2.6262	262.6
A2B1	0.01	2.763	298	1.0169	2.8101	281.0
n=2	0.01	2.490	323	1.0144	2.5262	252.6
	0.01	2.253	348	1.0123	2.2811	228.1
	0.01	2.043	373	1.0105	2.0646	206.5
	0.01	1.853	398	1.0090	1.8701	187.0
A3B1	0.01	2.140	298	1.0131	2.1682	216.8
n=2	0.01	1.925	323	1.0111	1.9468	194.7
	0.01	1.743	348	1.0095	1.7593	175.9
	0.01	1.583	373	1.0082	1.5963	159.6
	0.01	1.441	398	1.0070	1.4514	145.1

Table E.14: AB1 + H$_2$

Molecular structure	Mole fraction	Pressure	Temperature	Fugacity coefficient	Fugacity	Henry coefficient
	$-$	P/MPa	T/K	$\phi_{H_2}/-$	f_{H_2}/MPa	H/MPa
A1B1	0.01	3.805	298	1.0234	3.8936	389.4
n=5	0.01	3.416	323	1.0198	3.4831	348.3
	0.01	3.080	348	1.0169	3.1316	313.2
	0.01	2.784	373	1.0144	2.8238	282.4
	0.01	2.519	398	1.0123	2.5505	255.0
A2B1	0.01	2.811	298	1.0172	2.8597	286.0
n=5	0.01	2.538	323	1.0147	2.5749	257.5
	0.01	2.302	348	1.0126	2.3309	233.1
	0.01	2.094	373	1.0108	2.1163	211.6
	0.01	1.906	398	1.0093	1.9238	192.4
A3B1	0.01	2.270	298	1.0139	2.3020	230.2
n=5	0.01	2.044	323	1.0118	2.0685	206.8
	0.01	1.853	348	1.0101	1.8720	187.2
	0.01	1.687	373	1.0087	1.7021	170.2
	0.01	1.540	398	1.0075	1.5515	155.2

Table E.15: AB2 + H₂

Molecular structure	Mole fraction	Pressure	Temperature	Fugacity coefficient	Fugacity	Henry coefficient
	−	P/MPa	T/K	ϕ_{H_2}/−	f_{H_2}/MPa	H/MPa
A1B2	0.01	10.129	298	1.0635	10.7722	1077.2
	0.01	8.623	323	1.0507	9.0601	906.0
	0.01	7.439	348	1.0412	7.7459	774.6
	0.01	6.484	373	1.0338	6.7030	670.3
	0.01	5.696	398	1.0280	5.8553	585.5
A2B2	0.01	6.017	298	1.0372	6.2406	624.1
	0.01	5.414	323	1.0316	5.5852	558.5
	0.01	4.898	348	1.0269	5.0293	502.9
	0.01	4.442	373	1.0230	4.5439	454.4
	0.01	4.030	398	1.0198	4.1100	411.0
A3B2	0.01	4.108	298	1.0253	4.2124	421.2
	0.01	3.708	323	1.0215	3.7882	378.8
	0.01	3.377	348	1.0185	3.4393	343.9
	0.01	3.094	373	1.0160	3.1432	314.3
	0.01	2.846	398	1.0139	2.8854	288.5

Table E.16: AB3 + H₂

Molecular structure	Mole fraction	Pressure	Temperature	Fugacity coefficient	Fugacity	Henry coefficient
	−	P/MPa	T/K	ϕ_{H_2}/−	f_{H_2}/MPa	H/MPa
A1B3	0.01	8.422	298	1.0525	8.8646	886.5
	0.01	7.192	323	1.0421	7.4943	749.4
	0.01	6.220	348	1.0343	6.4338	643.4
	0.01	5.434	373	1.0283	5.5880	558.8
	0.01	4.784	398	1.0235	4.8959	489.6
A2B3	0.01	4.903	298	1.0302	5.0506	505.1
	0.01	4.385	323	1.0255	4.4965	449.6
	0.01	3.940	348	1.0216	4.0253	402.5
	0.01	3.549	373	1.0184	3.6146	361.5
	0.01	3.199	398	1.0157	3.2494	324.9
A3B3	0.01	3.541	298	1.0217	3.6181	361.8
	0.01	3.182	323	1.0184	3.2402	324.0
	0.01	2.878	348	1.0157	2.9232	292.3
	0.01	2.614	373	1.0135	2.6492	264.9
	0.01	2.379	398	1.0116	2.4064	240.6

Table E.17: AB4 + H$_2$

Molecular structure	Mole fraction −	Pressure P/MPa	Temperature T/K	Fugacity coefficient ϕ_{H_2}/−	Fugacity f_{H_2}/MPa	Henry coefficient H/MPa
A1B4	0.01	3.477	298	1.0213	3.5507	355.1
	0.01	3.268	323	1.0189	3.3301	333.0
	0.01	3.056	348	1.0167	3.1075	310.7
	0.01	2.847	373	1.0147	2.8890	288.9
	0.01	2.644	398	1.0129	2.6782	267.8
A2B4	0.01	2.267	298	1.0139	2.2985	229.9
	0.01	2.117	323	1.0122	2.1432	214.3
	0.01	1.972	348	1.0108	1.9934	199.3
	0.01	1.831	373	1.0094	1.8487	184.9
	0.01	1.695	398	1.0083	1.7095	170.9
A3B4	0.01	1.637	298	1.0100	1.6534	165.3
	0.01	1.519	323	1.0088	1.5322	153.2
	0.01	1.409	348	1.0077	1.4199	142.0
	0.01	1.306	373	1.0067	1.3145	131.4
	0.01	1.208	398	1.0059	1.2148	121.5

Table E.18: AB5 + H$_2$

Molecular structure	Mole fraction −	Pressure P/MPa	Temperature T/K	Fugacity coefficient ϕ_{H_2}/−	Fugacity f_{H_2}/MPa	Henry coefficient H/MPa
A1B5	0.01	3.014	298	1.0185	3.0696	307.0
	0.01	2.840	323	1.0164	2.8870	288.7
	0.01	2.666	348	1.0146	2.7050	270.5
	0.01	2.494	373	1.0129	2.5264	252.6
	0.01	2.327	398	1.0114	2.3540	235.4
A2B5	0.01	2.213	298	1.0135	2.2429	224.3
	0.01	2.061	323	1.0119	2.0857	208.6
	0.01	1.916	348	1.0105	1.9357	193.6
	0.01	1.776	373	1.0092	1.7925	179.3
	0.01	1.643	398	1.0080	1.6560	165.6
A3B5	0.01	1.760	298	1.0107	1.7792	177.9
	0.01	1.622	323	1.0094	1.6373	163.7
	0.01	1.494	348	1.0081	1.5061	150.6
	0.01	1.375	373	1.0071	1.3845	138.4
	0.01	1.263	398	1.0062	1.2708	127.1

Table E.19: AB6 + H₂

Molecular structure	Mole fraction −	Pressure P/MPa	Temperature T/K	Fugacity coefficient ϕ_{H_2}/−	Fugacity f_{H_2}/MPa	Henry coefficient H/MPa
A1B6	0.01	3.461	298	1.0212	3.5348	353.5
	0.01	3.264	323	1.0189	3.3259	332.6
	0.01	3.062	348	1.0168	3.1139	311.4
	0.01	2.862	373	1.0148	2.9044	290.4
	0.01	2.667	398	1.0130	2.7012	270.1
A2B6	0.01	2.366	298	1.0145	2.4000	240.0
	0.01	2.210	323	1.0128	2.2387	223.9
	0.01	2.060	348	1.0112	2.0826	208.3
	0.01	1.913	373	1.0099	1.9324	193.2
	0.01	1.772	398	1.0087	1.7876	178.8
A3B6	0.01	1.796	298	1.0110	1.8156	181.6
	0.01	1.662	323	1.0096	1.6776	167.8
	0.01	1.537	348	1.0084	1.5497	155.0
	0.01	1.420	373	1.0073	1.4299	143.0
	0.01	1.309	398	1.0064	1.3172	131.7

Table E.20: AB7 + H₂

Molecular structure	Mole fraction −	Pressure P/MPa	Temperature T/K	Fugacity coefficient ϕ_{H_2}/−	Fugacity f_{H_2}/MPa	Henry coefficient H/MPa
A1B7	0.01	3.193	298	1.0196	3.2559	325.6
	0.01	2.972	323	1.0172	3.0227	302.3
	0.01	2.755	348	1.0151	2.7964	279.6
	0.01	2.546	373	1.0132	2.5801	258.0
	0.01	2.348	398	1.0115	2.3754	237.5
A2B7	0.01	2.231	298	1.0136	2.2611	226.1
	0.01	2.060	323	1.0119	2.0847	208.5
	0.01	1.900	348	1.0104	1.9193	191.9
	0.01	1.748	373	1.0090	1.7638	176.4
	0.01	1.605	398	1.0078	1.6174	161.7
A3B7	0.01	1.728	298	1.0106	1.7462	174.6
	0.01	1.581	323	1.0091	1.5954	159.5
	0.01	1.448	348	1.0079	1.4591	145.9
	0.01	1.325	373	1.0068	1.3342	133.4
	0.01	1.212	398	1.0059	1.2191	121.9

Table E.21: AB8 + H$_2$

Molecular structure	Mole fraction	Pressure	Temperature	Fugacity coefficient	Fugacity	Henry coefficient
	−	P/MPa	T/K	ϕ_{H_2}/−	f_{H_2}/MPa	H/MPa
A1B8	0.01	3.687	298	1.02270	3.7711	377.1
	0.01	3.489	323	1.02020	3.5590	355.9
	0.01	3.285	348	1.01800	3.3444	334.4
	0.01	3.083	373	1.01590	3.1323	313.2
	0.01	2.886	398	1.01410	2.9266	292.7
A2B8	0.01	2.567	298	1.01570	2.6073	260.7
	0.01	2.411	323	1.01390	2.4450	244.5
	0.01	2.259	348	1.01230	2.2872	228.7
	0.01	2.111	373	1.01090	2.1342	213.4
	0.01	1.967	398	1.00960	1.9861	198.6
A3B8	0.01	1.892	298	1.01160	1.9144	191.4
	0.01	1.770	323	1.01020	1.7885	178.9
	0.01	1.655	348	1.00900	1.6697	167.0
	0.01	1.544	373	1.00800	1.5566	155.7
	0.01	1.438	398	1.00700	1.4479	144.8

Table E.22: AB9 + H$_2$
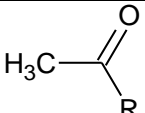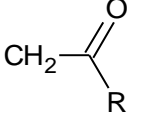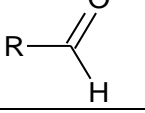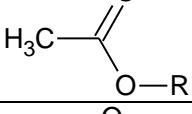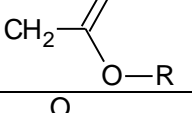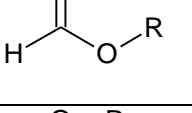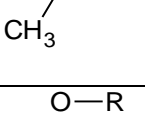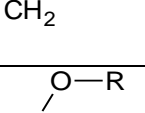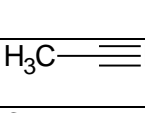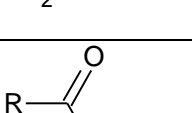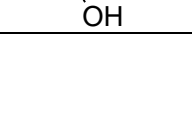
Molecular structure	Mole fraction	Pressure	Temperature	Fugacity coefficient	Fugacity	Henry coefficient
	−	P/MPa	T/K	ϕ_{H_2}/−	f_{H_2}/MPa	H/MPa
A1B9	0.01	3.898	298	1.02400	3.9920	399.2
	0.01	3.727	323	1.02160	3.8074	380.7
	0.01	3.543	348	1.01940	3.6118	361.2
	0.01	3.354	373	1.01740	3.4121	341.2
	0.01	3.164	398	1.01550	3.2126	321.3
A2B9	0.01	2.756	298	1.01690	2.8024	280.2
	0.01	2.604	323	1.01510	2.6437	264.4
	0.01	2.454	348	1.01340	2.4869	248.7
	0.01	2.305	373	1.01190	2.3327	233.3
	0.01	2.158	398	1.01050	2.1810	218.1
A3B9	0.01	2.172	298	1.01330	2.2009	220.1
	0.01	2.025	323	1.01170	2.0482	204.8
	0.01	1.887	348	1.01030	1.9066	190.7
	0.01	1.758	373	1.00910	1.7735	177.4
	0.01	1.634	398	1.00800	1.6471	164.7

Appendix F

UNIFAC group contribution

Table F.1: UNIFAC Group Specifications and PSRK compatibility of parameters

Group number	Name	Structure	Gas compatibility PSRK	
			CO_2	H_2
1020	CH_3	$R-CH_3$	X	X
1010	CH_2	$R-CH_2$ R	X	X
1005	CH	$R=CH$ R	X	X
1000	C	$R=C$ R	X	X
1070	$CH_2=CH$	$R-CH$ CH_2	X	X
1065	CH=CH	$R-CH$ $CH-R$	X	X
1060	$CH_2=C$	$R=C$ CH_2	X	X
1055	CH=C	$R-CH$ $C=R$	X	X
1050	C=C	$R=C$ $C=R$	X	X
1105	ACH	R R	X	X
1100	AC	R —R R	X	X
1060	$ACCH_3$	R —CH_3 R	X	X
1155	$ACCH_2$	R —H_2C R	X	X
1150	ACCH	R —HC R	X	X
1200	OH	R-OH	X	X
1350	ACOH	R —OH R	X	X

1405	CH$_3$CO	$\begin{array}{c} \text{O} \\ \| \\ \text{H}_3\text{C}-\text{C} \\ \| \\ \text{R} \end{array}$	X	X
1400	CH$_2$CO	$\begin{array}{c} \text{O} \\ \| \\ \text{CH}_2-\text{C} \\ \| \\ \text{R} \end{array}$	X	X
1450	CHO	$\begin{array}{c} \text{O} \\ \| \\ \text{R}-\text{C} \\ \| \\ \text{H} \end{array}$	X	X
1505	CH$_3$COO	$\begin{array}{c} \text{O} \\ \| \\ \text{H}_3\text{C}-\text{C} \\ \| \\ \text{O}-\text{R} \end{array}$	X	X
1500	CH$_2$COO	$\begin{array}{c} \text{O} \\ \| \\ \text{CH}_2-\text{C} \\ \| \\ \text{O}-\text{R} \end{array}$	X	X
1550	HCOO	$\begin{array}{c} \text{O} \\ \| \\ \text{H}-\text{C} \\ \| \\ \text{O}-\text{R} \end{array}$	X	X
1615	CH$_3$O	$\text{CH}_3-\text{O}-\text{R}$	X	X
1610	CH$_2$O	$\text{CH}_2-\text{O}-\text{R}$	X	X
1605	CHO	$\text{CH}-\text{O}-\text{R}$	X	X
1905	CH$_3$CN	$\text{H}_3\text{C}-\!\!\equiv\!\!\text{N}$	X	X
1900	CH$_2$CN	$\text{CH}_2-\!\!\equiv\!\!\text{N}$	X	X
1955	COOH	$\begin{array}{c} \text{O} \\ \| \\ \text{R}-\text{C} \\ \| \\ \text{OH} \end{array}$	X	X

Appendix G

Literature VLE and PSRK VLE

Table G.1: Benzene + CO_2

Experimental data			PSRK simulation
T/K	x_i/−	P/MPa	P/MPa
315.45	0.162	1.71	1.93
	0.229	2.42	2.65
	0.300	3.15	3.37
	0.349	3.61	3.83
	0.403	4.10	4.31
	0.458	4.56	4.77
	0.530	5.11	5.31
	0.582	5.47	5.67
	0.593	5.53	5.75
	0.632	5.79	6.00
	0.653	5.93	6.13
	0.718	6.33	6.52
	0.795	6.81	6.98
	0.812	6.92	7.09
	0.845	7.13	7.30
	0.887	7.40	7.60
	0.922	7.75	7.89

Table G.2: Benzene + H_2

Experimental data			PSRK simulation
T/K	x_i/−	P/MPa	P/MPa
295	0.017	6.99	8.17
	0.027	10.44	12.96
	0.034	13.88	16.60
	0.042	17.33	20.88

Table G.3: Ethylbenzene + H_2

Experimental data			PSRK simulation
T/K	x_i/−	P/MPa	P/MPa
295	0.033	10.44	11.06
	0.044	13.88	15.00
	0.055	17.33	19.09

Table G.4: Ethylbenzene + CO$_2$

Experimental data			PSRK simulation
T/K	x_i/$-$	P/MPa	P/MPa
313.2	0.557	5.69	5.71
	0.600	6.09	6.05
	0.617	6.16	6.17
	0.621	6.16	6.20
	0.705	6.66	6.73
	0.822	7.09	7.29
	0.837	7.16	7.36
	0.838	7.16	7.37

Table G.5: Methyl benzoate + CO$_2$

Experimental data			PSRK simulation
T/K	x_i/$-$	P/MPa	P/MPa
313.1	0.586	6.10	5.35
	0.582	6.10	5.30
	0.639	6.60	5.90
	0.638	6.60	5.89
	0.703	7.10	6.57
	0.701	7.10	6.54
	0.790	7.61	7.44
	0.793	7.61	7.47

Table G.6: Phenyl acetate + CO$_2$

Experimental data			PSRK simulation
T/K	x_i/$-$	P/MPa	P/MPa
333.15	0.144	2.00	1.10
	0.279	4.00	2.27
	0.407	6.00	3.55

Table G.7: Biphenyl + CO₂

Experimental data			PSRK simulation
T/K	x_i/–	P/MPa	P/MPa
333.2	0.385	7.74	8.57
	0.388	7.75	8.66
	0.480	10.39	11.75
	0.537	13.49	14.75
	0.571	16.54	17.25
	0.602	19.96	20.03
	0.633	23.30	23.23
	0.677	30.01	26.88
	0.719	35.61	30.23
	0.721	37.46	30.36

Table G.8: Cyclohexane + CO₂

Experimental data			PSRK simulation
T/K	x_i/–	P/MPa	P/MPa
315.45	0.168	1.95	1.82
	0.204	2.35	2.20
	0.238	2.82	2.56
	0.277	3.24	2.96
	0.320	3.68	3.40
	0.360	4.08	3.80
	0.377	4.25	3.96
	0.390	4.40	4.09
	0.418	4.62	4.36
	0.468	5.09	4.82
	0.511	5.41	5.19
	0.563	5.78	5.61
	0.604	6.03	5.92
	0.635	6.25	6.14
	0.707	6.58	6.60
	0.789	7.01	7.05
	0.841	7.28	7.33
	0.862	7.39	7.45
	0.893	7.60	7.65
	0.921	7.85	7.85

Table G.9: Cyclohexane + H$_2$

	Experimental data		PSRK simulation
T/K	x_i/−	P/MPa	P/MPa
295	0.029	6.99	6.16
	0.042	10.44	9.10
	0.056	13.88	12.35
	0.068	17.33	15.43

Table G.10: Cyclohexanone + CO$_2$

	Experimental data		PSRK simulation
T/K	x_i/−	P/MPa	P/MPa
290.8	0.239	1.43	1.29
	0.383	2.22	2.11
	0.424	2.51	2.35
	0.493	2.88	2.76
	0.552	3.25	3.11
	0.626	3.58	3.53
	0.680	3.92	3.84
	0.754	4.34	4.23
	0.815	4.64	4.52
	0.871	4.93	4.76
	0.922	5.16	4.95

Table G.11: Propyl cyclohexane + CO$_2$

	Experimental data		PSRK simulation
T/K	x_i/−	P/MPa	P/MPa
313.1	0.089	1.03	0.91
	0.209	2.54	2.17
	0.343	4.02	3.61
	0.441	5.14	4.65
	0.526	5.97	5.52
	0.606	6.64	6.25
	0.718	7.28	7.06

Table G.12: Cyclohexyl acetate + CO$_2$

Experimental data			PSRK simulation
T/K	x_i/$-$	P/MPa	P/MPa
333.15	0.193	2.00	1.35
	0.370	4.00	2.80
	0.519	6.00	4.28
	0.621	7.50	5.50
	0.733	9.00	7.13

Table G.13: Acetonitrile + CO$_2$

Experimental data			PSRK simulation
T/K	x_i/$-$	P/MPa	P/MPa
318.45	0.251	2.33	2.60
	0.314	2.95	3.22
	0.378	3.60	3.83
	0.461	4.40	4.60
	0.540	5.29	5.30
	0.630	6.08	6.05
	0.690	6.62	6.53
	0.746	7.10	6.95
	0.824	7.73	7.55
	0.902	8.26	8.17
	0.937	8.59	8.50

Table G.14: Hexyl acetate + CO$_2$

Experimental data			PSRK simulation
T/K	x_i/$-$	P/MPa	P/MPa
333.15	0.119	1.00	0.80
	0.229	2.00	1.61
	0.321	3.00	2.35
	0.418	4.00	3.20
	0.569	6.00	4.75
	0.642	7.00	5.63
	0.699	8.00	6.40

Table G.15: Ethanol + CO$_2$

Experimental data			PSRK simulation
T/K	x_i/−	P/MPa	P/MPa
298.15	0.114	1.55	1.80
	0.132	1.83	2.05
	0.151	2.07	2.31
	0.198	2.62	2.92
	0.232	3.12	3.33
	0.294	3.67	3.99
	0.323	4.10	4.25
	0.329	4.30	4.31
	0.385	4.61	4.74
	0.457	5.11	5.15
	0.484	5.22	5.26
	0.500	5.31	5.32
	0.533	5.41	5.41
	0.545	5.50	5.44
	0.569	5.59	5.48
	0.626	5.70	5.54
	0.691	5.79	5.54
	0.876	5.90	5.61

Table G.16: Acetic acid + CO$_2$

Experimental data			PSRK simulation
T/K	x_i/−	P/MPa	P/MPa
298.15	0.034	0.34	0.30
	0.045	0.44	0.39
	0.062	0.60	0.54
	0.069	0.66	0.60
	0.083	0.78	0.72
	0.101	0.94	0.87
	0.123	1.14	1.06
	0.151	1.39	1.30

Table G.17: Acetic acid + H$_2$

Experimental data			PSRK simulation
T/K	x_i/−	P/MPa	P/MPa
298.15	0.002	0.55	0.34
	0.003	0.77	0.43
	0.004	1.28	0.60
	0.006	1.74	0.85
	0.007	2.10	1.00
	0.008	2.47	1.12
	0.009	2.85	1.32

Table G.18: Decane + CO$_2$

Experimental data			PSRK simulation
T/K	x_i/−	P/MPa	P/MPa
344.3	0.069	0.89	0.90
	0.120	1.53	1.60
	0.169	2.18	2.29
	0.217	2.82	2.99
	0.265	3.47	3.71
	0.319	4.24	4.55
	0.366	4.95	5.31
	0.412	5.62	6.08
	0.459	6.35	6.88
	0.502	7.00	7.63
	0.549	7.75	8.46
	0.586	8.32	9.12
	0.630	9.05	9.91

Table G.19: Decane + H$_2$

Experimental data			PSRK simulation
T/K	x_i/−	P/MPa	P/MPa
283.22	0.031	5.03	6.52
	0.038	6.34	8.12
	0.056	9.46	12.46
	0.067	11.64	15.30
	0.078	13.49	18.28